Carotid Hemodynamics and Atherosclerotic Plaque Composition

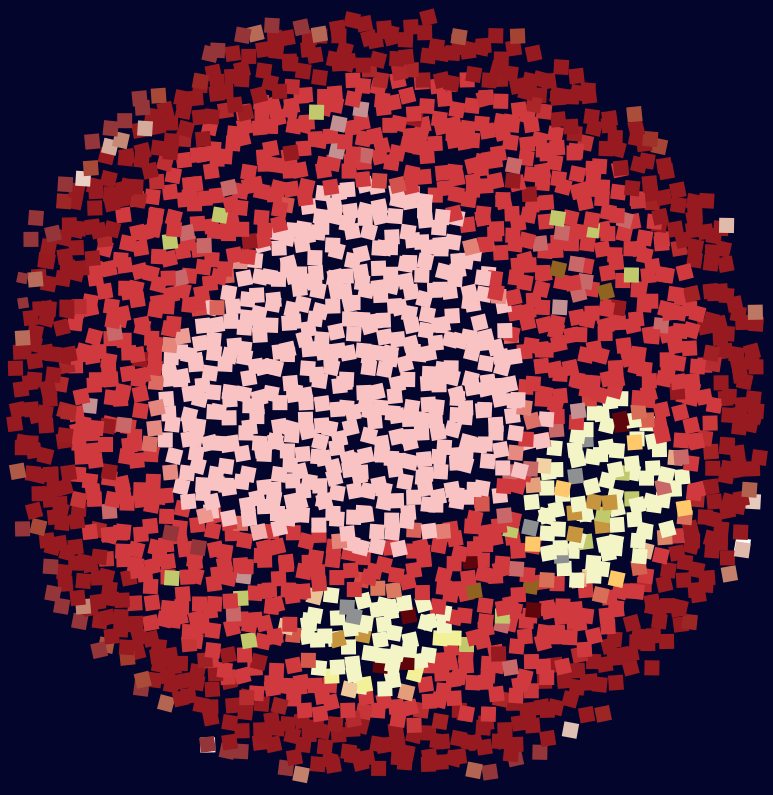

Astrid Moerman

Carotid Hemodynamics and Atherosclerotic Plaque Composition

Astrid Moerman

ISBN: 978-94-6421-085-9

Lay-out: Niek van der Heijden, Astrid Moerman
Coverdesign: Astrid Moerman
Printing: Ipskamp Printing, Amsterdam

A digital version of this thesis is available at http://repub.eur.nl

Carotid Hemodynamics and Atherosclerotic Plaque Composition

Hemodynamiek van de halsslagader en weefselsamenstelling van atherosclerotische plaques

Proefschrift

ter verkrijging van de graad van doctor aan de
Erasmus Universiteit Rotterdam
op gezag van de rector magnificus
Prof.dr. R.C.M.E. Engels
en volgens besluit van het College voor Promoties.

De openbare verdediging zal plaatsvinden op
woensdag 4 november 2020 om 15.30 uur

door

Astrid Moerman

geboren te Maassluis

Erasmus University Rotterdam

Promotiecommissie:

Promotor	*Prof. dr. ir. A.F.W. van der Steen*
Overige leden	*Prof. dr. A. van der Lugt* *Prof. dr. Y.B. de Rijke* *Prof. dr. ir. C. Lally*
Copromotoren	*Dr. K. van der Heiden* *Dr. ir. F.J.H. Gijsen*

The research described in this thesis was supported by a grant of the Dutch Heart Foundation (DHF 2014T096). Financial support by the Dutch Heart Foundation for the publication of this thesis was gratefully acknowledged. Additional financial support for the printing of this thesis was kindly provided by Erasmus University Rotterdam.

Contents

Chapter 1 Introduction

Atherosclerosis – a disease of arteries

The cardiovascular system

The human body is equipped with a vascular network consisting of arteries and veins. This vascular network effectively supplies all parts of the body with blood rich in oxygen and nutrients. The heart, or cardiac muscle, which embodies the center of this so-called cardiovascular system, pumps the blood through the vasculature by a rhythm of subsequent contractions and relaxations. Oxygen-rich blood is circulated from the lungs, via the heart and arteries, to all parts of the body, while a network of veins delivers the resulting oxygen-poor blood from all parts of the body back to the heart and subsequently to the pulmonary arteries, for re-oxygenation by the lungs. Besides oxygen, other substances, such as nutrients and waste, are circulated between different organs or body parts by the cardiovascular system.

Arteries are tubular structures of varying size, that by definition carry blood from the heart to the organs and periphery of the body. The arterial wall is made up of three layers: the innermost layer is called the tunica intima, the middle layer the tunica media and the outer layer the tunica adventitia. In healthy arteries, the intimal layer consists of one layer of endothelial cells on a basal lamina and a thin layer of extracellular matrix. The intimal layer covers the luminal surface and is separated from the medial layer by an elastic membrane, the internal elastic lamina. The medial layer is composed of several layers of smooth muscle cells separated by an elastic lamina that, by contracting or relaxing, can actively influence the size of the artery. The adventitial layer consists of connective tissue, mostly collagen, and provides rigidity. Depending on the location of the artery, the medial and adventitial layers vary in thickness. Larger arteries, such as the aorta and the carotid arteries, which are located in the vicinity of the heart, have a thick medial muscular layer, which is necessary to withstand the fluctuations in blood pressure elicited by the pumping heart. These arteries are called elastic arteries. Towards the periphery, as the elastic arteries pass into muscular arteries and subsequently into arterioles, both the diameter and the media thickness of arteries gradually decrease. From the arterioles, blood is transported into the capillary beds, a dense network of very small vessels. The small vessel size and large surface area of the capillaries al-

lows for efficient exchange of oxygen and nutrients from the blood to the tissue [1].

Atherosclerosis

The endothelial cells that line the lumen of a healthy artery regulate the transport of nutrients, signaling molecules and other substances between the blood and the vessel wall by adjusting their degree of permeability in response to systemic or mechanical cues. Dysfunction of endothelial cells primes the arterial wall for atherosclerosis [2]. Endothelial dysfunction can be triggered by mechanical factors, which will be discussed in the next paragraph, and can be enhanced by a variety of risk factors such as lifestyle, e.g. smoking, diabetes and physical inactivity, and/or genetic factors [3]. Endothelial dysfunction results in increased vascular permeability which enables circulating lipoproteins, in particular low density lipoprotein (LDL), from the blood to accumulate in the intima. Lipoproteins are transport vehicles for lipid molecules, composed of a protein-enforced, hydrophilic outer membrane and a core of hydrophobic lipid molecules. Major lipid components of the lipoprotein core are cholesteryl esters and triglycerides, while the membrane consists of a monolayer of phospholipids and free cholesterol. The influx of lipoproteins and their eventual aggregation and oxidative modification attracts circulating monocytes, that transmigrate into the intima and subsequently transform into macrophages [4–6]. The macrophages internalize the accumulated lipoproteins with the aim of converting and excreting the sterol lipids as solubilized esterified lipid droplets [7,8]. However, if too much lipid accumulates in the arterial wall, this cellular conversion system cannot keep pace and the macrophages turn into lipid-laden foam cells. Apoptosis of these foam cells and the resulting spill of their lipid contents into the tissue, forming so-called necrotic cores or lipid pools, exacerbates instead of resolves, the pathogenic process [3,4]. The intimal lesion that is formed by this process is called ‘plaque’. At the same time, the interaction of lipoproteins and lipoprotein-derived lipids with immune cells such as macrophages can induce a wide array of signaling pathways that are not exclusively pro-atherogenic [7]. Over the course of disease progression, the size of the plaque can increase and its compositional complexity [9] and lipid content [5,6,8,10] can change. Disease stages were classified histologically and were found to vary from pathological intimal thickening to thin fibrous cap atheroma [3,11,12]. The first stages of atherosclerotic disease are characterized by thickening of the intima, foam cell infiltrates and small extracellular lipid pools. More advanced plaques contain larger necrotic cores which are shielded from the blood by a fibrous layer, i.e. the cap, and these plaques may contain calcifications, cholesterol crystals and/or neovascularization. Several processes can result in thinning and/or weakening of the

fibrous cap, rendering the cap at risk of rupture. Cap rupture causes the release and subsequent embolization of plaque contents into the circulation, which can lead to cerebrovascular or cardiovascular events, depending on the anatomical location of the plaque. Based on the rupture risk, plaques can alternatively be referred to as stable, i.e. fibrous tissue-rich, or vulnerable, i.e. containing large cores of lipids and necrotic debris covered by a thin cap.

Hemodynamics and disease initiation and progression

Wall shear stress and plaque initiation

Mechanical factors induce endothelial dysfunction, driving the pattern in which early atherosclerotic plaques appear over the vascular tree. Bends and bifurcations of the arterial system are so-called predilection sites for atherosclerosis. This phenomenon can be attributed to wall shear stress (WSS), the frictional force exerted by the flowing blood on the endothelial cells. Endothelial cells contain mechanosensitive structures e.g. cell surface receptors, that sense patterns and levels of WSS and that respond to it by regulating intracellular signaling cascades that regulate several processes, including vessel diameter [13,14]. Via this mechanism physiological WSS values can be retained, even when the amount of blood flow alters. Physiological values of WSS, i.e. around 1 Pa, are atheroprotective: they induce a quiescent, anti-inflammatory state in endothelial cells. Low and/or oscillatory WSS values however, elicit endothelial cell activation and a pro-inflammatory state [15,16]. Because vessel geometry influences WSS patterns, bends and bifurcations in the arterial tree are exposed to low and/or oscillatory WSS and thus predisposed for lesion initiation. Upon activation, endothelial cells lose their aligned appearance and enter a pro-atherogenic state, characterized by increased activation of pro-inflammatory signaling pathways, resulting in increased adhesion molecule expression to bind immune cells, increased oxidative stress and increased permeability [2,15].

The carotid arteries are prone to develop plaques

One of the predilection sites for lesion initiation is the carotid bifurcation. The human body contains two carotid arteries, which accommodate the bulk of the blood transport from the aorta to the head. The part of the carotid artery proximal to the aorta is called the common carotid artery (CCA). The CCA bifurcates into the internal carotid artery (ICA), which delivers blood to the brain, and the external carotid artery (ECA), which supplies the face. The geometry of the carotid bifurcation region induces low and oscillatory WSS patterns, and subsequent priming for plaque initiation, at the lateral walls of the bifurcation

and in the ICA (Fig. 1 [17]). Plaque initiation and development at the carotid artery can be seen in all people and already at a young age [18]. As the carotid artery is a large and superficial artery, it is easily accessible for imaging and surgical intervention. This renders the carotid arteries a widely studied anatomical location for investigating atherosclerosis initiation and progression in relation to WSS.

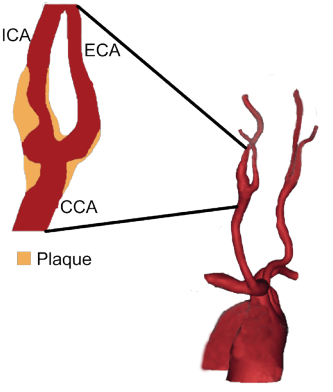

Fig. 1: The anatomy of the carotid arteries. The common carotid artery (CCA) bifurcates into the internal carotid artery (ICA) and external carotid artery (ECA). This bifurcation region is susceptible to atherosclerotic plaque development. Figure adapted from [17]

Computation of WSS

There is no method to directly measure WSS *in vivo*. However, there are ways to derive WSS values based on direct measurements of other hemodynamic parameters and vessel geometry. The most accurate way is using computational fluid dynamics (CFD). This is a computational method in which the Navier-Stokes equations, which describe the behavior of fluid, are numerically solved. The method requires an accurate reconstruction of the artery geometry, in our case the carotid bifurcation region, discretized into a mesh of very small elements. Additionally, the fluid properties of the blood, such as the viscosity and density, need to be described. These values are often based on population-averages reported in literature. Third, the physical boundary conditions, i.e. measures of the blood flow at the in- and outlet regions of the geometry, need to be defined. Both the artery geometry and the boundary conditions necessary for CFD can be obtained by imaging. For this purpose, imaging of carotid arteries is often performed by magnetic resonance imaging (MRI). When all required input values have been set, the Navier-Stokes equations can be solved in an iterative manner. These CFD simulations, implemented in commercial software packages, result in a description of the velocity and pressure of the

fluid in all directions, which are used to calculate WSS.

WSS and plaque progression

Though WSS is considered a relatively well-established factor in plaque initiation, its contribution to plaque progression is less clear. Plaque growth is initially accompanied by outward or expansive vessel remodeling, which ensures preservation of lumen diameter and consequently sustainment of the low WSS levels [18,19]. At a relative plaque area of around 40% however, a plaque generally starts to encroach the lumen and this lumen narrowing can locally induce an increase in WSS in case of unaltered flow rates [18]. This increased WSS might consecutively alter endothelial cell signaling and influence plaque progression [20]. Thus as atherosclerosis progresses, the interplay between WSS and plaque progression becomes interdependent and this relation remains to this day not fully elucidated [20,21]. Finding a correlation between WSS and compositional characteristics of advanced atherosclerotic plaques is relevant for understanding disease pathophysiogy, but might also add predictive value to the current set of prognostic markers for plaque vulnerability, thereby improving diagnosis and treatment strategy. The next paragraph provides an overview of the currently available models and knowledge regarding this matter.

Investigating WSS and atherosclerosis in the carotid arteries

In order to elucidate the relation between WSS and plaque progression, different animal models of surgically-induced atherosclerosis have been developed [22]. An example is the placement of a tapering cast around the CCA of mice, to induce altered WSS patterns and accelerate atherosclerosis progression [23]. Animal models provide a controllable environment in which WSS and plaque development can be monitored over time. This availability of WSS metrics and plaque information at multiple time points is an important advantage of animal models. In human subjects, on the other hand, WSS and plaque composition have been investigated mostly by cross-sectional studies involving only one time point. To this end, a wide array of imaging studies, mostly using MRI, ultrasound or Computed Tomography (CT), have been performed to assess the association between atherosclerosis and WSS in the carotid artery in humans, both in asymptomatic and symptomatic patients. In these studies, WSS was correlated to compositional features of plaque vulnerability, e.g. wall thickness, lipid pool size, presence of intraplaque hemorrhage, ulcer and/or inflammatory markers [24–32]. The composition of an advanced plaque was found to vary over its axial length and the site of maximal lumen narrowing was not necessarily the plaque's most vulnerable location. That is, ulceration, a strong independent

predictor of stroke [33–35], and associated with plaque rupture [36], has been encountered predominantly upstream of the minimal lumen area [29,37–39] and also occurs in hemodynamically insignificant stenosis [33,37]. Also, the cellular composition was shown to alter over the axial length of the plaque, with a higher abundancy of macrophages and proteolytic and pro-apoptotic factors, assumed to cause cap thinning, at the high shear stress-exposed upstream site [28,40]. The inhomogeneous morphology and composition of advanced plaques suggests a relation between local hemodynamics and plaque composition. Histology is the current gold standard for assessing plaque composition in high resolution. However, the one-to-one relation between local WSS levels and histology-based plaque composition has not been performed yet in a substantial set of cases of advanced atherosclerosis.

Identification of the vulnerable, rupture-prone plaque

Most research into the pathophysiology of atherosclerosis is ultimately aimed at identifying the vulnerable plaque based on tissue compositional or hemodynamic parameters. At the same time, development of imaging strategies to visualize these plaque characteristics indicative of vulnerability is ongoing [41]. Besides the potential of WSS as a marker for plaque vulnerability, which is covered in the first part of this thesis, we also investigate the plaque's lipid composition in relation to histological markers of vulnerability. Namely, as the lipid molecules incorporated into the plaque have been shown to reflect disease stage [5,6,8,10], studying this lipid composition will be informative for plaque phenotyping and risk assessment. *In vivo*, the spectral lipid signal can be visualized by imaging modalities like spectral photoacoustics [42], making the lipid profile of a plaque a potential powerful imaging biomarker.

Imaging of lipids by MALDI-MSI

A suitable imaging modality for visualizing lipids in tissue sections is matrix-assisted laser desorption/ionization mass spectrometry imaging (MALDI-MSI) [43]. This method requires deposition of a matrix on the tissue section, which, upon laser irradiation, promotes the desorption and ionization of the tissue molecules [44,45]. Depending on the chosen ionization mode of the MALDI source, positive or negative analyte ions are formed, which enter the mass spectrometer. Ionization using MALDI produces single-charged ions and does not elicit in-source molecular fragmentation, which is very advantageous for the measurement of lipids [43,46]. The chosen matrix and ionization mode determine the type of lipids that can be measured: using positive polarity e.g. phosphocholines, sphingomyelins and triglycerides can be detected, while in negative

mode e.g. phosphatidylinositols or phosphatidylethanolamines are seen [47]. In the mass spectrometer, the ions are sorted by their mass-to-charge (*m/z*) ratio. The measurement output is described by a mass spectrum, which reports the measured molecular masses and their relative intensities. In mass spectrometry imaging (MSI) a mass spectrum is captured for each pixel of the tissue section. In this way, a multi-dimensional dataset is collected, containing both spatial and mass spectral information. Tissue sections imaged by MALDI-MSI can, after matrix removal, be stained histochemically. Using accurate image registration, the spatial lipid data captured by MALDI-MSI can be correlated to tissue compositional features identified by histology.

Aim and outline of this thesis

This thesis is aimed at visualizing hemodynamic and tissue compositional patterns in atherosclerotic carotid bifurcations. The first part of this thesis is focused on the distribution of WSS and its correlation with histologically-determined compositional characteristics of plaque vulnerability. In Part II, spatial lipid patterns in advanced carotid plaques are investigated. We compare these lipid distributions to compositional characteristics of plaque vulnerability with the aim of finding lipid signatures that help to identify the vulnerable plaque.

PART I: Hemodynamics and plaque vulnerability

Chapter 2 describes an image-registration pipeline to register WSS data and corresponding histological images of human carotid plaques. The WSS data is calculated from *in vivo* MR imaging and computational fluid dynamics. Using a series of rigid and non-rigid registration steps, in conjunction with intermediate imaging modalities to capture tissue deformations inferred by plaque excision and histological processing, we map WSS values on the corresponding histological lumen contours. This method enables correlation of local WSS to the histological composition of the underlying plaque tissue.

In **Chapter 3**, we apply this registration method on a set of human carotid atherosclerotic plaques. We calculate time averaged WSS (TAWSS) patterns as well as oscillatory shear index (OSI) patterns and investigate the correlated histological plaque composition at different tissue depths. NC size was found to be significantly higher at high TAWSS regions and macrophage area and cap thickness were higher at regions exposed to low OSI.

Chapter 4 describes a mouse model in which atherosclerosis is induced by cast placement in the common carotid artery. WSS distribution and disease deve-

lopment are monitored at multiple time points. This longitudinal study shows the temporal and spatial changes in WSS patterns during plaque progression. At the final time point, the correlation between WSS and histological plaque composition is assessed.

PART II: Lipid imaging in atherosclerosis

We developed a pipeline for visualizing the spatial distribution of lipids by MALDI mass spectrometry imaging. **Chapter 5** describes how tissue processing, MALDI measurement parameters and data analysis were optimized to obtain a reproducible and ready-to-use pipeline for lipid imaging in human carotid atherosclerotic plaques. In a set of tissue sections, we investigate the correlation between spatial lipid distributions and histological plaque characteristics.

In **Chapter 6** the lipid imaging pipeline is applied to a dataset of human carotid endarterectomy samples. We analyze the resulting highly dimensional dataset both by a clustering algorithm as well as by a histology-based multivariate analysis. We report increased abundances of sphingomyelins and oxidized cholesteryl esters in necrotic core regions, as well as spatial correlations between diacylglycerols and triacylglycerols with thrombotic tissue.

The main findings in this thesis are discussed in **Chapter 7**. We discuss the added value of our findings to the atherosclerosis research field and the future developments that might be at hand.

References

1. Boron, W. F. & Boulpaep, E. L. ***Medical Physiology***. (Elsevier Saunders, 2005).
2. Gimbrone, M. A. & García-Cardeña, G. Vascular endothelium, hemodynamics, and the pathobiology of atherosclerosis. doi:10.1016/j.carpath.2012.06.006.
3. Bentzon, J. F., Otsuka, F., Virmani, R. & Falk, E. Mechanisms of plaque formation and rupture. ***Circ Res*** **114**, 1852–1866 (2014).
4. Lusis, A. J. Atherosclerosis. ***Nature*** **407**, 233–241 (2000).
5. Upston, J. M. ***et al.*** Disease stage-dependent accumulation of lipid and protein oxidation products in human atherosclerosis. ***Am J Pathol*** **160**, 701–710 (2002).
6. Small, D. M. George Lyman Duff memorial lecture. Progression and regression of atherosclerotic lesions. Insights from lipid physical biochemistry. ***Arterioscler. (Dallas, Tex)*** **8**, 103–129 (1988).
7. Rader, D. J. & Puré, E. Lipoproteins, macrophage function, and atherosclerosis: Beyond the foam cell? ***Cell Metab.*** **1**, 223–230 (2005).
8. Rapp, J. H., Connor, W. E., Lin, D. S., Inahara, T. & Porter, J. M. Lipids of human atherosclerotic plaques and xanthomas: clues to the mechanism of plaque progression. ***J Lipid Res*** **24**, 1329–1335 (1983).
9. Falk, E. Pathogenesis of Atherosclerosis. ***J. Am. Coll. Cardiol.*** **47**, 0–5 (2006).
10. Felton, C. V, Crook, D., Davies, M. J. & Oliver, M. F. Relation of plaque lipid composition and morphology to the stability of human aortic plaques. ***Arterioscler. Thromb. Vasc. Biol.*** **17**, 1337–1345 (1997).
11. Virmani, R., Kolodgie, F. D., Burke, A. P., Farb, A. & Schwartz, S. M. Lessons from sudden coronary death: a comprehensive morphological classification scheme for atherosclerotic lesions. ***Arter. Thromb Vasc Biol*** **20**, 1262–1275 (2000).
12. Stary, H. C. ***et al.*** A definition of advanced types of atherosclerotic lesions and a histological classification of atherosclerosis. A report from the Committee on Vascular Lesions of the Council on Arteriosclerosis, American Heart Association. ***Circulation*** **92**, 1355–1374 (1995).
13. Baeyens, N., Bandyopadhyay, C., Coon, B. G., Yun, S. & Schwartz, M. A. Endothelial fluid shear stress sensing in vascular health and disease. ***Journal of Clinical Investigation*** vol. 126 821–828 (2016).
14. Simmons, R. D., Kumar, S., Thabet, S. R., Sur, S. & Jo, H. Omics-based approaches to understand mechanosensitive endothelial biology and atherosclerosis. ***Wiley Interdiscip. Rev. Syst. Biol. Med.*** **8**, 378–401 (2016).
15. Malek, A. M., Alper, S. L. & Izumo, S. Hemodynamic shear stress and its role in atherosclerosis. ***Jama*** **282**, 2035–2042 (1999).
16. Chiu, J.-J. & Chien, S. Effects of Disturbed Flow on Vascular Endothelium: Pathophysiological Basis and Clinical Perspectives. (2011) doi:10.1152/physrev.00047.2009.-Vascular.
17. Kamenskiy, A. V., Pipinos, I. I., Carson, J. S., Mactaggart, J. N. & Baxter, B. T. Age and disease-related geometric and structural remodeling of the carotid artery. ***J. Vasc. Surg.*** **62**, 1521–1528 (2015).
18. Slager, C. J. ***et al.*** The role of shear stress in the generation of rupture-prone vulnerable plaques. ***Nat Clin Pr. Cardiovasc Med*** **2**, 401–407 (2005).
19. Glagov, S., Weisenberg, E., Zarins, C. K., Stankunavicius, R. & Kolettis, G. J. Compensatory Enlargement of Human Atherosclerotic Coronary Arteries. ***N. Engl. J. Med.*** **316**, 1371–1375 (1987).
20. Slager, C. J. ***et al.*** The role of shear stress in the destabilization of vulnerable plaques and related therapeutic implications. ***Nat Clin Pr. Cardiovasc Med*** **2**, 456–464 (2005).
21. Gijsen, F. ***et al.*** Expert recommendations on the assessment of wall shear stress in human coronary arteries: existing methodologies, technical considerations, and clinical applications. ***Eur Hear. J*** **40**, 3421–3433 (2019).
22. Winkel, L. C., Hoogendoorn, A., Xing, R., Wentzel, J. J. & Van der Heiden, K. Animal models of surgically manipulated flow velocities to study shear stress-induced atherosclerosis. ***Atherosclerosis*** vol. 241 100–110 (2015).
23. Cheng, C. ***et al.*** Atherosclerotic lesion size and vulnerability are determined by patterns of fluid shear stress. ***Circulation*** **113**, 2744–53 (2006).
24. Groen, H. C. ***et al.*** Plaque rupture in the carotid artery is localized at the high shear stress region: a case report. ***Stroke*** **38**, 2379–2381 (2007).
25. Zarins, C. K. ***et al.*** Carotid bifurcation atherosclerosis. Quantitative correlation of plaque localization with flow velocity profiles and wall shear stress. ***Circ Res*** **53**, 502–514 (1983).
26. Tuenter, A. ***et al.*** High shear stress relates to intraplaque haemorrhage in asymptomatic carotid plaques. ***Atherosclerosis*** **251**, 348–354 (2016).
27. Kaazempur-Mofrad, M. R. ***et al.*** Characterization of the atherosclerotic carotid bifurcation using MRI,

finite element modeling, and histology. ***Ann Biomed Eng*** **32**, 932–946 (2004).
28. Dirksen, M. T., van der Wal, A. C., van den Berg, F. M., van der Loos, C. M. & Becker, A. E. Distribution of inflammatory cells in atherosclerotic plaques relates to the direction of flow. ***Circulation*** **98**, 2000–2003 (1998).
29. Lovett, J. K. & Rothwell, P. M. Site of carotid plaque ulceration in relation to direction of blood flow: an angiographic and pathological study. ***Cerebrovasc Dis*** **16**, 369–375 (2003).
30. van Ooij, P. ***et al.*** Spatial correlations between MRI-derived wall shear stress and vessel wall thickness in the carotid bifurcation. ***Eur Radiol Exp*** **2**, 27 (2018).
31. Duivenvoorden, R. ***et al.*** Endothelial shear stress: a critical determinant of arterial remodeling and arterial stiffness in humans--a carotid 3.0-T MRI study. ***Circ Cardiovasc Imaging*** **3**, 578–585 (2010).
32. Shishikura, D. ***et al.*** The relationship between segmental wall shear stress and lipid core plaque derived from near-infrared spectroscopy. ***Atherosclerosis*** **275**, 68–73 (2018).
33. Rothwell, P. M., Gibson, R. & Warlow, C. P. Interrelation between plaque surface morphology and degree of stenosis on carotid angiograms and the risk of ischemic stroke in patients with symptomatic carotid stenosis. ***Stroke*** **31**, 615–621 (2000).
34. Eliasziw, M. ***et al.*** Significance of plaque ulceration in symptomatic patients with high-grade carotid stenosis. ***Stroke*** **25**, 304–308 (1994).
35. Homburg, P. J. ***et al.*** Association Between Carotid Artery Plaque Ulceration and Plaque Composition Evaluated With Multidetector CT Angiography. (2011) doi:10.1161/STROKEAHA.110.597369.
36. Yuan, J. ***et al.*** Imaging carotid atherosclerosis plaque ulceration: Comparison of advanced imaging modalities and recent developments. ***American Journal of Neuroradiology*** vol. 38 664–671 (2017).
37. de Weert, T. T. ***et al.*** Atherosclerotic plaque surface morphology in the carotid bifurcation assessed with multidetector computed tomography angiography. ***Stroke*** **40**, 1334–1340 (2009).
38. Fagerberg, B. ***et al.*** Differences in Lesion Severity and Cellular Composition between in vivo Assessed Upstream and Downstream Sides of Human Symptomatic Carotid Atherosclerotic Plaques. ***J. Vasc. Res.*** **47**, 221–230 (2010).
39. Masawa, N. ***et al.*** Three-dimensional analysis of human carotid atherosclerotic ulcer associated with recent thrombotic occlusion. ***Pathol. Int.*** **44**, 745–752 (2008).
40. Cicha, I. ***et al.*** Carotid plaque vulnerability: a positive feedback between hemodynamic and biochemical mechanisms. ***Stroke*** **42**, 3502–3510 (2011).
41. Bourantas, C. V ***et al.*** Hybrid intravascular imaging: recent advances, technical considerations, and current applications in the study of plaque pathophysiology. doi:10.1093/eurheartj/ehw097.
42. Kruizinga, P. ***et al.*** Photoacoustic imaging of carotid artery atherosclerosis. ***J. Biomed. Opt.*** **19**, 110504 (2014).
43. Norris, J. L. & Caprioli, R. M. Analysis of Tissue Specimens by Matrix-Assisted Laser Desorption/Ionization Imaging Mass Spectrometry in Biological and Clinical Research. ***Chem Rev*** **113**, 2309–2342 (2013).
44. Goto-Inoue, N., Hayasaka, T., Zaima, N. & Setou, M. Imaging mass spectrometry for lipidomics. ***Biochim. Biophys. Acta - Mol. Cell Biol. Lipids*** **1811**, 961–969 (2011).
45. Fuchs, B., Süß, R. & Schiller, J. An update of MALDI-TOF mass spectrometry in lipid research. ***Prog. Lipid Res.*** **49**, 450–475 (2010).
46. Schiller, J. ***et al.*** Matrix-assisted laser desorption and ionization time-of-flight (MALDI-TOF) mass spectrometry in lipid and phospholipid research. ***Prog. Lipid Res.*** **43**, 449–488 (2004).
47. Mezger, S. T. P., Mingels, A. M. A., Bekers, O., Cillero-Pastor, B. & Heeren, R. M. A. Trends in mass spectrometry imaging for cardiovascular diseases. ***Anal Bioanal Chem*** **411**, 3709–3720 (2019).

Chapter 2 An MRI-based method to register patient-specific wall shear stress data to histology

Astrid M. Moerman, Kristine Dilba, Suze-Anne Korteland, Dirk H.J. Poot, Stefan Klein, Aad van der Lugt, Ellen V. Rouwet, Kim van Gaalen, Jolanda J. Wentzel, Antonius F.W. van der Steen, Frank J.H. Gijsen, Kim van der Heiden

Based on: An MRI-based method to register patient-specific wall shear stress data to histology, PLoS ONE, 2019

Abstract

Wall shear stress (WSS), the frictional force exerted on endothelial cells by blood flow, is hypothesized to influence atherosclerotic plaque growth and composition. We developed a methodology for image registration of MR and histology images of advanced human carotid plaques and corresponding WSS data, obtained by MRI and computational fluid dynamics.
The image registration method requires four types of input images, *in vivo* MRI, *ex vivo* MRI, photographs of transversally sectioned plaque tissue and histology images. These images are transformed to a shared 3D image domain by applying a combination of rigid and non-rigid registration algorithms. Transformation matrices obtained from registration of these images are used to transform subject-specific WSS data to the shared 3D image domain as well. WSS values originating from the 3D WSS map are visualized in 2D on the corresponding lumen locations in the histological sections and divided into eight radial segments. In each radial segment, the correlation between WSS values and plaque composition based on histological parameters can be assessed.

The registration method was successfully applied to two carotid endarterectomy specimens. The resulting matched contours from the imaging modalities had Hausdorff distances between 0.57 and 0.70 mm, which is in the order of magnitude of the *in vivo* MRI resolution. We simulated the effect of a mismatch in the rigid registration of imaging modalities on WSS results by relocating the WSS data with respect to the stack of histology images. A 0.6 mm relocation altered the mean WSS values projected on radial bins on average by 0.59 Pa, compared to the output of original registration. This mismatch of one image slice did not change the correlation between WSS and plaque thickness. In conclusion, we created a method to investigate correlations between WSS and plaque composition.

Introduction

Atherosclerosis is a progressive vascular disease, characterized by the accumulation of lipids and inflammatory cells in the vessel wall, which results in plaque formation. A subset of atherosclerotic plaques is prone to rupture [1-3]. A rupture-prone, vulnerable plaque differs compositionally from a stable plaque, and is characterized by a large lipid core covered by a thin fibrous cap, inflammatory cell infiltration and/or intraplaque haemorrhage. In the event of rupture, plaque- and thrombus material may embolize into the distally located vessel bed. Depending on the anatomical location of the plaque, rupture might lead to stroke or acute myocardial infarction. Unravelling the mechanisms be-

hind plaque destabilization, leading to a rupture-prone plaque, is thus of high importance.
Wall shear stress (WSS) is the blood-exerted frictional force on the vessel wall. Low and/or oscillatory WSS is an established factor in atherosclerosis initiation, due to activation of pro-inflammatory pathways in the endothelium. The pro-inflammatory environment favors oxidation and retention of lipoproteins inside the vessel wall, aggravating inflammation and resulting in atherosclerotic plaque formation [4-6].

In case of advanced lumen-intruding plaques, the influence of WSS on the human plaque composition and thus vulnerability is still a subject of debate. Several invasive imaging studies have assessed plaque size and corresponding WSS levels [7-9] while other studies included surrogate markers of plaque vulnerability, such as plaque burden [10-14], intraplaque hemorrhage [15,16], inflammation [17], lipid core size [18] or plaque stiffness [19]. However, none of these studies were able to fully characterize plaque vulnerability as histology is regarded as the gold standard for assessment of local plaque vulnerability. Thus, our research question requires co-registration of 2D histology information with MR imaging and its derived WSS data. Co-registration of imaging modalities is challenging, as the registration method has to account for tissue reorientation and deformation occurring due to multimodal imaging and tissue processing. Different approaches of registering histology sections and 3D medical imaging such as MRI have been proposed, varying from slice-to-slice approaches, slice-to-volume approaches, volume-based approaches and hybrid methods. Also, extra imaging modalities, such as *ex vivo* tissue scans and/or blockface photographs, have been added to registration frameworks to refine registrations and account for tissue processing artefacts [20]. Multiple methods for co-registration have been described in an extensive review [20].

To assess the relation between WSS and plaque composition from histology, we based our image registration method on a previously designed tool [21] to map 2D histological cross-sections of a human carotid plaque to the 3D *in vivo* artery geometry. [21-23]. In our method, the registration of histology and *in vivo* MRI/WSS data was aided by an additional *ex vivo* MR scan and block photographs (en face) of sliced tissue. The novelty of the method presented here, lies in the use of subject-specific geometries and flow data obtained by *in vivo* MR imaging, making the image registration framework fully based upon MRI data. In this paper, the new image registration method is described and tested on two human carotid plaques. Moreover, we simulated the effect of a registration mismatch between imaging modalities on WSS results to evaluate the impact of a potential mismatch on WSS and correlations between WSS and plaque thickness.

Methods

Plaque MR imaging

In vivo MR imaging

Two patients scheduled for elective carotid endarterectomy for recent stroke or transient ischemic attack, underwent an MRI scan one day prior to surgery. The carotid plaques were imaged *in vivo* in order to visualize lumen and outer wall geometry and measure blood flow velocity. Patients were scanned in a 3.0 T MRI scanner (General Electric (GE) Healthcare, Milwaukee, USA) using a four-channel phased-array coil with an angulated setup (Machnet B.V., Roden, The Netherlands). Lumen and plaque geometry were imaged using a black blood 3D fast spin echo (3D-BB-FSE) sequence with variable flip angles (TR/TE: 1000/16 ms, FOV: 15 cm, slice thickness: 0.8 mm, matrix: 160x160, number of excitations 1, scan time: 190 s). The MRI scan was resampled to a resolution of 0.4 x 0.4 x 0.6 mm. Blood flow velocity was measured at 2 locations, approximately 20 mm below and ~20 mm above the carotid bifurcation, using 3D phase-contrast MRI (TR/TE: 5/3 ms, FOV: 15 cm, slice thickness: 4.0 mm, matrix: 160x160, scan time: ~3 min, VENC: 70 cm/s). Written informed consent was obtained. This study was approved by the Medical Ethical Committee of Erasmus MC.

Plaque tissue collection and ex vivo MR imaging

Carotid plaque specimens, hereafter referred to as 'CEA1' and 'CEA2', were collected within 30 minutes after surgical resection. Plaque tissue was resected with a specialized technique, resulting in tissue specimens with intact lumen and plaque morphology [24]. Tissue was rinsed with phosphate-buffered saline (PBS), snap frozen in liquid nitrogen and stored at -80 °C until further processing.
Ex vivo T2w fast recovery FSE (frFSE)MRI scans (TR/TE: 2500/66 ms, in-plane resolution: 0.1 x 0.1 mm, slice thickness: 0.5 mm, matrix: 256x256, scan time: ~20 min, number of slices: 66) of the excised CEAs provided necessary images of the plaque to link histology and *in vivo* MRI images in the registration procedure. *Ex vivo* MR imaging was performed on 4% formaldehyde-fixed plaque specimens, immersed in PBS, with a 7.0T MRI scanner (7.0T Discovery MR901, GE Healthcare, Milwaukee, USA).

Specimen processing, en face photos and analysis

Formaldehyde-fixed CEA tissue was decalcified in a solution of 10% ethylenediaminetetraacetic acid (EDTA) in demineralized water for 14 days, washed in PBS and cut in 1 mm consecutive transverse sections. The proximal side of each transverse section was photographed (IXUS 60, Canon, Tokyo, Japan). Photos, hereafter referred to as 'en face photos', were taken from a fixed point perpendicular to the tissue section. The tissue section was further processed and embedded in paraffin. The en face photo contained landmarks to enable the registration of this photo to the en face photo of the adjacent transverse section, as well as a measuring grid to calculate the image resolution. The paraffin blocks were sectioned into 5 µm sections, which were stained histochemically (Hematoxilyn-Eosin stain and Miller's Elastic stain). Lumen and intima were segmented on the Miller's Elastic stain (Fig. 1), using an in-house developed software tool (Mevislab 2.7.1, MeVis Medical Solutions, Bremen, Germany). Size of plaque components was expressed in mm^2.

Computational fluid dynamics

Lumen contours were segmented from the MRI 3D-BB-FSE scan using ITK-SNAP software [25]. A volume mesh of approximately 4 million tetrahedral and prism elements was generated using ICEM (ANSYS ICEM, 17.1, ANSYS, Pennsylvania, USA). The patient-specific time-dependent blood velocity profile in the common carotid artery (CCA) was derived from the phase-contrast MRI scan using MATLAB (MATLAB R2015b, Mathworks Inc., Natick (MA), USA) and applied as inlet boundary condition [26]. As outlet boundary condition we assumed the outflow ratio of the internal carotid artery (ICA) and external carotid artery (ECA) to be 50:50, corresponding to moderately stenosed carotid bifurcations [27]. According to previously defined protocols, blood density was set to 1060 kg/m3 and non-Newtonian fluid behavior was mimicked by the Carreau-Yasuda model [26]. The Navier-Stokes equations were solved and time-dependent wall shear stress (WSS) was computed using Fluent software (ANSYS Fluent, 17.1, ANSYS, Pennsylvania USA) over the length of two heart cycles with a time step of 0.004 seconds. The results of the second heart cycle were used for analysis to account for entrance effects.

Image registration

In order to register 2D histology images to the 3D shear stress distribution, we adapted an image registration tool that was developed to register *in vivo* CT images to histology [21].

We aimed at mapping histology images, en face photos, *ex vivo* MRI and *in vivo* MRI, as well as the WSS data to a shared 3D image domain. We chose the image domain of the en face photos as the shared domain. To that aim, MRI scans and WSS data were resampled and transformed to the en face image domain by the series of registration steps explained below and shown in Fig. 2. The z-resolution of en face and histology was equal, since each en face photo had a corresponding histology section. Thus by choice of the shared en face image domain, interpolation of histology images in z-direction could be avoided and only in-plane registrations were necessary to transform histology to the shared image domain. Coordinate transformations that describe mappings of the different imaging modalities were obtained in a series of registration steps. An overview of the registration procedure is shown in Fig. 2.

A 3D reconstruction of the excised vessel was created by stacking the en face photos of adjacent transverse sections, using point-based rigid registration based on applied landmarks. In this way, we obtained a 3D stack of en face photos. Subsequently, *in vivo* MRI, *ex vivo* MRI and histology images were mapped to the 3D stack of en face photos via a series of registration steps. We started with rigid registration of *in vivo* MR images to *ex vivo* MR images, by determining corresponding points on the first slice cranial to the bifurcation in both image sets (Fig. 2, step A, blue arrow). This was the first MR slice in which both the internal and the external carotid artery were visible. Based on these points and using a similarity transformation, i.e. rotation and isotropic scaling, the *in vivo* MR images were transformed and resampled to the *ex vivo* image domain using the Elastix toolbox [28]. We assumed the deformation of the plaque in longitudinal direction after surgical resection to be minimal, as the tissue was relatively stiff and was resected in intact shape. After rigid registration, an additional B-spline deformation model was applied to the transformed and resampled *in vivo* MR images to improve the mapping to the *ex vivo* MR images [28]. To that aim, contours of the lumen and outer wall were drawn in both image sets. A non-rigid B-spline transformation (metric: advanced mean squares, optimization: adaptive stochastic gradient descent [28]) was applied to match the *in vivo* contour sets to the *ex vivo* contours (Fig. 2, step A, red arrow). The coordinate transformation resulting from this non-rigid registration step was applied to the *in vivo* MR images that were already rigidly registered to the *ex vivo* images. Thus, with the aid of a similarity and a B-spline transform, the *in vivo* MR images were mapped to the *ex vivo* image domain The *ex vivo* MR images were registered to the 3D stack of en face photos (Fig. 2, step B) using a similar rigid and non-rigid registration procedure. Based on anatomical landmarks, histological sections were registered and transformed to their corresponding section in the 3D stack of en face photos using a similarity transformation (Fig. 2, step C). This resulted in a 3D stack of histology images. Taken together, this set of registration steps provided us with the necessary coordinate transforma-

tions to map the WSS data and the *in vivo* MR images to the 3D stack of en face photos as well.

Data processing, selection and analysis

For data analysis, WSS values originating from the 3D WSS map were visualized in 2D onto the corresponding lumen locations in the histological sections using nearest-neighbor interpolation. Therefore, WSS values were averaged in axial direction over a region of -0.3 mm to +0.3 mm with respect to the z-location of the histological section (Fig. 3A). This axial length corresponded to the axial resolution of the *in vivo* MRI scan. In-plane, the cross-section was subdivided into 8 radial segments and the WSS values were averaged [29]. The centerpoint that served as origin for the radial segmentation, was obtained from the centerline of the transformed 3D WSS map. This centerline was obtained using the centerline algorithm in VMTK software [30] which makes use of the Voronoi diagram of the vessel model. The centerline calculation is based on the radii of maximally inscribed spheres along the path of the Voronoi diagram [31]. An example of a histological image with manually segmented areas and distribution of radial bins is shown in Fig. 1.
Radial bins were eliminated from the dataset on the basis of three types of errors: 1) presence of processing artefacts in histology, 2) mismatch between histology and en face photos due to inhomogeneous shrinkage or strain in the tissue that could not be accounted for in the registration procedure, and 3) mismatch in registration between *in vivo* MR images and en face photos. The presence of all error types was visually assessed by three independent observers. Radial bins were excluded based on consensus. The effect of the exclusion of type 2 and type 3 error-containing bins was investigated with the following metrics: 1) by calculating the Dice Similarity Coefficient (DSC) between lumen segmentations in the en face photos and histology images (type 2 error, DSC_type2) and in the en face photos and transformed *in vivo* images (type 3 error, DSC_type3) and 2) by calculating the Hausdorff distance (HD) between the edges of the lumen segmentations in the en face photos and histology images (HD_type 2) and in the en face photos and in the transformed *in vivo* images (HD_type3). For each radial segment, mean, maximum and minimum WSS (Pa) and average plaque thickness (mm) were calculated. Plaque thickness was defined as the mean shortest distance between the lumen border and the lamina media border in histology images.

Simulation of image registration mismatch

This procedure used a combination of imaging modalities and multiple registration steps to enable reliable registration of WSS data to histology. We investigated the effect of a potential registration mismatch in the order of magnitude of the *in vivo* MR resolution on mapped WSS values. To that aim, we relocated the WSS data with respect to the stack of histology slices. We simulated mismatches in rigid registration of a complete axial *in vivo* MRI slice, i.e. a relocation of WSS data by -0.6 mm or +0.6 mm, and a mismatch of half the axial *in vivo* MRI resolution, i.e. -0.3 mm and +0.3 mm (Fig. 3). We subsequently analyzed the resulting change in WSS value projected on each radial histology bin. The effect of registration mismatches on the possible correlation between WSS and plaque thickness was also investigated by plotting, for each radial bin, the mean, minimum and maximum WSS against the average plaque thickness and calculating the Pearson correlation coefficient R.

Statistical analysis

WSS values projected on radial bins, after different relocation distances of the WSS stack, were compared to the original WSS-histology registration using a Wilcoxon signed rank test. For each relocation case, the correlation between WSS and plaque thickness per radial bin was calculated (MATLAB R2015b, Mathworks Inc., Natick (MA), USA) at a 0.05 significance level.

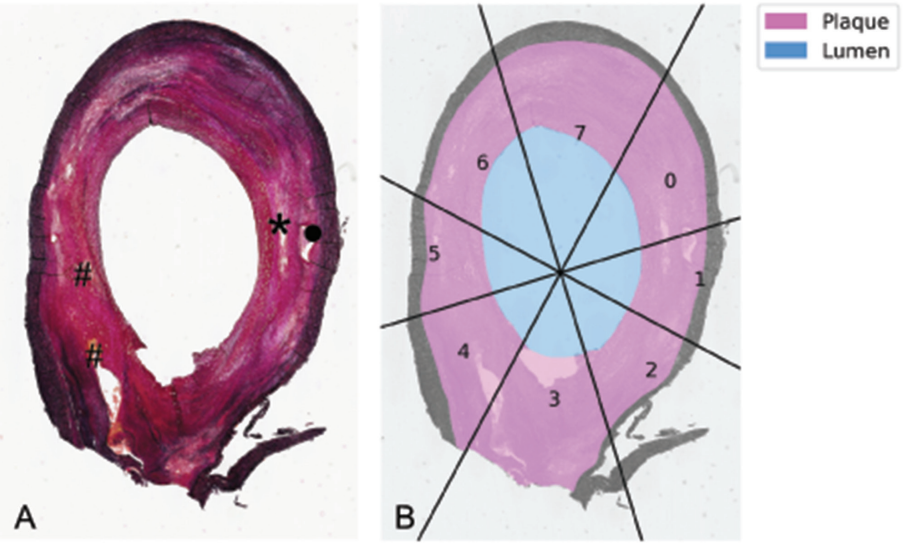

Figure 1: Result of manual segmentation of lumen and intima areas and definition of radial bins. *A) Image of an histology section (Miller's Elastic Stain) of caudal side of an endarterectomy specimen. Plaque components are visualized: * necrotic core, • calcium, # hemorrhage. B) Segmentation of intima and lumen area and radial bins. Based on the centerline, eight radial bins were defined. Mean WSS per radial bin was calculated.*

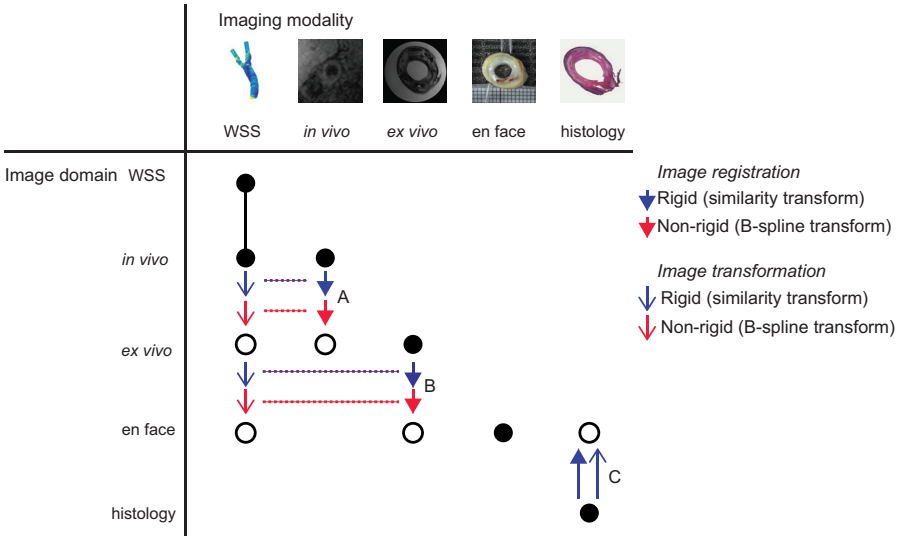

Figure 2: Image registration overview. *Black dots represent the original image domains of the different imaging modalities. White dots represent the image domain where the corresponding imaging modality is mapped to using rigid (blue arrows) and non-rigid (red arrows) transformations. Image sets are brought to a mutual image domain, the en face photos. Step A represents the registration of* ***in vivo*** *MRI to* ***ex vivo*** *MRI. Step B represents the registration of* ***ex vivo*** *MRI to en face photos. The coordinate transformations obtained in registration step A and B can also be used to map the WSS data to the image domain of the en face photos. Step C represents the registration and transformation of histology images to the en face image domain.*

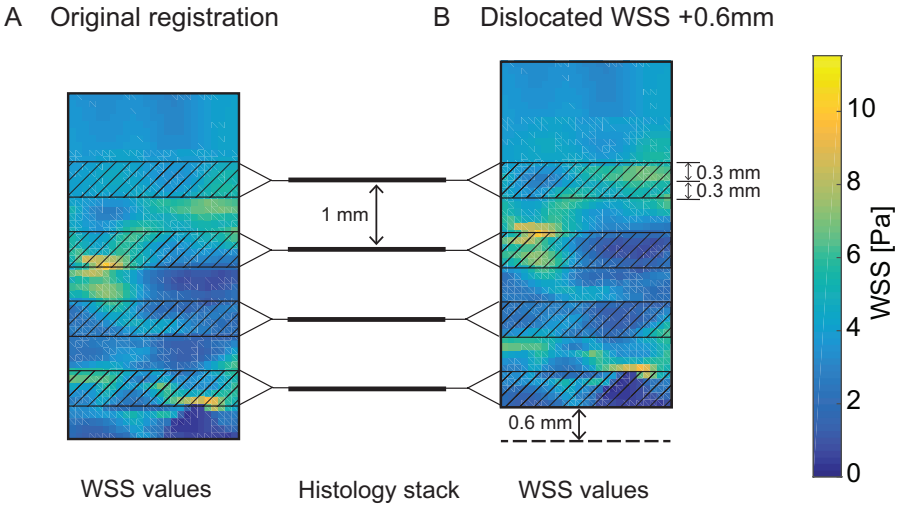

Figure 3: Projection of WSS data on histology (A) and simulation of image registration mismatch (B). *A illustrates the relation between WSS data, which is continuous in z-direction, and the 3D reconstructed stack of histology sections, which are spaced 1mm in z-direction. For analysis of the correlation between WSS and histology, WSS data needed to be averaged in z-direction and mapped and correlated to the nearest histology image. WSS data was averaged in z-direction over a region of -0.3 mm to +0.3 mm with respect to the z-location of the histological section. B illustrates how the WSS data was relocated with respect to the histology stack to simulate a mismatch in registration.*

Results

Plaque imaging, specimen processing and image registration

12 sets of WSS-histology images, representing 12 axial locations, were included for CEA1 and 11 sets of images for CEA2. In Fig. 4 shows some examples of histology slices with the transformed WSS data visualized on the lumen.

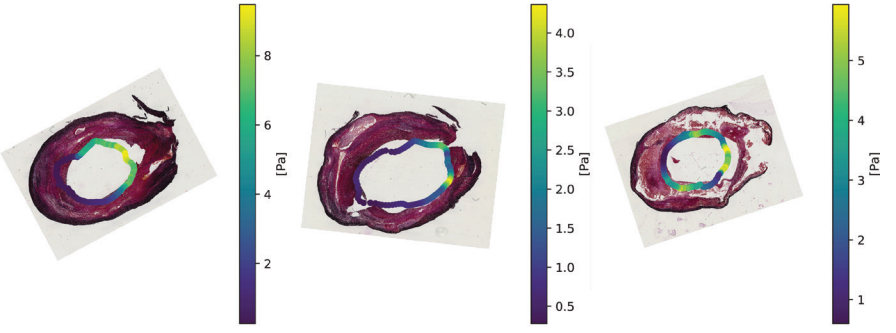

Figure 4: Histology images with WSS data projected onto the lumen. *This figure illustrates the mapping of histology sections and WSS data to the shared image domain by the series of registration steps. When brought into the same image domain, WSS data, averaged in axial direction, can be projected onto the lumen of the corresponding histology section.*

Data processing, selection and analysis

We segmented the lumen and intima contours on all histological sections included in the analysis. Using the centerline as origin, eight radial bins were projected onto a histological section. This resulted in (12+11)*8=184 radial bins in total. Per radial bin, we checked whether histological processing errors (type 1) or registration errors (type 2 and 3) were present. In Table 1 the number of excluded radial segments after image registration on the basis of different errors is summarized for CEA1 and CEA2. Note that some bins present with multiple type of errors.
In both CEAs, the majority of exclusions of radial bins were due to type 1 errors (37 of 184 bins), representing histological artefacts. Errors of type 2 and 3, representing registration mismatches between imaging modalities were found in a small number of bins: 19 of 184 bins had a type 2 error and 13 of 184 bins were found to have a type 3 error. Excluding these bins, based on consensus between three observers, improved the mean DSC and HD values for both CEAs (Table 1). The average DSC_type2 became 0.82 for both CEAs. The average DSC_type3 became 0.90. The average HD for both CEAs was 0.70 mm after exclusion of bins on basis of type 2 errors. After exclusion of type 3 error-containing bins, average HD reduced to 0.57 mm.

Table 1: Exclusion of radial bins on basis of three types of registration error.

	Type 1 error	***Type 2 error***		***Type 3 error***		***Remaining radial bins***
	Number of bins	***Number of bins***	***Mean DSC and HD****	***Number of bins***	***Mean DSC and HD****	
CEA1	24	8	DSC: 0.78 vs. 0.83** HD: 1.06 vs. 0.65	5	DSC: 0.79 vs. 0.90** HD: 1.01 vs. 0.59	73/96 (76.0%)
CEA2	13	11	DSC: 0.70 vs. 0.81** HD: 1.23 vs. 0.75	8	DSC: 0.84 vs. 0.89** HD: 0.87 vs. 0.55	60/88 (68.2%)

**DSC = Dice Similarity Coefficient, HD = Hausdorff Distance (mm)*
***Mean DSC and HD values are given before vs. after exclusion of bins with error*

Simulation of image registration mismatch

The WSS data was relocated by -0.6 mm, -0.3 mm, +0.3 mm and +0.6 mm (Fig. 3B) in z-direction, with respect to the stack of histology images. For each registration case, the mean WSS value per radial histology bin was calculated. For each axial location, the WSS values of the radial bins were averaged. In Fig. 5, the distribution of WSS values over axial locations for each case of relocation of the WSS data is visualized for CEA1 and CEA2 and compared to the original registration. The deviation between WSS values in the original registration and WSS values in cases of simulated registration mismatch increased with increasing length of axial mismatch. Combining the results of both CEAs, mean WSS varied on average 0.25 Pa in case of 0.3 mm relocation and 0.59 Pa in case of 0.6 mm relocation. In none of the cases the difference in mean, minimum or maximum WSS after relocation, with respect to the WSS values of the original registration, were significant. We tested the effect of relocation of the WSS data on the correlation between WSS and plaque thickness. Per axial location,

we plotted, for each radial bin, the mean, minimum and maximum WSS against the average plaque thickness and calculated the R value of the original registration. In two axial locations, the correlation between minimal WSS and plaque thickness was negative and significant. In all other axial locations, no significant correlation between plaque thickness and mean, minimum or maximum WSS was found. Considering the negative correlation between WSS and plaque thickness found in one axial location: this correlation remained significant in all cases of 0.3 mm relocation and in two out of four cases of 0.6 mm relocation. Fig. 6 shows the results of this analysis for one axial location. After relocating the WSS data, the R value of the original registration (R = -0.90) increased to R = -0.97 after application of a +0.6 mm relocation of the WSS stack (Fig. 6). The R value decreased to R = -0.83 when a –0.6 mm relocation was applied (Fig. 6). In this example, significance was lost only in case of -0.6 mm relocation of WSS data. A mismatch of 0.3 mm changed the value of the correlation coefficient between mean WSS and plaque thickness by 0.045 on average. A mismatch of 0.6 mm changed the correlation coefficient between mean WSS and plaque thickness by on average 0.049, compared to the original registration.

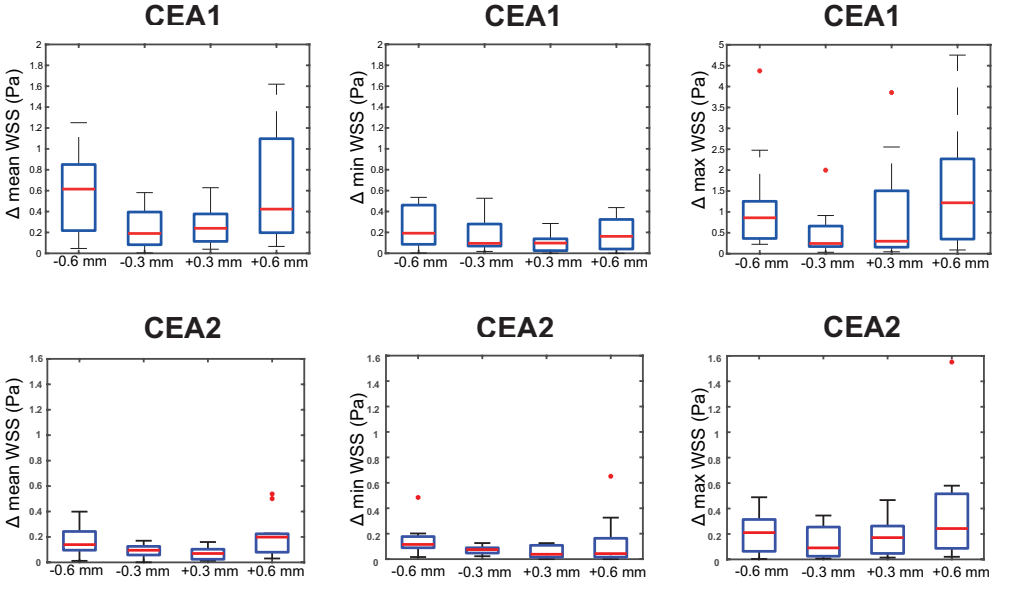

Figure 5: Average absolute variation in mean, minimum and maximum WSS values for axial locations after relocation of WSS data in CEA1 and CEA2. *Delta represents difference in WSS value compared to original rregiststration. Note that the Y-axis scaling differs in the Δmax WSS boxplot.*

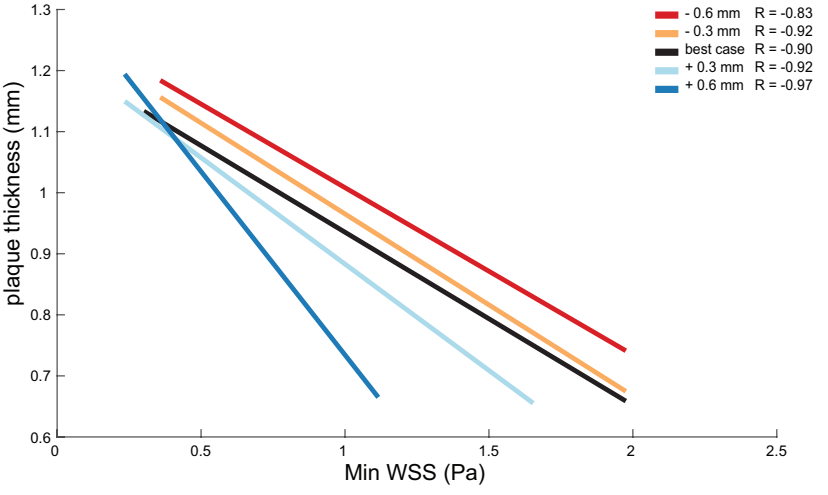

Figure 6: Correlation between minimal WSS and plaque thickness for one axial location. *Variation in minimum WSS-plaque thickness correlation, resulting from relocation of the WSS data in z-direction, is shown.*

Discussion

We developed the first MRI-based pipeline to register WSS data to histology images. This method enables patient-specific investigation of correlations between WSS and histology-based plaque composition. We demonstrated that a mismatch of one slice does not significantly affect WSS distribution or the relation between WSS and plaque thickness.

In terms of image registration, this pipeline is an improvement over a previous CT-based method developed by our group [21]. Our new pipeline is fully based on MRI, and therefore requires less image registration steps. Compared to CT, *in vivo* MR imaging is less harmful to the patient as it does not involve ionising radiation. In addition, patient-specific blood flow and WSS information can be derived from MRI scans [26]. Finally, MR imaging has the potential to image different plaque components [32], that can serve as additional landmarks for image registration, in addition to the lumen and vessel wall contours used in this pipeline.

In addition to our objective of registering WSS data to histology, the developed image registration method can also serve other MRI-based image registration purposes, such as comparison of plaque imaging sequences or validation of image segmentation algorithms.

We assessed registration accuracy and excluded radial bins on the basis of three error types. By this selection process, 28% of radial bins was excluded

from the data-sets. Only a minor part of radial bins was excluded due to insufficient image registration, as represented by type 2 and type 3 errors. Reliable matching between histology and WSS was also evaluated by DSC and HD. After removing insufficiently matched radial bins from the data-sets, average HD values ranged from 0.57 mm to 0.70 mm. This distance between en face photo contours and histology or WSS contours was in the order of magnitude of the *in vivo* MRI resolution.

The applied image registration algorithms required user-defined matching of the bifurcation slices and segmentation of lumen and outer wall contours in different imaging modalities. However, image registration accuracy might be compromised for plaque samples with a relatively large axial length and/or a concentric plaque. In these cases, accuracy of the pipeline can be improved if rigid registration can reliably be based on multiple image slices. To achieve this, additional anatomical landmarks are needed, that are clearly recognizable in the imaging modalities to be registered. Large calcium spots might be good landmarks, as these can be imaged by a combination of MRI sequences [33] and remnants of large calcium areas are also visible in the en face photos and in the histological sections.

The rigid registration of *in vivo* and *ex vivo* MRI is based on the matching of a single image slice. A potential registration error of one image slice in this procedure would equal the MRI resolution in z-direction, i.e. 0.6 mm. After relocation of a half image slice with respect to the original registration, mean WSS values varied on average 0.25 Pa. Simulating the mismatch of a complete MRI slice resulted in an average deviation in mean WSS of 0.59 Pa. As expected, larger mismatches resulted in larger WSS deviations. Although a WSS value difference of 0.59 Pa appears substantial, deviations in WSS values in the same order of magnitude were found to result from variations in vessel segmentations for WSS calculations [34]. As we plan to use this method for assessing possible correlations between WSS and histological parameters, the effect of possible registration and segmentation inaccuracies on found correlations should be carefully documented.

The carotids included in this study are representative geometries, that have a stenosis degree of >70%. The nonsignificant change in WSS values after relocation suggests that the axial gradients in WSS data are not large enough to cause significant changes, even in case of mismatch of a complete MRI slice. Plaques with relatively irregular lumen outlines will show larger gradients in WSS data. In those cases, a registration mismatch is more likely to cause a significant change in WSS data on radial bins. In future applications of this pipeline, the

‘smoothness’ of the lumen should thus be carefully assessed and, in case of irregular plaques, the applicability of this image registration pipeline should be re-assessed

We determined whether a registration mismatch would influence the correlations we want to investigate with the pipeline, namely the identification of a possible relation between WSS and a histology parameter. For this purpose, we analyzed the correlation between WSS and plaque thickness. In two axial locations close to the bifurcation, we found a significant negative correlation ($p<0.05$) between minimum WSS and plaque thickness. The negative correlations remained significant in case of a 0.3 mm mismatch in WSS data. A 0.6 mm WSS relocation, resulting in a larger change in WSS, weakened the correlation to non-significance in two out of four cases. For all cases, the R value of the original registration however, remained negative. Non-significant R values in other axial locations in case of original image registration remained non-significant. Considering the correlation between mean WSS and plaque thickness, the R values after relocation deviated from the R values of the original registration by 0.045-0.048 on average. Similar to the WSS patterns, the correlation between WSS and plaque composition should be reassessed for plaques with a highly irregular lumen, potentially requiring additional registration landmarks.

In conclusion, our novel MRI-based pipeline can match histology to patient-specific WSS data. This method can now be used to investigate the relation between the hemodynamic environment and features of plaque vulnerability.

References

1 Bentzon, J. F., Otsuka, F., Virmani, R. & Falk, E. Mechanisms of plaque formation and rupture. ***Circ Res*** **114**, 1852-1866 (2014).

2 Virmani, R., Kolodgie, F. D., Burke, A. P., Farb, A. & Schwartz, S. M. Lessons from sudden coronary death: a comprehensive morphological classification scheme for atherosclerotic lesions. ***Arterioscler Thromb Vasc Biol*** **20**, 1262-1275 (2000).

3 Schaar, J. A. ***et al.*** Terminology for high-risk and vulnerable coronary artery plaques. Report of a meeting on the vulnerable plaque, June 17 and 18, 2003, Santorini, Greece. ***Eur Heart J*** **25**, 1077-1082 (2004).

4 Malek, A. M., Alper, S. L. & Izumo, S. Hemodynamic shear stress and its role in atherosclerosis. ***Jama*** **282**, 2035-2042 (1999).

5 Cunningham, K. S. & Gotlieb, A. I. The role of shear stress in the pathogenesis of atherosclerosis. ***Lab Invest*** **85**, 9-23 (2005).

6 Slager, C. J. ***et al.*** The role of shear stress in the generation of rupture-prone vulnerable plaques. ***Nat Clin Pract Cardiovasc Med*** **2**, 401-407 (2005).

7 Stone, P. H. ***et al.*** Effect of endothelial shear stress on the progression of coronary artery disease, vascular remodeling, and in-stent restenosis in humans: in vivo 6-month follow-up study. ***Circulation*** **108**, 438-444 (2003).

8 Stone, P. H. ***et al.*** Regions of low endothelial shear stress are the sites where coronary plaque progresses and vascular remodelling occurs in humans: an in vivo serial study. ***Eur Heart J*** **28**, 705-710 (2007).

9 van Ooij, P. ***et al.*** Spatial correlations between MRI-derived wall shear stress and vessel wall thickness in the carotid bifurcation. ***Eur Radiol Exp*** **2**, 27 (2018).

10 Stone, P. H. ***et al.*** Role of Low Endothelial Shear Stress and Plaque Characteristics in the Prediction of Nonculprit Major Adverse Cardiac Events: The PROSPECT Study. ***JACC Cardiovasc Imaging*** **11**, 462-471 (2018).

11 Corban, M. T. ***et al.*** Combination of plaque burden, wall shear stress, and plaque phenotype has incremental value for prediction of coronary atherosclerotic plaque progression and vulnerability. ***Atherosclerosis*** **232**, 271-276 (2014).

12 Eshtehardi, P. ***et al.*** High wall shear stress and high-risk plaque: an emerging concept. ***Int J Cardiovasc Imaging*** **33**, 1089-1099 (2017).

13 Samady, H. ***et al.*** Coronary artery wall shear stress is associated with progression and transformation of atherosclerotic plaque and arterial remodeling in patients with coronary artery disease. ***Circulation*** **124**, 779-788 (2011).

14 Costopoulos, C. ***et al.*** Impact of combined plaque structural stress and wall shear stress on coronary plaque progression, regression, and changes in composition. ***Eur Heart J*** (2019).

15 Tuenter, A. ***et al.*** High shear stress relates to intraplaque haemorrhage in asymptomatic carotid plaques. ***Atherosclerosis*** **251**, 348-354 (2016).

16 Huang, X. ***et al.*** Intraplaque hemorrhage is associated with higher structural stresses in human atherosclerotic plaques: an in vivo MRI-based 3D fluid-structure interaction study. ***Biomed Eng Online*** **9**, 86 (2010).

17 Tang, D. ***et al.*** Cap inflammation leads to higher plaque cap strain and lower cap stress: An MRI-PET/CT-based FSI modeling approach. ***J Biomech*** **50**, 121-129 (2017).

18 Shishikura, D. ***et al.*** The relationship between segmental wall shear stress and lipid core plaque derived from near-infrared spectroscopy. ***Atherosclerosis*** **275**, 68-73 (2018).

19 Duivenvoorden, R. ***et al.*** Endothelial shear stress: a critical determinant of arterial remodeling and arterial stiffness in humans--a carotid 3.0-T MRI study. ***Circ Cardiovasc Imaging*** **3**, 578-585 (2010).

20 Pichat, J., Iglesias, J. E., Yousry, T., Ourselin, S. & Modat, M. A Survey of Methods for 3D Histology Reconstruction. ***Med Image Anal*** **46**, 73-105 (2018).

21 Groen, H. C. ***et al.*** Three-dimensional registration of histology of human atherosclerotic carotid plaques to in-vivo imaging. ***J Biomech*** **43**, 2087-2092 (2010).

22 van Engelen, A. ***et al.*** Multi-feature-based plaque characterization in ex vivo MRI trained by registration to 3D histology. ***Phys Med Biol*** **57**, 241-256 (2012).

23 van Engelen, A. ***et al.*** Atherosclerotic plaque component segmentation in combined carotid MRI and CTA data incorporating class label uncertainty. ***PLoS One*** **9**, e94840 (2014).

24 Wijeyaratne, S. M., Abbott, C. R. & Gough, M. J. A modification to the standard technique for carotid endarterectomy allowing removal of intact endarterectomy specimens: implications for research and quality control of preoperative imaging. ***Eur J Vasc Endovasc Surg*** **23**, 370-371 (2002).

25 Yushkevich, P. A. ***et al.*** User-guided 3D active contour segmentation of anatomical structures: significantly improved efficiency and reliability. ***Neuroimage*** **31**, 1116-1128 (2006).
26 Cibis, M. ***et al.*** Wall shear stress calculations based on 3D cine phase contrast MRI and computational fluid dynamics: a comparison study in healthy carotid arteries. ***NMR Biomed*** **27**, 826-834 (2014).
27 Groen, H. C. ***et al.*** MRI-based quantification of outflow boundary conditions for computational fluid dynamics of stenosed human carotid arteries. ***J Biomech*** **43**, 2332-2338 (2010).
28 Klein, S., Staring, M., Murphy, K., Viergever, M. A. & Pluim, J. P. elastix: a toolbox for intensity-based medical image registration. ***IEEE Trans Med Imaging*** **29**, 196-205 (2010).
29 Timmins, L. H. ***et al.*** Focal association between wall shear stress and clinical coronary artery disease progression. ***Ann Biomed Eng*** **43**, 94-106 (2015).
30 Antiga, L. ***et al.*** An image-based modeling framework for patient-specific computational hemodynamics. ***Med Biol Eng Comput*** **46**, 1097-1112 (2008).
31 Antiga, L. Patient-specific modeling of geometry and blood flow in large arteries. ***Politecnico di Milano*** (2002).
32 van den Bouwhuijsen, Q. J. ***et al.*** Determinants of magnetic resonance imaging detected carotid plaque components: the Rotterdam Study. ***Eur Heart J*** **33**, 221-229 (2012).
33 Saam, T. ***et al.*** Quantitative evaluation of carotid plaque composition by in vivo MRI. ***Arterioscler Thromb Vasc Biol*** **25**, 234-239 (2005).
34 Potters, W. V., van Ooij, P., Marquering, H., vanBavel, E. & Nederveen, A. J. Volumetric arterial wall shear stress calculation based on cine phase contrast MRI. ***J Magn Reson Imaging*** **41**, 505-516 (2015).

Chapter 3 The correlation between WSS and plaque composition in advanced human carotid atherosclerosis – assessment of registered MRI-based WSS and histology

Astrid M. Moerman, Suze-Anne Korteland, Kristine Dilba, Kim Van Gaalen, Dirk H.J. Poot, Aad van der Lugt, Hence J.M. Verhagen, Antonius F.W. van der Steen, Frank J.H. Gijsen, Kim van der Heiden

Abstract

The role of wall shear stress (WSS) in atherosclerotic plaque development is evident, but the relation between WSS and plaque composition in advanced atherosclerosis, potentially resulting in plaque destabilization, is a topic of discussion. Using a previously developed image registration pipeline, we investigated the relation between two WSS metrics, time-averaged WSS (TAWSS) and the oscillatory shear index (OSI), and the local histologically-determined plaque composition in a set of human advanced carotid plaques. WSS values were subdivided into patient-specific low, mid and high tertiles. This cross-sectional study shows a relation between necrotic core (NC) size and high TAWSS, as well as relations between low OSI and both macrophage area and cap thickness. When limiting the analysis to intimal depths of 250 μm and 400 μm from the lumen, relations between WSS and compositional features of vulnerability were not found. Local TAWSS and OSI tertile values were generally inversely related, as described in literature, but other combinations were also found. Vulnerability features that were related to low OSI, did not show a significant relation with high TAWSS. This illustrates that TAWSS and OSI are independent metrics in relation to plaque vulnerability.

Introduction

Atherosclerosis is a gradually progressing disease of arteries characterized by vessel wall thickening due to accumulation of lipids and inflammatory cells originating from the blood. This is referred to as plaque formation. Atherosclerosis is a multifactorial disease, that can be aggravated by lifestyle factors such as high caloric diet, physical inactivity and smoking, but also by genetic factors. The initiation of plaque formation however, has been strongly linked to a hemodynamic parameter: wall shear stress (WSS). WSS is the frictional force exerted by the flowing blood on the vessel wall. Atherosclerotic plaques form at predetermined locations, where WSS is low and/or oscillatory, which increases endothelial cell permeability and subsequent retention of lipoproteins [1], and regulates pro-inflammatory signaling pathways in the endothelium, resulting in increased influx of inflammatory cells [2]. The causal role of WSS in plaque initiation is evident [3,4], however the influence of WSS on plaque progression is less clear. Initial plaque growth is generally accompanied by outward remodeling and preservation of low and/or oscillatory WSS levels. With disease progression however, plaques will start to intrude the lumen, thereby affecting local hemodynamics. Upstream and at the throat of the plaque, WSS levels are high, while low WSS is found downstream [5]. Based on their composition and resulting risk of rupture, plaques are classified as stable or vulnerable. Vulnerable plaques

are characterized by a thin cap, covering a large necrotic core (NC) and often present with high inflammatory activity and decreased smooth muscle cell content [6]. Intra-plaque hemorrhage (IPH) can also be present [7]. The morphology and composition of advanced plaques was shown to be inhomogeneous, both in axial and in circumferential direction [8–12], which suggests a relation between local hemodynamics and plaque composition. In addition, plaque rupture is most often encountered at the high WSS-exposed upstream site [13]. The interplay between WSS and plaque composition is a subject of debate: both low and high WSS have been linked to features of plaque vulnerability [12,14–19]. However, these studies differ in imaging modality used for assessing plaque composition, complicating one-to-one comparison of their results. In addition, studies in the carotid artery are often based on surrogate imaging markers of WSS [11,18,20] or used animal models, which are not truly representative [21,22]. Since histology is the gold standard for assessment of human plaque composition in high resolution, we have previously developed a framework for accurate registration of MRI-derived WSS patterns to histological cross-sections [23]. In this study, we investigated the correlation between WSS and histologically-identified components of plaque vulnerability in a dataset of advanced human carotid atherosclerotic plaques.

Methods

MR imaging, tissue collection and histological processing

MR imaging, tissue collection, tissue processing and image registration procedures have been described in detail elsewhere 23. In short, we imaged the carotid bifurcations of eleven patients scheduled for carotid endarterectomy (CEA) surgery in a 3.0 T MRI scanner (GE Healthcare, Milwaukee, USA). The MRI protocol consisted of a black blood 3D fast spin echo (3D-BB-FSE) sequence with variable flip angles (TR/TE: 1000/16 ms, FOV: 15 cm, slice thickness: 0.8 mm, matrix: 160x160, number of excitations 1, scan time: 190 s), which was optimized for visualizing lumen and outer wall geometry. After surgery, CEA specimens were collected within 30 minutes after surgical resection and snap frozen in liquid nitrogen and stored at -80°C until *ex vivo* scans and histology were performed. Upon processing, CEA specimens were thawed, fixed in 4% formaldehyde and immersed in PBS. *Ex vivo* MRI scans (T2w fast recovery FSE (frFSE) (TR/TE: 2500/66 ms, in-plane resolution: 0.1 x 0.1 mm, slice thickness: 0.5 mm, matrix: 256x256, scan time: ~20 min, number of slices: 66) were made using a 7.0 T MRI scanner (7.0T Discovery MR901, GE Healthcare, Milwaukee, USA).
CEA specimens were decalcified and cut into 1 mm thick consecutive axial

cross-sections. 'En face photos' were taken (IXUS 60, Canon, Tokyo, Japan) of the proximal side of each cross-section. The en face photos contained landmarks to facilitate registration of each en face photo to the photo of the adjacent cross-section, enabling reconstruction of a 3D stack of en face photos. After photographing, the 1 mm thick axial cross-sections were embedded in paraffin. Each paraffin block was cut into consecutive 5 µm thick sections, which were processed for a series of histochemical staining procedures, i.e. Miller's elastic stain, hematoxilyn-eosin, Martius scarlet blue and picro-sirius red, as well as two immuno-histological staining procedures for macrophages (CD68, Abcam, UK) and endothelial cells (CD31, Abcam, UK). For each tissue section, compositional characteristics of plaque vulnerability, i.e. necrotic core (NC) and the IPH-associated protein fibrin were delineated in a segmentation image. This segmentation was based on the total set of histochemical stains. Based on the immuno-histological staining for CD68, we made segmentation masks of the CD68-positive pixels by applying a color deconvolution filter in Fiji [24,25]. Tissue areas containing artefacts and NC led to false positive results and were subtracted from the CD68-positive pixel selection.

Computational Fluid Dynamics for WSS calculation

Lumen contours of the stenosed bifurcations were delineated on the *in vivo* MRI scan using ITK-snap [26] and exported as surface geometry. VMTK [27] was used for surface smoothing and centerline calculation. Clipping of inlet and outlets normal to the centerline was performed in ICEM (ANSYS ICEM 17.1, USA) and flow extensions were applied on inlet and outlets using VMTK. The length of the added flow extensions was 5 times the radius of the inlet or outlets. Subsequently, ICEM was used to generate a volume mesh containing on average 7 million elements. The volume mesh consisted of tetrahedral elements with 5 layers of prism elements at the wall. On the inlet of the common carotid artery (CCA), we applied a transient flow velocity profile using the theory of Womersley [28]. This transient profile was based on the average flow waveform over one heartcycle and the heartrate reported by Lee [29]. For each patient the transient flow waveform was scaled to obtain an average WSS in the common carotid artery of 0.9 Pa. As outlet boundary condition the relative outflow to the internal carotid artery (ICA) and external carotid artery (ECA) was defined based on the stenosis degree [34]. Blood density was set to 1060 kg/m^3 and non-Newtonian fluid behavior was mimicked by the Carreau-Yasuda model using the parameters reported in [35]. The Navier-Stokes equations were solved numerically (ANSYS Fluent 17.1, USA) (convergence criteria: 1E-4 for continuity residual, 1E-5 for x-velocity, y-velocity, z-velocity residuals, time step was 0.004 seconds) over 2 heartcycles. Time-dependent time-averaged wall shear stress (TAWSS)

and oscillatory shear index (OSI) [36] were computed over the second heartcycle to account for initialization effects.

Image registration of MRI, CFD and histology

Image registration was performed according to the methods we previously described in Moerman et al. [23]. In short, via a series of rigid and non-rigid image registrations and transformations, the *in vivo* MRI lumen and its corresponding WSS map were transformed to consecutively the *ex vivo* and the en face image domain. Histology images were axially stacked and registered to the en face domain as well, resulting in a co-registration of *in vivo* MRI-derived WSS and histology.

Analysis and exclusion criteria

For a detailed description of data selection and analysis procedures we refer to our previous publication [23]. In short, WSS patterns were axially averaged over -0.3 mm to +0.3 mm with respect to the axial location of the nearest histology section. Transversally, the WSS distribution over each lumen was discretized into eight radial bins (bin radius 45 degrees). Points on the centerline of the transformed 3D WSS map were used as center points to create the radial bins. Plaque component measures were averaged in each radial bin. Per bin, we investigated the relation between local WSS and tissue composition of 1) the total intima depth and of 2) depths of 250 µm and 400 µm from the lumen. Plaque composition at a depth of 250 µm might reflect the direct influence of WSS on endothelial signaling, as protein-bound- and/or receptor-mediated responses are thought to be transported to a depth of 250 µm [37–39]. A depth of 400 µm might reflect the relation between WSS and passive diffusion of substances through the endothelium, a process that is thought to cross a distance of this order of magnitude [39].
We excluded data, both axial cross-sections and radial bins, based on a set of objectives. Axial cross-sections were excluded if: A) A part of the excised CEA lumen showed severe and non-uniform deformation with respect to the rest of the lumen, e.g. large lumen collapse in the ICA compared to the CCA. The applied non-rigid lumen registration algorithms act on the global 3D geometry and are not able to correct for local severe tissue deformations, thus accurate registration was impaired in such cross-sections. B) Lumen diameter on *in vivo* MRI was < 3 pixels and/or showed a very large axial gradient. As discussed previously [23] the applicability of our method should be carefully assessed in these cases, since WSS calculations in highly stenotic areas are very sensible to minor variations in lumen size and a small mismatch in registration accuracy

in regions with large axial gradients has a relatively large effect on the found relation between WSS and plaque composition. C) Low signal-to-noise of the *in vivo* MRI images, which impaired reliable lumen segmentation. Radial bins were excluded based on the presence of 1) Histological processing artefacts, 2) A mismatch in lumen registration between en face and histology images, or 3) A mismatch in lumen registration between *in vivo* MRI and en face images [23]. For the included radial bins, we quantified registration performance by calculating the average Hausdorff distance (HD) and Dice Similarity coefficients (DSC) between en face and histology lumen segmentations and en face and *in vivo* MRI lumen segmentations [23].

Statistical analysis

The range of absolute TAWSS and OSI values varied per artery. To define both low, mid and high WSS regions within each artery, patient-specific TAWSS and OSI tertiles were calculated. Statistical analysis was performed using a linear mixed effects model: WSS tertiles were set as fixed factor and patient as random factor. Bonferroni correction was applied to adjust for multiple comparisons between WSS tertiles. P-values < 0.05 were considered statistically significant.

Results

Registration performance

The dataset of 11 CEA samples yielded 183 axial cross-sections, of which 87 (48%) were included in the final analysis. 96 axial cross-sections were excluded; the majority of exclusions (59) were due to severe nonuniform deformation in the excised tissue or processing artefacts. 20 axial cross-sections were excluded because the *in vivo* lumen was highly stenotic or had a large axial gradient, impairing accurate lumen segmentation for CFD simulations. 17 cross-sections were excluded because of bad signal-to-noise on *in vivo* MRI. The 87 included axial cross-sections were divided into 8 radial bins, yielding a total of 696 radial bins of which 511 (73%) were included in the final analysis. The majority of excluded radial bins (111) presented with histological artefacts. Table 1 summarizes the results of the registration procedure.
After the exclusion procedure, registration accuracy of the remaining dataset was quantified by calculating the Dice Similarity Coefficient (DSC) and Hausdorff Distance (HD) between the lumen segmentations of the en face and histology cross-sections and between the en face and the transformed *in vivo* cross-sections. For the histology-to-en face registration, we found a mean HD

of 0.51 mm of and a mean DSC of 0.87. The registration performance between *in vivo* MRI and en face was slightly better: mean HD was 0.32 mm and mean DSC was 0.92. These values were in the order of magnitude of previously reported similarity indices describing registration of images of CEA specimens by multiple imaging modalities [40].

Patient	*Axial 1 mm cross-sections included (included/total)*	*Radial bins included (included/total)*	*Mean DSC Hist-EF included radial bins*	*Mean DSC Inv-EF included radial bins*	*Mean HD Hist-EF included radial bins [mm]*	*Mean HD Inv-EF included radial bins [mm]*
1	10/20	55/80	0.85	0.96	0.64	0.23
2	9/25	50/72	0.86	0.96	0.58	0.30
3	5/12	31/40	0.90	0.97	0.47	0.22
4	5/22	24/40	0.72	0.71	1.10	0.83
5	7/19	49/56	0.88	0.94	0.42	0.28
6	10/15	53/80	0.88	0.95	0.57	0.24
7	7/14	39/56	0.89	0.96	0.37	0.25
8	12/20	87/96	0.90	0.90	0.38	0.36
9	12/17	77/96	0.88	0.91	0.38	0.28
10	4/10	14/32	0.82	0.79	0.39	0.46
11	6/9	32/48	0.82	0.93	0.70	0.51
Total included	87/183 (48%)	511/696 (73%)	0.87	0.92	0.51	0.32

Table 1: Results of registration procedure*. DSC = Dice Similarity Coefficient. HD = Hausdorff Distance. Hist-EF = histology-to-en face. Inv-EF = in vivo MRI-to-en face.*

WSS patterns in advanced carotid atherosclerosis

In Fig. 1 the TAWSS and OSI patterns on a carotid bifurcation are shown. In all included carotid arteries, relatively high TAWSS was mainly located at the flow divider, at the ECA inlet and upstream to and at locations of maximally narro-

wed lumen. Low TAWSS was mainly found in the proximal CCA, at the lateral side of the carotid bulb and at sites of relative lumen dilation. High OSI was generally found at the lateral side of the carotid bulb and downstream of stenoses, while low OSI was seen in relatively straight arterial segments such as the proximal CCA, and at sites of lumen narrowing. The range of absolute TAWSS and OSI values varied per artery. After registration of the WSS maps to histology, WSS values were axially and radially averaged. In Table 2 the patient-specific tertile boundaries and the ranges of average TAWSS and OSI values, after registration and averaging per bin, are reported. In Table 3, the co-occurrences of TAWSS and OSI tertile values are reported. An inverse relation between TAWSS and OSI tertile values was most frequently encountered, but other combinations were also found.

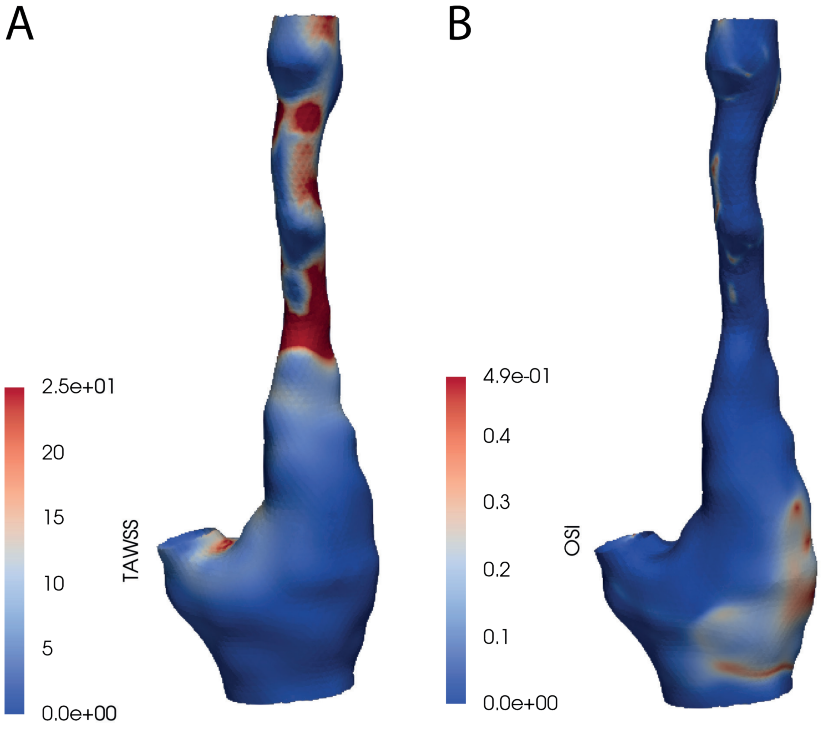

Figure 1: A. Time-averaged wall shear stress (TAWSS) and B. Oscillatory shear index (OSI) values on a carotid bifurcation included in the dataset.

Patient	TAWSS tertile boundary low-mid [Pa]	TAWSS tertile boundary mid-high [Pa]	Range TAWSS – averaged over bins [Pa]	OSI tertile boundary low-mid [Pa]	OSI tertile boundary mid-high [Pa]	Range OSI – averaged over bins [Pa]
1	2.1	4.5	0.5 – 10.4	0.003	0.010	0 - 0.092
2	1.0	1.9	0.3 – 3.8	0.004	0.018	0 - 0.386
3	1.5	2.0	1.0 – 3.3	0.000	0.001	0 - 0.005
4	1.3	2.0	0.5 - 3.5	0.011	0.021	0 - 0.169
5	1.1	2.5	0.2 - 8.0	0.001	0.014	0 - 0.093
6	1.2	2.8	0.5 - 34.8	0.002	0.044	0 - 0.344
7	1.1	2.9	0.2 – 6.0	0.002	0.008	0 - 0.111
8	0.6	1.5	0.2 – 5.8	0.007	0.032	0 - 0.232
9	1.8	8.8	0.1 – 52.6	0.000	0.013	0 - 0.308
10	1.7	2.7	1.0 – 11.1	0.000	0.004	0 - 0.091
11	0.8	2.5	0.3 - 11.7	0.004	0.031	0 - 0.156

Table 2: Patient-specific tertile boundaries and ranges of wall shear stress (WSS) metrics averaged on radial bins. *TAWSS: time-averaged WSS. OSI: oscillatory shear index.*

	Low OSI	*Mid OSI*	*High OSI*
Low TAWSS	11	38	120
Mid TAWSS	42	89	35
High TAWSS	116	39	14

Table 3: Co-occurrence of TAWSS and OSI tertiles. *An inverse relation between TAWSS and OSI tertile values was most frequently encountered (high TAWSS + low OSI or low TAWSS + high OSI). TAWSS: time-averaged WSS. OSI: oscillatory shear index.*

Histologically-determined plaque composition in advanced carotid atherosclerosis

In Fig. 2, a selection of histological cross-sections is shown, along with segmentation images. In general, histological cross-sections originating from the CCA showed a thickened intima with one or more NCs and small, elongated

patches of macrophages. Both the NCs and the macrophages were generally located from the lumen up to a depth of half of the intima (Fig. 2A). Relatively small fibrin areas could be observed as well. When moving from proximal to distal through the bulb, the plaque thickness varied in circumferential direction: plaque area and NC size were larger at the lateral side of the bifurcation (Fig. 2B, C). Largest plaque area and eccentric plaque growth were observed in cross-sections harvested from the ICA (Fig. 2D, E). Large NCs were present and showed large fibrin-positive areas. In these cross-sections, macrophages were generally distributed around the circumference of the lumen, were present in the cap, but also were also seen deeper in the intima, at the edges of the NCs (Fig. 2E). The amount of fibrous tissue was relatively low compared to proximal axial locations.

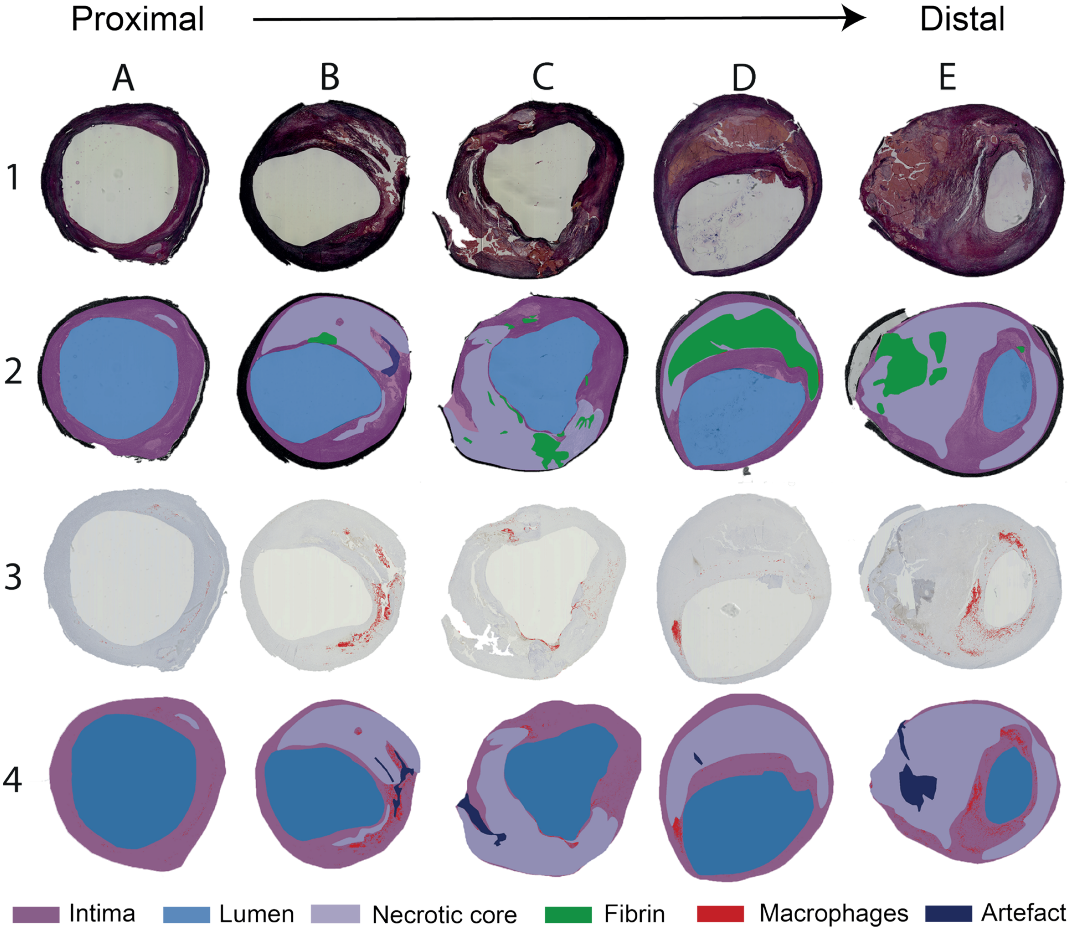

Figure 2: A-E. Selection of typical histology cross-sections of carotid plaques seen when moving from proximal to distal along the length of the carotid plaque. *Cross-*

sections A-C were seen proximal to the flow divider and D-E distal to the flow divider. Row 1: Miller's elastic stain. Row 2: segmentation of necrotic core (NC), fibrin and artefact, based on the combination of histochemical staining procedures performed. Row 3: CD68+ immuno-histochemical stain. CD68 positive areas are marked in red. Row 4: segmentation of CD68+ stained slides, showing macrophage areas, NC and artefacts.

Relation WSS metrics and plaque composition

For all included radial bins, we compared the averaged TAWSS and OSI levels, subdivided into patient-specific low, mid and high tertiles, to the composition of the underlying plaque (NC area, fibrin area, macrophage area, cap thickness). When considering the plaque composition of the total intimal area per radial bin, we found significantly larger NC areas in plaque regions exposed to high TAWSS, compared to low TAWSS ($p = 0.023$). In addition, we found significantly larger macrophage areas in regions exposed to low OSI than in regions exposed to mid ($p < 0.001$) or high OSI ($p = 0.005$). Thicker caps were seen at low OSI regions compared to high OSI ($p = 0.030$). These relations were only found when assessing the complete intima thickness. Relations between WSS and plaque composition at radii of 250 µm or 400 µm depth from the lumen were not found. In Fig. 3 the relations between WSS metrics and plaque composition are visualized.

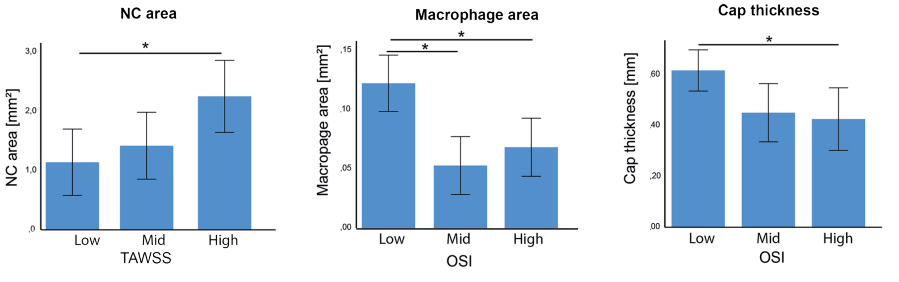

Figure 3: Relation between WSS metrics and plaque compositional characteristics. *At high TAWSS-exposed regions, larger NC area was found. At low OSI regions, larger macrophage area and thicker caps were found compared to respectively mid and high or high OSI regions.*

Discussion

This was the first study that was able to make a direct comparison between local WSS levels and histologically-determined compositional characteristics of plaque vulnerability in a substantial number of human plaques. The applied image registration pipeline allowed for a very accurate, localized assessment of

this relation. We were able to take into account not just axial, but also rotational matching of WSS and histology.
Our cross-sectional analysis showed a relation between NC size and high TAWSS, as well as relations between low OSI and both macrophage area and cap thickness in advanced carotid atherosclerosis. We did not find relations between WSS and vulnerability features, when limiting the analysis to intimal depths of 250 μm and 400 μm from the lumen. Previously reported relations between high TAWSS and cap thickness [41] in human coronaries, high TAWSS and IPH [17,42] in human carotids and between presumed high TAWSS because of upstream location [11,20] and increased macrophage area in human carotids were not present in this dataset.

WSS patterns in advanced carotid atherosclerosis

The TAWSS patterns observed in this set of carotid arteries were in line with findings previously described in literature [36,43–47]. That is, low TAWSS was present at the CCA, at the lateral side of the carotid bulb, while high TAWSS was mainly seen at the upstream side of lumen stenoses. Generally, an inverse relation between TAWSS and OSI was found, as described before [44]. However, a subset of radial bins showed other relations between these two WSS metrics. As inflow boundary conditions, we did not use measured patient-specific flow profiles, but applied estimated patient-specific flow profiles, scaled by inlet diameter. Yet, large variations in WSS and OSI values were still encountered between patients, which stresses the large influence of geometrical factors on WSS patterns. Because of the large variation in WSS ranges between patients, it would be impossible to draw conclusions on the relation between WSS and plaque composition by using absolute WSS values. Therefore, we calculated patient-specific WSS tertiles. The use of relative instead of absolute WSS levels has the additional advantage of diminishing the sensitivity of the CFD results to the approximated boundary conditions that were applied.

Histologically-determined plaque composition in advanced carotid atherosclerosis

The histologically-determined composition seen in this set of carotid plaques reflected histology results reported in literature [48.] That is, greatest plaque cross-sectional area and smallest lumens were found in the ICA, at cross-sections where the largest NCs were present, sometimes accompanied by fibrin-positivity, reflecting IPH. The majority of excluded axial cross-sections and radial bins presented with processing artefacts, especially in the distal part of the plaque. The relatively ‘soft’ necrotic and thrombotic tissue areas were more

prone to deformation than tissue areas containing a higher amount of fibrous tissue. In addition, the tissue structure at areas that contained high amount of calcium lost rigidity after decalcification, making these regions also susceptible to processing artefacts. The exclusion of these necrotic and calcified areas may have introduced a bias in our dataset towards moderately diseased tissue segments. The effect of this bias on the obtained results is unpredictable.

Relation WSS metrics and plaque composition

Our study was designed to assess the correlations between WSS metrics and a set of compositional features of plaque vulnerability in carotid plaques. We found that NC area was significantly higher at locations exposed to high TAWSS. Besides the existence of a direct correlation between TAWSS and NC size, this finding might be explained by the fact that progression of atherosclerosis is accompanied by plaque growth and subsequent lumen intrusion. This local lumen narrowing will affect TAWSS patterns, inducing a local high TAWSS at the upstream side and at the throat of the stenosis. In addition, plaque area has been shown to be correlated to NC size [41,49], a finding that links the co-existence of high TAWSS and NC size. A positive correlation between TAWSS and NC has been reported before in both carotid plaques [50], as well as in coronary plaques [16,41,51,52]. Although large NC size has been shown to be associated with rupture [53,54], based on this cross-sectional study, we cannot differentiate whether we are looking at a 'true' relation between WSS-induced NC growth and vulnerability or simply at the effect of stenosis-induced altered hemodynamics. Besides NC size, we did not find significant relations between TAWSS and the other characteristics of vulnerability investigated.
For OSI on the other hand, relations with cap thickness and macrophage infiltration, but not NC size, were found. We found significantly larger macrophage areas in plaque regions where OSI levels were low. At regions exposed to low OSI, we also found significantly thicker caps than at high OSI regions. To the best of our knowledge, relations between low OSI and vulnerability features in human plaques have not been reported before. The OSI value describes how much the WSS vector deviates from its average direction. Thus, low OSI, indicating a relative constant WSS direction, is mainly expected at regions with laminar flow, high flow velocity and high TAWSS, while high OSI is expected at regions of low flow velocity and low TAWSS. Indeed, in our dataset co-existences of either low OSI and high TAWSS or high OSI and low TAWSS were most frequently found. However, in our dataset, the vulnerability features that related to low OSI, i.e. macrophage area and cap thickness, were not significantly related to high TAWSS. It would be interesting to investigate the relation between plaque vulnerability features and different combinations of TAWSS and OSI tertile

values, e.g. low OSI and low TAWSS. Unfortunately, the different combinations of TAWSS and OSI tertile values were encountered in varying frequencies (Table 3), and the numbers in this dataset hamper further statistical analyses.

Implications of this study

The relation between WSS and plaque vulnerability has been a topic of discussion for many years. Finding a direct association between WSS and risk of rupture might guide diagnostic approaches to identify the patient at risk, or drive therapeutic development to stagnate disease progression. A combination of various study designs is necessary for finding evidence to reach these ultimate goals: both longitudinal studies, investigating the *in vivo* relation between WSS and plaque progression [55,56], *in vitro* assays, investigating the pathways underlying the response of endothelial cells to WSS, as well as cross-sectional investigations, proving the existence and applicability of these relations.
The variability in results between previous studies and ours might be due to different reasons. Firstly differences in geometry, size and/or origin of the vascular bed might influence the nature of a relation between plaque composition and a hemodynamic parameter such as WSS. This, in combination with the generally small sample sizes in this kind of studies, increases the likelihood of varying outcomes. Secondly, the degree of disease progression is likely to influence findings in cross-sectional setups. Thirdly, the study setup might be of influence. Only one previous study compared TAWSS and OSI to histologically-determined vulnerability features in four CEA samples [45] and found no correlations. In all other cross-sectional studies plaque composition was determined by *in vivo* imaging or relative WSS levels were assumed based on axial location instead of calculations.

Though histology is the gold standard for assessing plaque composition, correlation of WSS metrics to histology in human disease, as performed in this work, is only applicable if an endarterectomy procedure is performed, e.g. in the carotid, iliac or femoral artery, and is limited to highly advanced disease. For future applications of this pipeline, we could head into two directions. On one hand, we can investigate the relation between WSS, plaque composition and plaque mechanics by adding localized plaque mechanical parameters to the pipeline. On the other hand, we can optimize the registration framework for use in larger patient cohorts and less advanced disease. This would imply letting go of the histologically-determined plaque composition and use another imaging modality instead. As a first step, a modification of this pipeline could then be used for finding the optimal *in vivo* imaging procedure to obtain high-resolution, 'histology-alike' information on plaque composition.

References

1. Lusis, A. J. Atherosclerosis. ***Nature*** **407**, 233–241 (2000).
2. Gimbrone, M. A. & García-Cardeña, G. Vascular endothelium, hemodynamics, and the pathobiology of atherosclerosis. doi:10.1016/j.carpath.2012.06.006.
3. Cunningham, K. S. & Gotlieb, A. I. The role of shear stress in the pathogenesis of atherosclerosis. ***Lab Invest*** **85**, 9–23 (2005).
4. Kwak, B. R. ***et al.*** Basic science for the clinician Biomechanical factors in atherosclerosis: mechanisms and clinical implications †. doi:10.1093/eurheartj/ehu353.
5. Slager, C. J. ***et al.*** The role of shear stress in the destabilization of vulnerable plaques and related therapeutic implications. ***Nat Clin Pr. Cardiovasc Med*** **2**, 456–464 (2005).
6. Schaar, J. A. ***et al.*** Terminology for high-risk and vulnerable coronary artery plaques. ***Eur. Heart J.*** **25**, 1077–1082 (2004).
7. Virmani, R., Kolodgie, F. D., Burke, A. P., Farb, A. & Schwartz, S. M. Lessons from sudden coronary death: a comprehensive morphological classification scheme for atherosclerotic lesions. ***Arter. Thromb Vasc Biol*** **20**, 1262–1275 (2000).
8. Wentzel, J. J. ***et al.*** Extension of increased atherosclerotic wall thickness into high shear stress regions is associated with loss of compensatory remodeling. ***Circulation*** **108**, 17–23 (2003).
9. Burke, A. P. ***et al.*** Plaque rupture and sudden death related to exertion in men with coronary artery disease. ***J. Am. Med. Assoc.*** **281**, 921–926 (1999).
10. Richardson, P. D., Davies, M. J. & Born, G. V. R. Influence of plaque configuration and stress distribution onfissuring of coronary atherosclerotic plaques. ***Lancet*** **334**, 941–944 (1989).
11. Dirksen, M. T., van der Wal, A. C., van den Berg, F. M., van der Loos, C. M. & Becker, A. E. Distribution of inflammatory cells in atherosclerotic plaques relates to the direction of flow. ***Circulation*** **98**, 2000–2003 (1998).
12. Cicha, I. ***et al.*** Carotid plaque vulnerability: a positive feedback between hemodynamic and biochemical mechanisms. ***Stroke*** **42**, 3502–3510 (2011).
13. de Weert, T. T. ***et al.*** Atherosclerotic plaque surface morphology in the carotid bifurcation assessed with multidetector computed tomography angiography. ***Stroke*** **40**, 1334–1340 (2009).
14. Wentzel, J. J. ***et al.*** Endothelial shear stress in the evolution of coronary atherosclerotic plaque and vascular remodelling: current understanding and remaining questions. doi:10.1093/cvr/cvs217.
15. Vergallo, R. ***et al.*** Endothelial shear stress and coronary plaque characteristics in humans: combined frequency-domain optical coherence tomography and computational fluid dynamics study. ***Circ Cardiovasc Imaging*** **7**, 905–911 (2014).
16. Eshtehardi, P. ***et al.*** Association of coronary wall shear stress with atherosclerotic plaque burden, composition, and distribution in patients with coronary artery disease. ***J Am Hear. Assoc*** **1**, e002543 (2012).
17. Tuenter, A. ***et al.*** High shear stress relates to intraplaque haemorrhage in asymptomatic carotid plaques. ***Atherosclerosis*** **251**, 348–354 (2016).
18. Lovett, J. K. & Rothwell, P. M. Site of carotid plaque ulceration in relation to direction of blood flow: an angiographic and pathological study. ***Cerebrovasc Dis*** **16**, 369–375 (2003).
19. Yamamoto, E. ***et al.*** Endothelial Shear Stress and Plaque Erosion: A Computational Fluid Dynamics and Optical Coherence Tomography Study. ***JACC: Cardiovascular Imaging*** vol. 12 374–375 (2019).
20. Fagerberg, B. ***et al.*** Differences in Lesion Severity and Cellular Composition between in vivo Assessed Upstream and Downstream Sides of Human Symptomatic Carotid Atherosclerotic Plaques. ***J. Vasc. Res.*** **47**, 221–230 (2010).
21. Daugherty, A. ***et al.*** Recommendation on Design, Execution, and Reporting of Animal Atherosclerosis Studies: A Scientific Statement from the American Heart Association. ***Arterioscler. Thromb. Vasc. Biol.*** **37**, e131–e157 (2017).
22. Winkel, L. C., Hoogendoorn, A., Xing, R., Wentzel, J. J. & Van der Heiden, K. Animal models of surgically manipulated flow velocities to study shear stress-induced atherosclerosis. ***Atherosclerosis*** vol. 241 100–110 (2015).
23. Moerman, A. M. ***et al.*** An MRI-based method to register patient-specific wall shear stress data to histology. ***PLoS One*** **14**, e0217271 (2019).
24. Schindelin, J. ***et al.*** Fiji: An open-source platform for biological-image analysis. ***Nature Methods*** vol. 9 676–682 (2012).
25. Ruifrok, A. C. & Johnston, D. A. Quantification of histochemical staining by color deconvolution. ***Anal. Quant. Cytol. Histol.*** **23**, 291–299 (2001).

26. Yushkevich, P. A. ***et al.*** User-guided 3D active contour segmentation of anatomical structures: significantly improved efficiency and reliability. ***Neuroimage*** **31**, 1116–1128 (2006).
27. Antiga, L. ***et al.*** An image-based modeling framework for patient-specific computational hemodynamics. ***Med Biol Eng Comput*** **46**, 1097–1112 (2008).
28. Xu, P. ***et al.*** Assessment of boundary conditions for CFD simulation in human carotid artery. ***Biomech. Model. Mechanobiol.*** **17**, 1–17 (2018).
29. Lee, S. W., Antiga, L., Spence, J. D. & Steinman, D. A. Geometry of the carotid bifurcation predicts its exposure to disturbed flow. ***Stroke*** **39**, 2341–2347 (2008).
30. Lee, M. Y. ***et al.*** Association between hemodynamics in the common carotid artery and severity of carotid atherosclerosis in patients with essential hypertension. ***Am. J. Hypertens.*** **21**, 765–770 (2008).
31. Irace, C. ***et al.*** Human common carotid wall shear stress as a function of age and gender: A 12-year follow-up study. ***Age (Omaha).*** **34**, 1553–1562 (2012).
32. Carallo, C. ***et al.*** Evaluation of Common Carotid Hemodynamic Forces - Relations With Wall Thickening. ***Hypertension*** **34**, 217–221 (1999).
33. Gnasso, A. ***et al.*** In vivo association between low wall shear stress and plaque in subjects with asymmetrical carotid atherosclerosis. ***Stroke*** **28**, 993–998 (1997).
34. Groen, H. C. ***et al.*** MRI-based quantification of outflow boundary conditions for computational fluid dynamics of stenosed human carotid arteries. ***J Biomech*** **43**, 2332–2338 (2010).
35. Seo, T., Schachter, L. G. & Barakat, A. I. Computational Study of Fluid Mechanical Disturbance Induced by Endovascular Stents. ***Ann. Biomed. Eng.*** **33**, 444–456 (2005).
36. Ku, D. N., Giddens, D. P., Zarins, C. K. & Glagov, S. Pulsatile flow and atherosclerosis in the human carotid bifurcation. Positive correlation between plaque location and low oscillating shear stress. ***Arterioscler. An Off. J. Am. Hear. Assoc. Inc.*** **5**, 293–302 (1985).
37. Lovich, M. A., Creel, C., Hong, K., Hwang, C. W. & Edelman, E. R. Carrier proteins determine local pharmacokinetics and arterial distribution of paclitaxel. ***J. Pharm. Sci.*** **90**, 1324–1335 (2001).
38. Hwang, C. W. & Edelman, E. R. Arterial ultrastructure influences transport of locally delivered drugs. ***Circ. Res.*** **90**, 826–832 (2002).
39. Stein-Merlob. Atheroma susceptible to thrombosis exhibit imparied endothelial permeability in vivo as assessed by nanoparticle-based fluoresence molecular imaging. ***Circ Imaging*** **12**, 2715–2719 (2017).
40. Boekhoven, R. W., Lopata, R. G. P., van Sambeek, M. R., van de Vosse, F. N. & Rutten, M. C. M. A Novel Experimental Approach for Three-Dimensional Geometry Assessment of Calcified Human Stenotic Arteries inVitro. ***Ultrasound Med. Biol.*** **39**, 1875–1886 (2013).
41. Wentzel, J. J. ***et al.*** In vivo assessment of the relationship between shear stress and necrotic core in early and advanced coronary artery disease. ***EuroIntervention*** **9**, 989–995 (2013).
42. Groen, H. C. ***et al.*** Plaque rupture in the carotid artery is localized at the high shear stress region: a case report. ***Stroke*** **38**, 2379–2381 (2007).
43. van Ooij, P. ***et al.*** Spatial correlations between MRI-derived wall shear stress and vessel wall thickness in the carotid bifurcation. ***Eur Radiol Exp*** **2**, 27 (2018).
44. Gallo, D., Steinman, D. A. & Morbiducci, U. Insights into the co-localization of magnitude-based versus direction-based indicators of disturbed shear at the carotid bifurcation. ***J Biomech*** **49**, 2413–2419 (2016).
45. Kaazempur-Mofrad, M. R. ***et al.*** Characterization of the atherosclerotic carotid bifurcation using MRI, finite element modeling, and histology. ***Ann Biomed Eng*** **32**, 932–946 (2004).
46. Vamsi Krishna, C., Chandran Suja, V., Watton, P. N., Arakeri, J. H. & Gundiah, N. Shear stress rosettes capture the complex flow physics in diseased arteries. ***J. Biomech.*** (2020) doi:10.1016/j.jbiomech.2020.109721.
47. Ladisa, J. F. ***et al.*** Time-efficient patient-specific quantification of regional carotid artery fluid dynamics and spatial correlation with plaque burden. ***Med. Phys.*** **37**, 784–792 (2010).
48. Virmani, R., Ladich, E. R., Burke, A. P. & Kolodgie, F. D. Histopathology of carotid atherosclerotic disease. ***Neurosurgery*** **59**, S219-27; discussion S3-13 (2006).
49. Ahmadi, A. ***et al.*** Do Plaques Rapidly Progress Prior to Myocardial Infarction?: The Interplay between Plaque Vulnerability and Progression. ***Circulation Research*** vol. 117 99–104 (2015).
50. Yang, C. ***et al.*** Advanced human carotid plaque progression correlates positively with flow shear stress using follow-up scan data: an in vivo MRI multi-patient 3D FSI study. ***J Biomech*** **43**, 2530–2538 (2010).
51. Samady, H. ***et al.*** Coronary artery wall shear stress is associated with progression and transformation of atherosclerotic plaque and arterial remodeling in patients with coronary artery disease. ***Circulation*** **124**, 779–788 (2011).
52. Park, J. B. ***et al.*** Computational fluid dynamic measures of wall shear stress are related to coronary lesion characteristics. ***Heart*** **102**, 1655–1661 (2016).

53. Falk, E., Nakano, M., Bentzon, J. F., Finn, A. V & Virmani, R. Update on acute coronary syndromes: the pathologists' view. ***Eur. Heart J.*** **34**, 719–728 (2013).
54. Virmani, R., Burke, A. P., Farb, A. & Kolodgie, F. D. Pathology of the Vulnerable Plaque. ***J. Am. Coll. Cardiol.*** **47**, (2006).
55. Stone, P. H. ***et al.*** Role of Low Endothelial Shear Stress and Plaque Characteristics in the Prediction of Nonculprit Major Adverse Cardiac Events: The PROSPECT Study. ***JACC Cardiovasc Imaging*** **11**, 462–471 (2018).
56. Kumar, A. ***et al.*** High Coronary Shear Stress in Patients With Coronary Artery Disease Predicts Myocardial Infarction. ***J Am Coll Cardiol*** **72**, 1926–1935 (2018).

Chapter 4 Temporal and spatial changes in wall shear stress during atherosclerotic plaque progression in mice

Ruoyu Xing, Astrid M. Moerman, Yanto Ridwan, Mat J. Daemen, Anotius F.W. van der Steen, Frank J.H. Gijsen, Kim van der Heiden

Based on: Temporal and spatial changes in wall shear stress during atherosclerotic plaque progression in mice, Royal Society Open Science, 2018

Abstract

Wall shear stress (WSS) is involved in atherosclerotic plaque initiation, yet its role in plaque progression remains unclear. We aimed to study 1) the temporal and spatial changes in WSS over a growing plaque and 2) the correlation between WSS and plaque composition, using animal-specific data in an atherosclerotic mouse model. Tapered casts were placed around the right common carotid arteries (RCCA) of ApoE$^{-/-}$ mice. At 5, 7 and 9 weeks after cast placement, RCCA geometry was reconstructed using contrast-enhanced micro-CT. Lumen narrowing was observed in all mice, indicating the progression of a lumen intruding plaque. Next, we determined the flow rate in the RCCA of each mouse using Doppler Ultrasound and computed WSS at all time points. Over time, as the plaque developed and further intruded into the lumen, absolute WSS significantly decreased. Finally at week 9, plaque composition was histologically characterized. The proximal part of the plaque was small and eccentric, exposed to relatively lower WSS. Close to the cast a larger and concentric plaque was present, exposed to relatively higher WSS. Lower WSS was significantly correlated to the accumulation of macrophages in the eccentric plaque. When pooling data of all animals, correlation between WSS and plaque composition was weak and no longer statistically significant. In conclusion, our data showed that in our mouse model absolute WSS strikingly decreased during disease progression, which was significantly correlated to plaque area and macrophage content. Besides, our study demonstrates the necessity to analyze individual animals and plaques when studying correlations between WSS and plaque composition.

Introduction

Wall shear stress (WSS) is the frictional force induced by blood flow acting on the endothelial lining of the vessel surface. WSS regulates the inflammatory status of the endothelium and thus determines the location of plaque development [1–3]. The progression of a plaque is a dynamic process, during which vessel geometry undergoes remodeling and narrowing, leading to substantial changes in the local WSS environment over time [4–7]. As the disease advances, plaques grow and they differ in composition, showing either a stable or vulnerable phenotype. Vulnerable plaques are characterized by the presence of a large necrotic core with a thin overlying fibrous cap and abundant infiltration of inflammatory cells [8]. Vulnerable plaques are prone to rupture and can cause subsequent thromboembolic events [9]. A substantial role for WSS in the initiation of atherosclerosis is established, however, whether WSS plays a role in plaque growth and/or progression remains under debate. Evidence towards a role

for WSS in plaque growth and progression does exist but is ambiguous. Clinical studies revealed that in carotid and coronary arteries, plaque rupture was predominantly located at the upstream shoulder of a plaque [10–13]. Plaque composition was heterogeneous along the direction of blood flow: thinner fibrous caps, larger necrotic cores and accumulation of macrophages were observed at the upstream shoulder of a plaque, correlating a vulnerable plaque phenotype to the location of rupture [12,14–17]. Several studies proposed that these regions were exposed to increased WSS, suggesting that high WSS may promote plaque vulnerability [18–21].

In contrast, low WSS was correlated to characteristics of plaque vulnerability in human and porcine coronary arteries [22–30]. Nevertheless, no direct association between evolution of WSS and plaque composition was established. We set out to study the dynamic process of disease progression and the concomitant spatial and temporal changes in lumen geometry and WSS using an atherosclerotic mouse model. In addition, we analyzed the association between WSS and plaque composition.

We use an atherosclerotic animal model in which we can manipulate WSS *in vivo* and induce atherosclerotic plaque development [31–37]. We previously summarized the use of surgically manipulated flow models [38] and found that WSS distribution was studied only in some of these models and usually not taking full 3D vessel geometry into account [34,36,39], while calculation of WSS critically depends on detailed vessel geometry and blood flow velocity [40]. In a previous cross-sectional study, using a tapered cast model [33], Pedrigi et al [37] discovered that certain WSS metrics co-localized to the presence of a plaque with increased Oil Red O-lipid-staining. However, quantitative analysis of plaque composition was not performed in this study and thus spatial correlations between WSS metrics and plaque composition could not be studied. The WSS metrics were investigated only at one time point while temporal data were lacking. Due to the dynamic nature of plaque progression, monitoring WSS *in vivo* over time is a prerequisite. To the best of our knowledge, no studies have monitored temporal and spatial changes of WSS or correlated these to plaque composition in individual animals. We investigated the evolution of geometry, flow and WSS during plaque progression and the correlation between WSS and plaque composition in individual animals by analyzing WSS *in vivo* at various time points during plaque progression. First, we obtained mouse-specific geometrical and flow data to compute WSS distribution at 5, 7 and 9 weeks after cast placement. This enabled us to monitor changes in WSS over the very same plaque during its growth and progression into an advanced plaque. At 9 weeks after cast placement, vessel samples were harvested and plaque composition was histologically characterized. Finally, regression analysis was performed to determine correlations between plaque composition and WSS.

Methods

Animals and cast placement

Female ApoE$^{-/-}$ mice on C57BL/6J background (n = 9) were purchased from Charles River (Maastricht, The Netherlands). At 13 weeks of age, normal chow diet was replaced with an atherogenic Western diet and provided *ad libitum* (Arie Blok, The Netherlands). Cast surgery was performed two weeks later on the animals under isoflurane-induced anesthesia as described previously [33,41,42]. The average weight of the mice was 21.9 grams. A tapering cast was placed around the right common carotid artery (RCCA), leading to changes in local WSS environment and subsequent plaque development. All animal experiments were performed conform to the guidelines from Directive 2010/63/EU of the European Parliament on the protection of animals used for scientific purposes and approved by ethical committee of Erasmus MC Rotterdam.

Contrast-enhanced micro-CT imaging and RCCA lumen reconstruction

To compute WSS in RCCA, we used time point and mouse-specific vessel geometries as the input, which was captured by contrast-enhanced micro-CT imaging (Quantum FX) with isotropic resolution of 40 μm. Images in Hounsfield unit (HU) were reconstructed. RCCA geometry of each animal at week 5, 7 and 9 was analyzed using in-house developed modules in MeVisLab (MeVisLab 2.2.1) and Matlab (Matlab 2012). The segmentation protocol was previously established [40]. RCCA lumen surface was reconstructed from its origin at the bifurcation of the brachiocephalic artery, to its bifurcation into the internal and external carotid artery. Mice were anesthetized with isoflurane with scanning parameters of 90kvp, 160μA, field of view 20mm (Fig 1). The radiation dose of each micro-CT scan was approximately 1.7 Gy. Mice underwent 3 scans in total, with 2 week time intervals. To determine a possible effect of radiation on atherosclerosis progression, we included a control group (n = 5) that was not imaged and analyzed plaque composition 9 weeks after cast placement. No significant differences in plaque area or macrophage content were found (data not shown). Contrast agent eXIA 160 was used with an injection dose of 150 μl/25 grams of body weight. One mouse had paralyzed hind limbs after the 1st imaging and was euthanized. One mouse was found dead before the 3rd imaging at week 9. These two mice were excluded from subsequent analyses. . Note that micro-CT is unable to capture outward remodeling of the vessel wall but allows visualization of lumen surface.

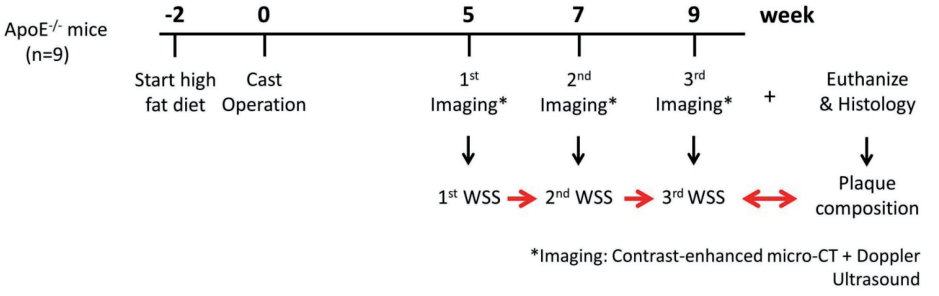

Figure 1: Experimental scheme. *At t = -2 weeks, ApoE-/- mice were fed a high fat diet; Cast operation was performed on the right common carotid artery (RCCA) at t=0 week to induce plaque growth (Note that at t = 0, mice were 15 weeks of age); At t = 5, 7, 9 weeks during plaque progression, 3D RCCA vessel geometry was reconstructed using contrast-enhanced micro-CT imaging. Blood flow velocity through the RCCA was measured by Doppler Ultrasound; Both micro-CT and ultrasound were carried out in each individual mouse; 3D WSS maps at 3 time points of the same animal were thus generated using these imaging data; After the last imaging moment at t = 9 weeks, animals were euthanized, RCCA was excised for histological analyses.*

Doppler Ultrasound imaging

Ultrasound imaging was performed using Vevo 2100 (VisualSonics) with a 40-MHz transducer. Blood velocity wave form was measured upstream of the RCCA under pulse-wave mode at 5 different time points: before and immediately after cast surgery, at 5, 7 and 9 weeks after cast surgery (Fig 1). RCCA diameter was measured under M-mode at the same location of the pulse-wave measurement, thus allowing conversion of blood velocity (mm/s) to flow (mm^3/s) assuming a parabolic velocity profile.

Mesh and CFD simulations

RCCA lumen surface was smoothed using Vascular Modelling Tool Kit (VMTK 1.2). The superfluous ends at the proximal and distal side of the vessel surface were clipped and flow extensions were added. A volume mesh with prism layers was then generated using ICEM (ICEM-CFD 14.5, Ansys). Parameters including number of mesh elements, maximum element size, use of curvature/proximity based refinement, numbers and thickness of prism layers were optimized to obtain a mesh-independent solution resulting in approximately 640,000 elements. Surface area of the RCCA inlet was derived, enabling the calculation of location-specific blood flow velocity as boundary condition. Several assumptions were made when solving the Navier-Stokes equations. First, the endothelial cells are exposed to time varying WSS levels. It is well

established that the response of these cells is triggered by the time-averaged WSS that they are exposed to [43]. To obtain the time-averaged WSS, we can use steady flow simulations, using the average flow through the vessel as input [44]. In previous studies, it was demonstrated that other time dependent WSS derived parameters such as Oscillatory Shear Index (OSI) are not relevant due the geometry and flow conditions in this model [37,40], unlike in other vascular territories [45,46]. Furthermore, we assumed the WSS values are not influenced by the distensibility of the vessel wall. For blood flow in carotid arteries in mice, it was previously shown that distensibility is only important in the carotid bifurcation, and has a negligible effect in the common carotid artery [47]. Finally, blood was modeled as a Newtonian fluid, a valid assumption given the high shear rates in the carotid arteries of mice [48]. Therefore, we confined ourselves to steady flow simulation.

The resulting Navier-Stokes equations were solved by computational fluid dynamics (CFD) using Fluent (Fluent 14.5, Ansys). Blood was modeled to be incompressible. A constant viscosity of 3.5×10^{-3} kg/m/s and a density of 1060 kg/m^3 were used [47,49]. Vessel wall was assumed to be rigid. A parabolic velocity profile was imposed as inlet boundary condition. Average blood flow velocity of the RCCA was derived from Doppler velocity measurements. For outlet boundary condition, zero pressure was used. WSS was then derived from the computed velocity field. Finally, post-processing and analysis were performed using CFD-Post (CFD-Post 14.5, Ansys) and Matlab.

Histological staining and analysis

After final imaging at week 9 (Fig. 1), mice were euthanized by isoflurane overdose. The vascular system was then flushed with PBS through the left ventricle. Subsequently, 4% paraformaldehyde (PFA) in 0.15 mM PBS was used for pressure fixation at 100 mmHg [50]. Tissue around the RCCA was carefully cleaned, exposing the vasculature. The RCCA, cast, proximal brachiocephalic bifurcation and aortic arch could be clearly seen (Fig. 2B). Photos of RCCA were taken with a 1 mm grid strip. The cast was then carefully removed from the vessel. Proximally, the RCCA was excised 3 mm distal to the aortic arch and distally after the carotid bifurcation. RCCA was then immersed in 4% PFA for 24h at room temperature. Tissue samples were then processed and embedded in paraffin for histological analysis. We focused on the plaque upstream of the cast because its composition was relevant to our aim of study. We did not investigate the region within the cast because this region was exposed to increased WSS, and thus no plaque formation was observed. For the region downstream of the constriction, the cast was generally located close to the bifurcation. We can therefore expect a strong interplay between the presence

of the jet downstream of the cast and the flow features associated with the division of the flow in the carotid bifurcation. These features will be greatly influenced by the flow division over the internal and external carotid artery. This ratio will change during the progression of the disease [47]. Since we did not measure flow in the internal or external carotid artery due to restricted time allocated for flow measurements, we cannot establish flow division and thus cannot evaluate WSS patterns downstream of the cast reliably. Therefore, we decided to exclude the plaque formed downstream in our analysis. Serial sections of the plaque upstream to the cast were collected. On average each plaque contains 21 serial sections (5 µm, at 50 µm interval), the two sections adjacent to the cast were excluded from the analysis to avoid possible confounding effects from the presence of the cast. Sections were stained for general plaque morphology (H&E), macrophages (CD68, Bio-Rad), endothelium (CD31, Dianova), and collagen (Resorcin-Fuchsine). Atherosclerotic plaque area, media area, and relative macrophage area were quantified (BioPix iQ3.2). Necrotic core was defined as a-cellular, a-nuclear areas, free of H&E staining [51].

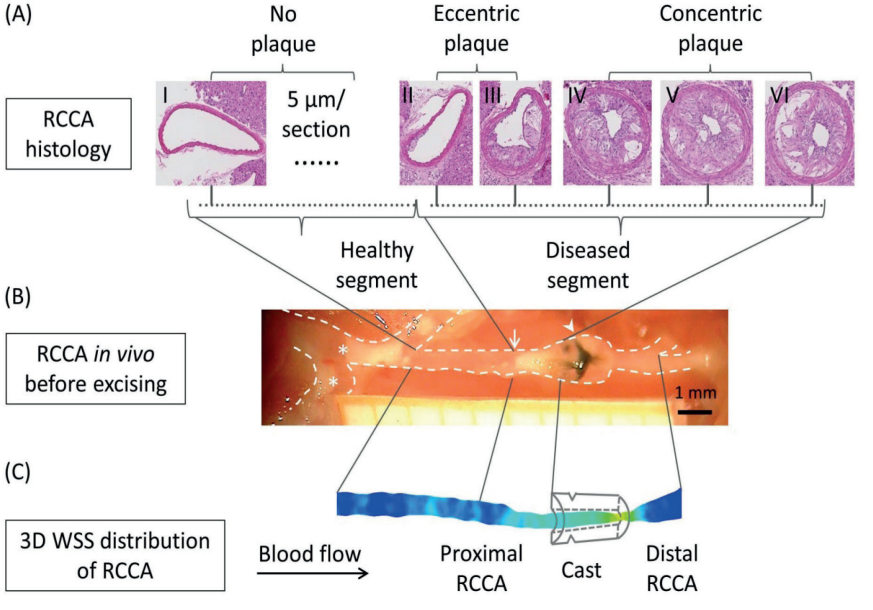

Figure 2: Spatial matching of histological sections to 3D WSS map of an individual RCCA. *(A) Representative H&E stained sections of the RCCA proximal to the cast, showing the healthy part, eccentric plaque part and the concentric plaque part. (B) Overview of the RCCA in situ before excision with 1 mm-spacing grid paper (Arrowhead: black suture around the cast; Arrow: proximal side of the plaque; Asterisk: plaques located at the inner curve of the aortic arch and brachiocephalic artery). (C) 3D WSS map.*

Registration of histological staining to 3D WSS maps

For each animal, histological sections of the RCCA (Fig. 2A) were spatially registered to 3D WSS maps at various time points (Fig. 2C) via the *in vivo* RCCA overview (Fig. 2B). We correlated plaque composition to WSS at different time points because although the effect of WSS on the endothelium is instant, the subsequent changes in plaque composition are not. Thus it is necessary to register WSS maps at week 5, 7, and 9 to plaque composition observed at the latest time point. To do the registration, we calculated RCCA vessel shrinkage from the *in vivo* situation to histology. Two landmarks are needed for this purpose. Since vessel segments with and without plaques were likely to exhibit different elasticity and therefore shrinkage, selection of landmarks should preferably be the beginning and the end of a plaque. The proximal edge of the plaque was clearly visible both on the RCCA overview (Fig. 2B, arrow) and histological sections (Fig. 2A, 2nd section on the left). We thus selected it as the first landmark. The end of the plaque coincided with the proximal edge of the cast, which can be identified on histology. However, due to the scar tissue surrounding the cast, the distal edge of the plaque was not clearly visible on the RCCA overview. The black suture around the cast, however, can be easily spotted (Fig. 2B, arrowhead). Since the distance to the proximal edge of the cast was known (0.5 mm), we could pinpoint it as our second landmark. The average longitudinal shrinkage was 51%±20%, comparable to that reported previously [37]. On the 3D WSS maps, location of the cast was identified from the micro-CT images. Using the individual shrinkage factor obtained for each mouse, histological sections were then spatially registered to the 3D WSS maps at week 5, 7 and 9 (Fig. 2C). We investigated the association between plaque composition and WSS profiles at 3 time points as the duration between changes in WSS and the actual effect of that particular WSS on plaques composition is unknown. According to the histological sections, proximal RCCA was divided into 2 segments: the healthy segment and the diseased segment. The corresponding segments were also identified on the 3D RCCA geometry reconstructed from the micro-CT images at week 9. Since histology was only available at week 9 and micro-CT imaging can only capture lumen geometry but not plaque composition, it was not possible to pinpoint the border between the healthy and diseased segment on the 3D RCCA geometry at week 5 and 7. We used the histology data obtained at week 9 to identify the healthy and diseased segments for these two time points. Lumen area in the proximal RCCA was derived from the 3D RCCA geometry assuming circular cross-section [52]. Degree of stenosis was calculated as the percentage ratio between the minimum lumen area in the diseased segment and the average lumen area of the healthy segment. When analyzing histological data, the diseased segment was further divided into two segments. Proximally, the plaque was composed of sections with eccentric pla-

que growth, in which plaque did not cover the entire circumferential direction. Close to the cast, the plaque covered the entire circumferential direction and was thus concentric (Fig. 2A).

Statistics

Data are presented as mean ± SD and analyzed in Matlab and RStudio. Differences between samples were evaluated using a paired, two-tailed, Student's t-test or repeated measures ANOVA. A Tukey's honestly significant difference (HSD) post-hoc test was performed after the ANOVA test. Correlations between histological quantifications and WSS data were performed by linear regression. A value of $p<0.05$ was considered significant.

Results

In vivo micro-CT reveals various plaque progression profiles among animals

3D RCCA vessel geometries were reconstructed from contrast-enhanced micro-CT at 5, 7 and 9 weeks after cast placement. Various plaque progression profiles were evident among animals. Changes in lumen diameter were most evident between either 7 and 9 weeks, or 5 and 7 weeks. In a representative animal (mouse number 1 shown in Fig 3-6), lumen narrowing was observed gradually over time (Fig. 3A, pink line, 3B). Degree of stenosis increased steadily from 55% at week 5 to 63% at week 7 and 80.0% at week 9 (Fig. 3A, pink line).
In all animals (n = 7), at week 5, lumen narrowing can be clearly seen in the diseased segment upstream of the cast (Suppl. Fig. 1), suggesting presence of a lumen intruding plaque. Degree of stenosis averaged among 7 animals was 41±11% at week 5, 57±8% at week 7 ($p<0.05$ vs. week 5) and 62±16% at week 9 ($p<0.05$ vs. week 5) (Fig. 3A, black line).

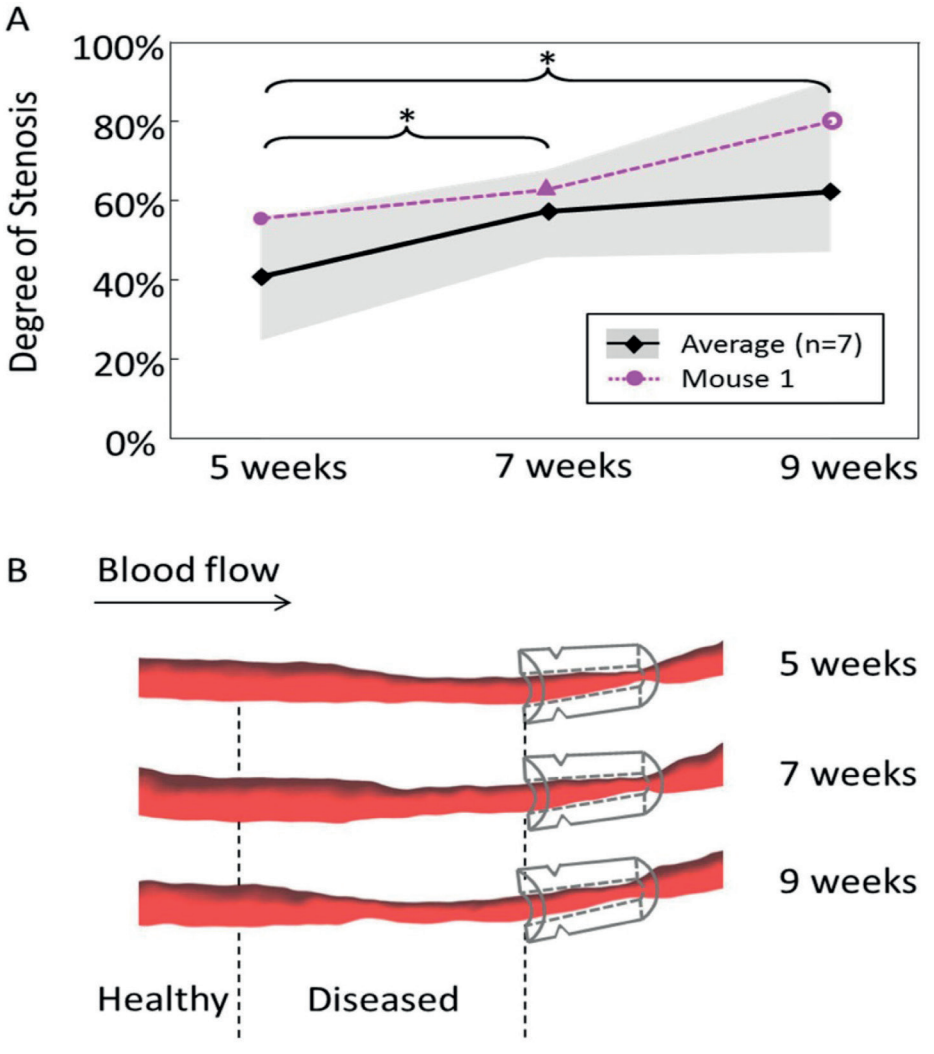

Figure 3: (A) Degree of stenosis of RCCA at 5, 7 and 9 weeks after cast placement: *Average of 7 animals (black line, *p<0.05, repeated measures ANOVA); Mouse 1 (pink line); Shadow area indicates data range of 7 animals. Notably, animals exhibited various plaque progression profiles. (B) 3D reconstruction of RCCA at 5, 7 and 9 weeks after cast placement of Mouse 1. Direction of blood flow is indicated by the arrow in the upper left corner. Location of the cast is illustrated. Upstream to the cast, the RCCA is divided into a healthy segment and a diseased segment based on the week 9 histology data. Lumen narrowing can be observed over time, suggesting the development and progression of a lumen intruding plaque.*

Blood flow in RCCA decreased over time

Blood velocity was measured upstream of the RCCA before and immediately after cast surgery, and at 5, 7 and 9 weeks after cast placement. Blood flow in the RCCA was then converted using the measured parameters. In our representative animal, blood flow reduced from 47.3 mm^3/s to 19.4 mm^3/s after cast placement and furthered decreased during plaque progression, from 14.8 mm^3/s at week 5 to 11.4 mm^3/s at week 7 and 2.0 mm^3/s at week 9 (Fig. 4, pink line).
All mice except for one (Mouse number 3 in Suppl. Fig. 1) showed a general decrease in blood flow over time. Blood flow in the RCCA averaged from all 7 animals decreased immediately after cast placement from 38.4±9.0 mm^3/s to 28.0±5.5 mm^3/s (Fig 4, black line). At week 5 and 7, blood flow further reduced to 19.8±9.2 mm^3/s and 16.4±6.0 mm^3/s ($p<0.05$ vs. before cast placement). Finally, at 9 weeks, blood flow was 9.9±11.3 mm^3/s, significantly lower than that before and after cast placement ($p<0.05$).

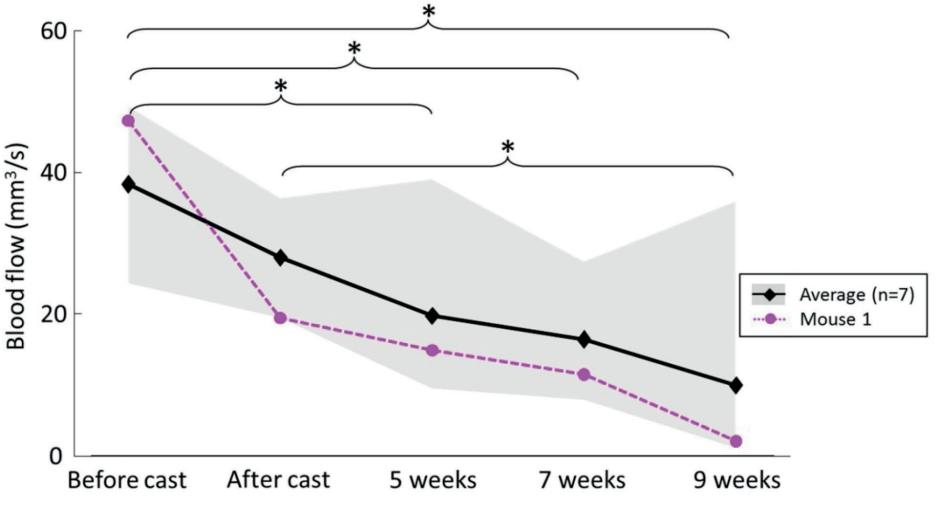

Figure 4: Blood flow along RCCA over time: *Average of 7 animals showed a general decrease in blood flow over time (black line, * indicates $p<0.05$, repeated measures ANOVA); Mouse 1 (pink line); Shadow area indicates data range of all animals.*

WSS profiles as determined by animal-specific geometry and flow data

The spatial and temporal 3D WSS distribution based on the mouse-specific geometry and flow data was computed at 5, 7 and 9 weeks after cast placement with CFD. Fig. 5 illustrates the evolution of the 3D WSS distribution of our representative animal. Before cast placement, average WSS was 14.4±9.4

Pa decreasing to 12.9±4.4 Pa after cast placement. At week 5, WSS was low upstream of the cast with an average value of 4.1±2.2 Pa (Fig. 5A, upper panel). At week 7 and 9, as blood flow in the RCCA gradually reduced, WSS decreased in the RCCA (Fig. 5A, middle and lower panel). WSS distribution in the RCCA upstream to the cast was further analyzed in the healthy and diseased segment. At week 5, the two segments were exposed to WSS of 2.2±0.1 Pa and 5.0±2.2 Pa respectively (Fig. 5C, green bars). Furthermore, WSS distribution was heterogeneous over the diseased segment (Fig. 5B, green line). Over time, as lumen area remained constant along the healthy segment, the decrease in blood flow lead to lower WSS in this region (Fig 5B, blue and red lines), with 1.3±0.1 Pa at week 7 and 0.3±0.0 Pa at week 9 ($p<0.05$, Fig. 5C, blue bars). For the diseased segment, the lumen area narrowed gradually over time. Combined with the reduction in blood flow over time, WSS in this segment decreased significantly to 3.4±1.7 Pa at week 7 and 1.7±1.0 Pa at week 9 ($p<0.05$, Fig. 5C, red bars). Since various geometry features and blood flow patterns were observed among the 7 mice, different WSS profiles were evident, presented in Suppl. Fig. 1. A general reduction in WSS over time was seen in 5 animals. Mouse number 2 showed an increase in WSS from 5 to 7 weeks, with a subsequent dramatic decrease from 7 to 9 weeks. Mouse number 3 was the only one showing a WSS increase over time, while in all other mice WSS was minimal in both the healthy and diseased segment at week 9. Furthermore, in all mice, the healthy segment was exposed to significantly lower levels of WSS when compared to the diseased segment at all time points.

Plaque morphology and composition varied within a single plaque

Histological analysis revealed the presence of one continuous plaque in the RCCA upstream to the cast 9 weeks after cast placement. However, differences in morphology and composition were found within this continuous plaque depending on the axial location. Histological sections of our representative animal are shown in Fig. 6. A smaller and eccentric plaque was observed proximally (Fig. 6, left section). Closer to the cast, the plaque was concentric and larger (Fig. 6, right section). Plaque area of the eccentric part was 0.04 mm^2 compared to that of the concentric plaque 0.15 mm^2. Relative macrophage area in the eccentric plaque was 24.6%, while in the concentric plaque a relative macrophage area of 13.9% was observed. In the eccentric plaque, relative necrotic core area was 2.7%, while it was 15.0% in the concentric plaque (data not shown).

The eccentric-concentric plaque morphology was present in all animals. Plaque

area was significantly smaller in the eccentric plaque compared to that of the concentric plaque (0.03±0.01 mm^2 vs. 0.12±0.02 mm^2, $p<0.05$) (Fig. 6A). Macrophages were more concentrated in the eccentric plaque compared to that of the concentric plaque (Fig. 6B). On average, relative macrophage area in the eccentric plaque was 28.3±6.9%, while in the concentric plaque a relative macrophage area of 13.4±3.5% was observed ($p<0.05$). In the eccentric plaque, relative necrotic core area appears to be somewhat smaller than that of the concentric plaque (Fig 6C, 15.2±8.2% vs. 21.1±7.7%). However, the difference between the eccentric and concentric plaque regarding relative necrotic core area was not statistically significant.

Correlation between WSS and plaque composition

Plaque area, macrophage content, and necrotic core area at week 9 was linked to WSS profiles at week 5, 7 and 9 (Fig. 7). In our representative animal, plaque area was positively associated with WSS and significant at all time points ($p<0.05$). Accumulation of macrophages was negatively correlated to WSS and significant at both week 5 and 7 ($p<0.05$), indicating that lower WSS suggested a pro-inflammatory profile in plaques. A positive correlation between relative necrotic core area and WSS level was positive at all 3 time points, however only significant at week 5 and 7. Fig. 7 summarizes the correlation between WSS and plaque area, macrophage content, and necrotic core area of all 7 animals at 3 time points. Thus for each plaque parameter, there were 7x3=21 observations. In 6 out of 7 animals at all time points, a positive and statistically significant correlation between WSS and plaque area was seen in 17 out of 21 observations. Inverse correlation between WSS and macrophages was observed in 6 out of 7 animals where 12/21 observations were statistically significant, and 6/21 showed a non-significant negative correlation. The correlations between WSS and relative necrotic core size showed less significance. For relative necrotic core size, 6/21 correlations were positive and statistically significant.
The correlation between plaque composition and WSS profiles were analyzed in each individual animal. When histological data from all the animals was pooled together, as is usually the followed approach in these types of studies, a positive but very weak correlation between WSS and plaque area was seen, which was not statistically significant at any time point (the correlation coefficient at week 5 was 0.08, 0.1 at week 7 and 0.04 at week 9, $p>0.05$), contrary to the result obtained from the individual animal analysis. Pooling data results in different and not necessarily correct correlation patterns.

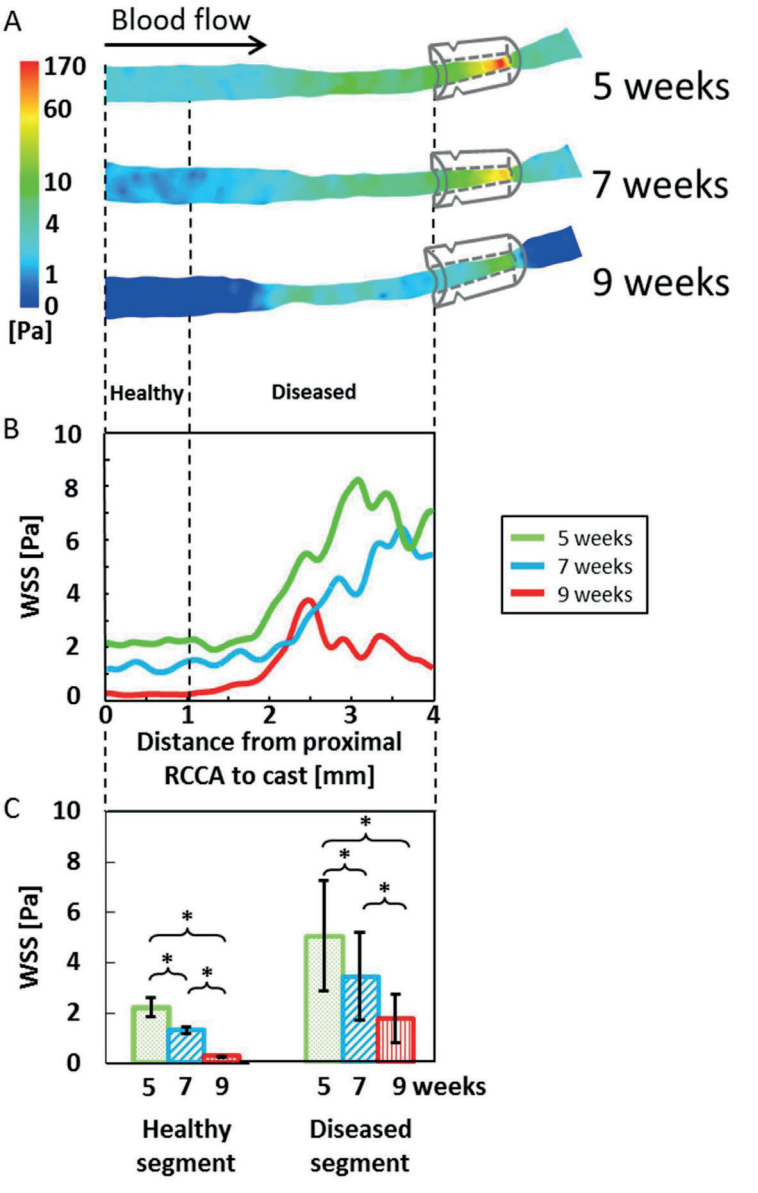

Figure 5: Illustration and quantification of WSS in a RCCA. *(A) 3D WSS distribution in the RCCA of representative mouse 1 at 5, 7 and 9 weeks after cast placement. Circumferentially-averaged WSS along the RCCA is shown (B). Proximally the RCCA was divided into a healthy and diseased segment, indicated by the vertical dashed line, based on the week 9 histology data. WSS distribution was heterogeneous over the diseased segment. Averaged WSS in both segments significantly decreased over time and was relatively higher in the diseased segment (Student's t-test, *p<0.05).*

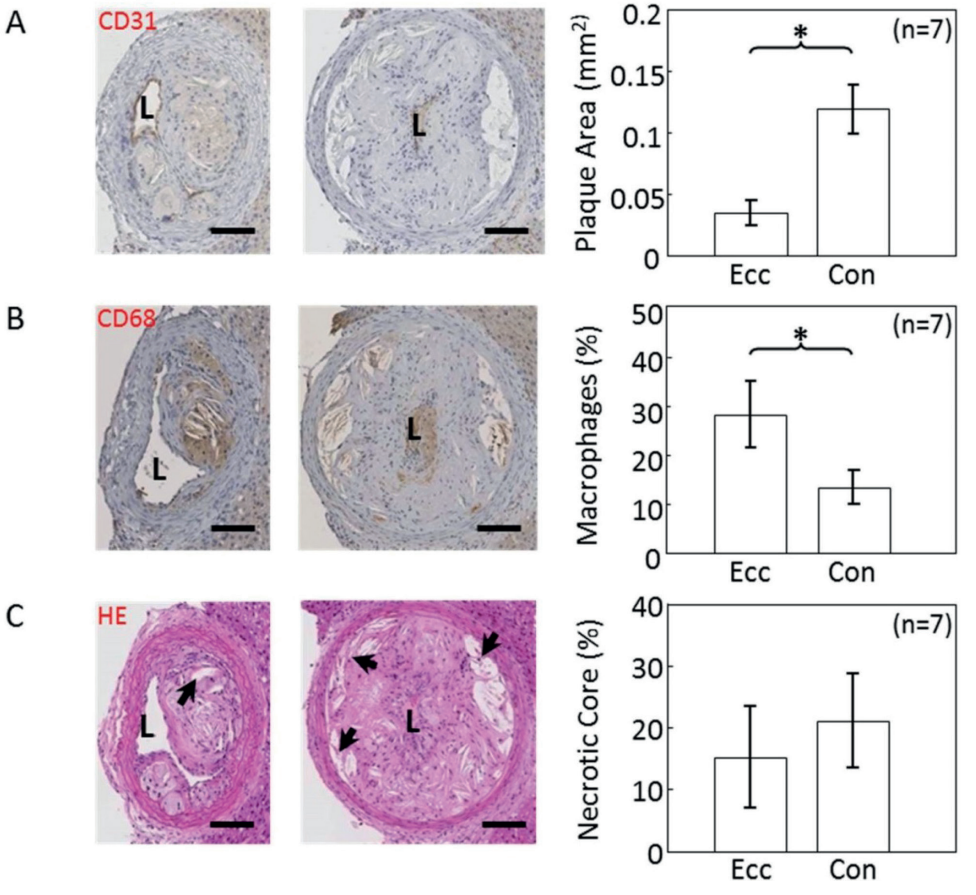

Figure 6: Characterization of plaque composition. *Representative histological staining of the eccentric and concentric segment of representative mouse 1 and quantification of all mice is shown. (A) Plaque area (mm2) was delineated by CD31 endothelial staining; (B) Relative macrophage area (%) was determined using CD68 staining; (C) relative necrotic core area (%) was delineated by H&E nuclei staining (Arrows: necrotic cores); Plaque area was significantly larger in the concentric segment, while macrophage area was larger in the eccentric segment (Student's t-test, n = 7, *p<0.05). Bar is 100 µm.*

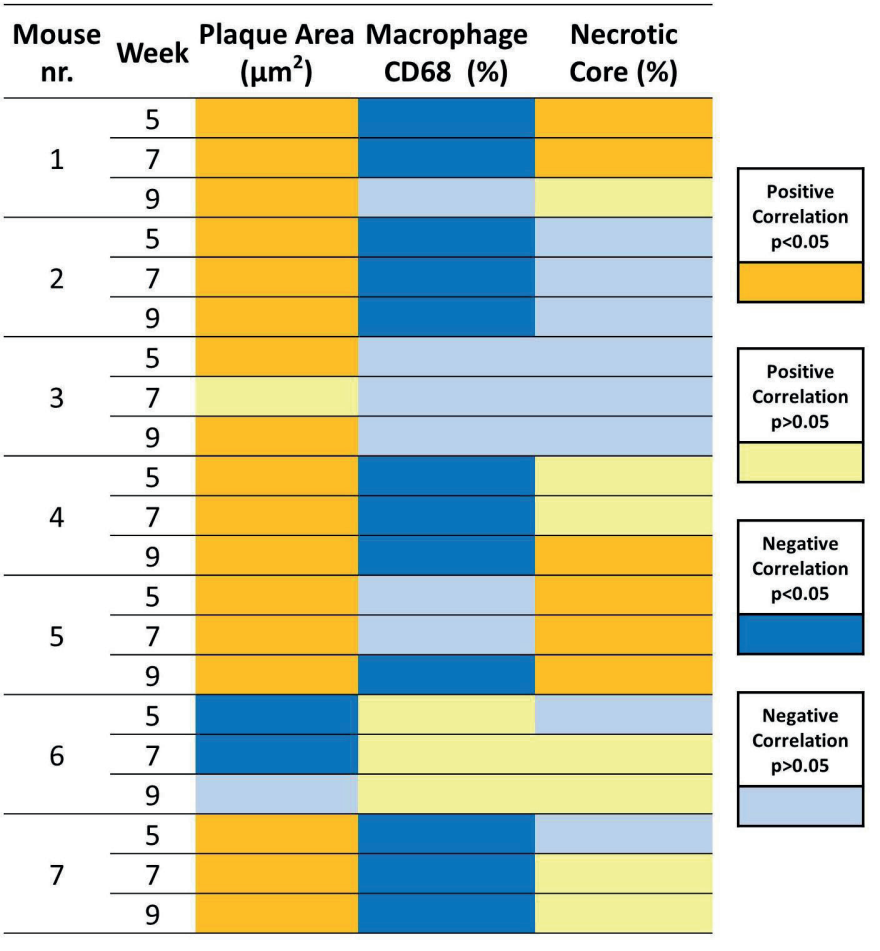

Figure 7: Correlation between WSS at all time points and plaque composition. *Yellow: positive correlation, p<0.05; Blue: positive correlation, p>0.05; Light Yellow: negative correlation, p<0.05; Light Blue: negative correlation, p>0.05.*

Discussion

Our study described the temporal and spatial changes in vessel geometry, blood flow and concomitant WSS over an advanced murine plaque and its correlation to plaque area and macrophage content. First, we demonstrated that it was possible to follow changes in lumen area over time using contrast-enhanced micro-CT. Lumen narrowing was observed in all animals upstream to the cast, implying the formation of a lumen intruding plaque. The minimum degree of stenosis varied among animals at each time point, leading to different progression profiles over time. These differences in disease progression rate were not related to the initial degree of stenosis at week 5 or plaque size observed at week 9. Immediately after cast placement, flow reduction of 23.3±19.8% was observed in the RCCA, comparable with previously reported values [33,37]. During plaque progression, as stenotic degree increased over time, blood flow in the RCCA decreased gradually from week 5 to 9. Flow decrease was also observed in animals with constant degree of stenosis over time. Therefore, the observed flow decrease was not only due to the increasing stenotic degree of the lumen intruding plaque, but also likely to be due to increasing resistance of the distal vascular bed beyond the carotid bifurcation. In general, blood flow decreased during plaque progression in all mice, except one. Our results strongly suggested that there were temporal and animal-specific variations in vessel geometry and blood flow and therefore one should not use generic values when computing WSS distribution as suggested previously [53].

Variations in the local geometrical and blood flow data at the time of investigation lead to a complex spatial and temporal distribution of WSS in vivo among animals. As blood flow reduced and vessel diameter remained constant, RCCA was exposed to dramatically decreasing levels of **absolute** WSS over time. However, over all, WSS decreased over time and was minimal at week 9 in all animals but one. Generally it is believed that WSS over a lumen intruding plaque would increase over time due to the increased degree of stenosis. Our findings showed that this is not the case in this animal model, contrary to the general consensus [54]. Nevertheless, if we look at the spatial distribution of WSS in the upstream RCCA, **relative** WSS showed a gradual increase from the healthy segment to the eccentric and then concentric plaque segment, which is in line with the general consensus. Although relative WSS distribution followed the expected spatial pattern, one should keep in mind that it was on a background with dramatically decreased absolute WSS levels. This implies that previous studies which correlated high WSS to plaque pathogenesis using this mouse model should potentially be reinterpreted. This underlines again the importance of computing WSS on subject-specific flow and geometries.

To analyze correlations between WSS and plaque components, we analyzed plaque composition after the final imaging moment. To visualize the spatial heterogeneity of plaque composition, we performed consistent sampling of the plaque, similar to the study reported before [55]. This analysis revealed the presence of one continuous plaque. Its composition varied in the axial direction (Fig. 8). In all animals, proximally, the plaque was small and eccentric, and abundant in macrophages. The macrophage concentration was comparable to that reported by Cheng et al [33]. We observed that the plaque segment located closer to the cast was big and concentric. CT data demonstrated that vessel lumen narrowing was first observed close to the upstream part of the cast, suggesting that the plaque revealed here was present for a longer time and thus its composition was more advanced, while the proximal part of the plaque is "younger" and less advanced. The spatial heterogeneity of the plaque implied that sampling location should be taken into account when analyzing plaque composition in any animal model for atherosclerosis or human atherosclerotic sample[15]. Results might be different if one only selects histological sections from either eccentric or concentric diseased segments.

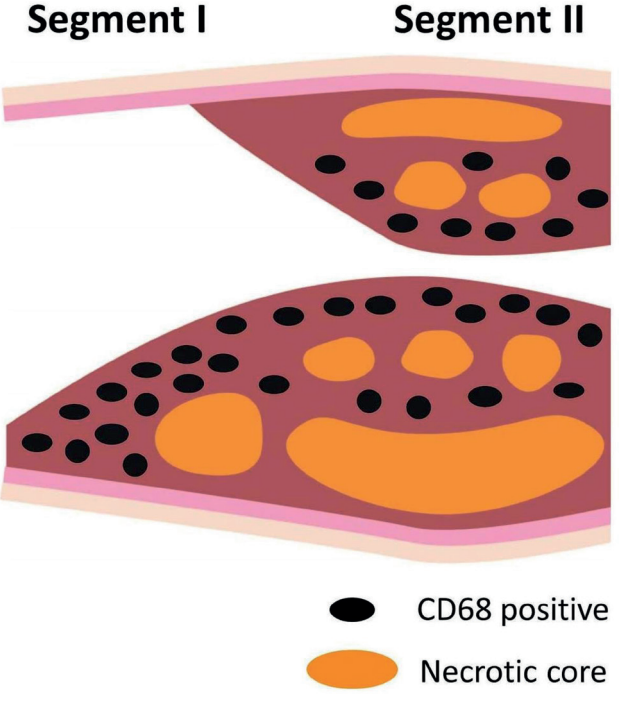

Figure 8: Schematic overview plaque morphology. *Proximally, the plaque was smaller and eccentric with abundant accumulation of macrophages. Closer to the cast, the plaque was larger and concentric.*

Using mouse-specific absolute WSS at a given time point and using the histological data, we demonstrated a strong inverse relationship between macrophages and WSS. Macrophages accumulated in the proximal eccentric plaques where WSS was lowest, confirming the pro-inflammatory effect of low WSS reported before [1,14,56]. In this mouse model, the continuous exposure to reducing levels of WSS in the proximal eccentric plaque correlated to inflammation and thus plaque growth. However, regardless of the homogeneous distribution of WSS in the upstream RCCA, the proximal segment of the plaque had an eccentric composition. In addition, although the upstream part of the RCCA was homogeneously exposed to extremely low WSS, plaque was only present close to the cast. These evidences suggested that low WSS alone is not incentive enough to induce plaque initiation. We think that the plaque initially grew from the region close to the cast, and there might be factors (damage from the cast surgery, distribution of inflammatory cells or layout of fibrotic tissues) from the existing plaque that induced a non-homogeneous growth pattern in the proximal direction. In addition, we showed that 6 out of 7 mice had a positive and significant correlation between WSS and plaque area. The one animal that showed contrasting correlations (mouse number 6 in Fig. 7) presented with such extensive plaque progression that the stenosis created by the plaque was more severe than the stenosis induced by cast placement (Suppl. Fig. 1).
In our study, we observed large variations in both WSS distribution and plaque composition among animals. Correlation between WSS distribution and plaque composition reduced when data were pooled. This implies that one can miss out on important correlations if the often-applied approach of pooling WSS and histological data is used. Similarly, De Wilde [7] showed that pooling data lead to misinterpretation of correlation between WSS metrics and plaque composition. Therefore, when analyzing functional parameters from one to another, using subject-specific WSS and histological data is necessary.

Study Limitations

A limitation of this study was that we were not able to perform rotational matching between the 3D WSS maps to the lumen surface obtained from histology. Subdividing the 3D WSS maps into cross-sections and matching it to the corresponding orientation of the histological sections would potentially increase information density. In our study, the upstream RCCA was relatively a straight segment where WSS distributed homogeneously along the lumen circumference. We thus expected little effect of performing rotational matching. In addition, we focused on computing WSS and did not compute wall stress which is expected to play a role, especially close to the cast [42], which is why we did not include the sections close to the cast in our histological analysis. A limitation of

our model is that mice do not present with vulnerable plaques in accordance with the definition of a human vulnerable plaque and that is mouse plaques are not rupture-prone [42]. The differences between mice –and animal models in general- and humans were reviewed by us and others [42,57,58]. The implication of these differences is that translation of the findings based on these animal data to patient studies should therefore be done cautiously. A relevant example of the difference between mice and humans pertains to cap thickness, a strong indicator of plaque vulnerability in human plaques, which is ill-defined in mice due to the presence of multiple necrotic cores, located deep in the plaque. We therefore decided not to put forward cap thickness analyses in this manuscript.

Conclusion

We quantified the temporal and spatial evolution of WSS in an atherosclerotic mouse model and we studied the correlation between the animal-specific WSS data and plaque composition in the same animal. Strikingly, due to the temporal changes in geometry and flow, WSS decreased over time during disease progression, contrary to the general belief. In the majority of the mice, lower WSS was associated with elevated levels of inflammation, which mainly localized proximally where the plaque was small and eccentric. Closer to the cast where a larger concentric plaque was observed, higher WSS was associated with increased plaque area. In addition, our study clearly demonstrated the necessity to analyze individual animals and plaques when studying correlations between WSS and plaque composition.

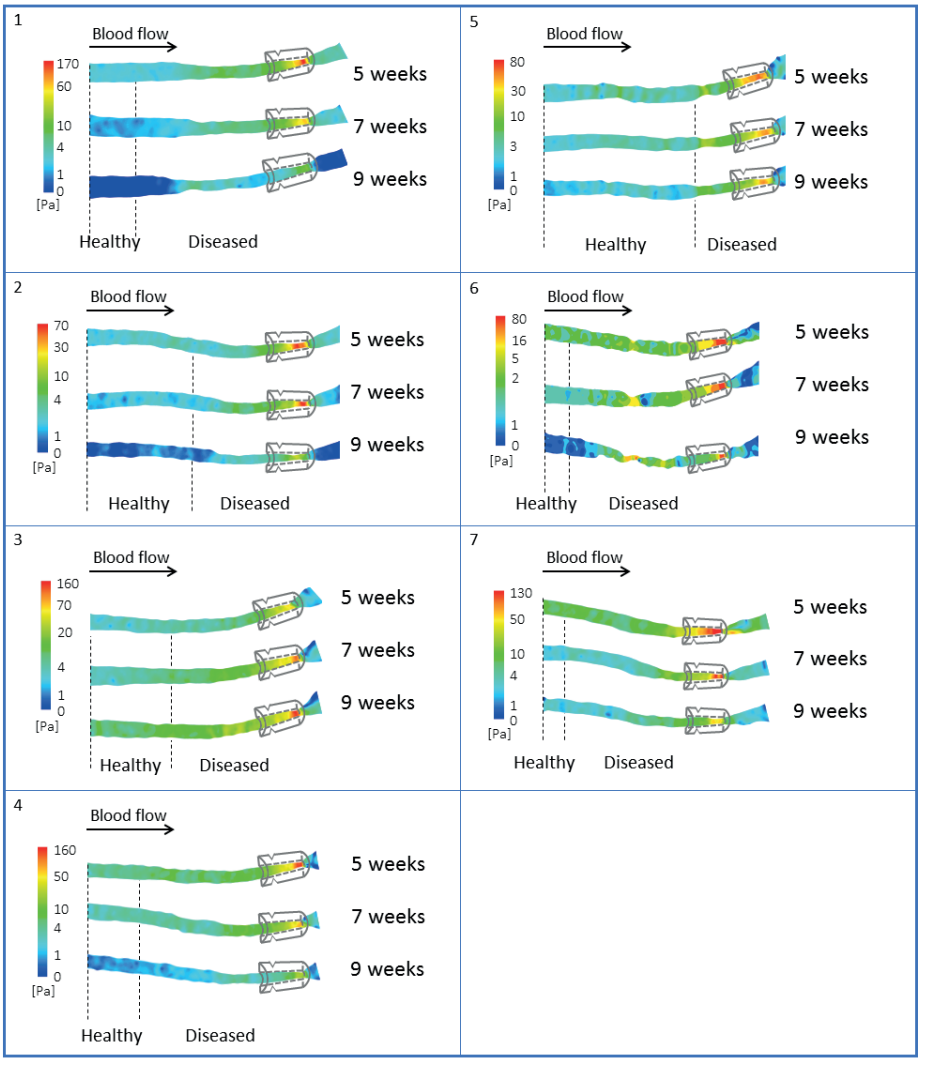

Supplemental Figure 1: *WSS distribution in all mice. 3D WSS distribution in the RCCAs at 5, 7 and 9 weeks after cast placement. Circumferentially-averaged WSS along the RCCA is shown. Each color bar shows animal-specific absolute WSS levels.*

References

1. Malek, A. M., Alper, S. L. & Izumo, S. Hemodynamic shear stress and its role in atherosclerosis. ***Jama* 282**, 2035–2042 (1999).
2. Chiu, J.-J., Usami, S. & Chien, S. Vascular endothelial responses to altered shear stress: Pathologic implications for atherosclerosis. ***Ann. Med.* 41**, 19–28 (2009).
3. Evans, P. C. & Kwak, B. R. Biomechanical factors in cardiovascular disease. ***Cardiovasc. Res.* 99**, 229–231 (2013).
4. Slager, C. J. ***et al.*** The role of shear stress in the generation of rupture-prone vulnerable plaques. ***Nat Clin Pr. Cardiovasc Med* 2**, 401–407 (2005).
5. Slager, C. J. ***et al.*** The role of shear stress in the destabilization of vulnerable plaques and related therapeutic implications. ***Nat Clin Pr. Cardiovasc Med* 2**, 456–464 (2005).
6. Koskinas, K. C. ***et al.*** Natural history of experimental coronary atherosclerosis and vascular remodeling in relation to endothelial shear stress: A serial, in vivo intravascular ultrasound study. ***Circulation* 121**, 2092–2101 (2010).
7. De Wilde, D., Trachet, B., De Meyer, G. R. Y. & Segers, P. Shear Stress Metrics and Their Relation to Atherosclerosis: An In Vivo Follow-up Study in Atherosclerotic Mice. ***Ann. Biomed. Eng.* 44**, 2327–2338 (2016).
8. Virmani, R., Burke, A. P., Kolodgie, F. D. & Farb, A. Vulnerable plaque: the pathology of unstable coronary lesions. ***J. Interv. Cardiol.* 15**, 439–46 (2002).
9. Stary, H. C. ***et al.*** A definition of advanced types of atherosclerotic lesions and a histological classification of atherosclerosis. A report from the Committee on Vascular Lesions of the Council on Arteriosclerosis, American Heart Association. ***Circulation* 92**, 1355–1374 (1995).
10. Fujii, K. ***et al.*** Intravascular Ultrasound Assessment of Ulcerated Ruptured Plaques. ***Circulation* 108**, (2003).
11. de Weert, T. T. ***et al.*** Atherosclerotic plaque surface morphology in the carotid bifurcation assessed with multidetector computed tomography angiography. ***Stroke* 40**, 1334–1340 (2009).
12. Cicha, I. ***et al.*** Carotid plaque vulnerability: a positive feedback between hemodynamic and biochemical mechanisms. ***Stroke* 42**, 3502–3510 (2011).
13. Daemen, M. J. ***et al.*** Carotid plaque fissure: An underestimated source of intraplaque hemorrhage. ***Atherosclerosis* 254**, 102–108 (2016).
14. Dirksen, M. T., van der Wal, A. C., van den Berg, F. M., van der Loos, C. M. & Becker, A. E. Distribution of inflammatory cells in atherosclerotic plaques relates to the direction of flow. ***Circulation* 98**, 2000–2003 (1998).
15. Fagerberg, B. ***et al.*** Differences in Lesion Severity and Cellular Composition between in vivo Assessed Upstream and Downstream Sides of Human Symptomatic Carotid Atherosclerotic Plaques. ***J. Vasc. Res.* 47**, 221–230 (2010).
16. Nakazawa, G. ***et al.*** Pathological Findings at Bifurcation Lesions: The Impact of Flow Distribution on Atherosclerosis and Arterial Healing After Stent Implantation. ***J. Am. Coll. Cardiol.* 55**, 1679–1687 (2010).
17. Samady, H. ***et al.*** Coronary artery wall shear stress is associated with progression and transformation of atherosclerotic plaque and arterial remodeling in patients with coronary artery disease. ***Circulation* 124**, 779–788 (2011).
18. Groen, H. C. ***et al.*** Plaque rupture in the carotid artery is localized at the high shear stress region: a case report. ***Stroke* 38**, 2379–2381 (2007).
19. Fukumoto, Y. ***et al.*** Localized Elevation of Shear Stress Is Related to Coronary Plaque Rupture. A 3-Dimensional Intravascular Ultrasound Study With In-Vivo Color Mapping of Shear Stress Distribution. ***J. Am. Coll. Cardiol.* 51**, 645–650 (2008).
20. Yang, C. ***et al.*** Advanced human carotid plaque progression correlates positively with flow shear stress using follow-up scan data: an in vivo MRI multi-patient 3D FSI study. ***J Biomech* 43**, 2530–2538 (2010).
21. Gijsen, F., van der Giessen, A., van der Steen, A. & Wentzel, J. Shear stress and advanced atherosclerosis in human coronary arteries. ***J Biomech* 46**, 240–247 (2013).
22. Stone, P. H. ***et al.*** Effect of endothelial shear stress on the progression of coronary artery disease, vascular remodeling, and in-stent restenosis in humans: in vivo 6-month follow-up study. ***Circulation* 108**, 438–444 (2003).
23. Chatzizisis, Y. S. ***et al.*** Prediction of the localization of high-risk coronary atherosclerotic plaques on the basis of low endothelial shear stress: an intravascular ultrasound and histopathology natural history study.

Circulation **117**, 993–1002 (2008).
24. Wentzel, J. J. ***et al.*** Endothelial shear stress in the evolution of coronary atherosclerotic plaque and vascular remodelling: current understanding and remaining questions. doi:10.1093/cvr/cvs217.
25. Eshtehardi, P. ***et al.*** Association of coronary wall shear stress with atherosclerotic plaque burden, composition, and distribution in patients with coronary artery disease. *J Am Hear. Assoc* **1**, e002543 (2012).
26. Koskinas, K. C. ***et al.*** Thin-capped atheromata with reduced collagen content in pigs develop in coronary arterial regions exposed to persistently low endothelial shear stress. ***Arter. Thromb Vasc Biol*** **33**, 1494–1504 (2013).
27. Vergallo, R. ***et al.*** Endothelial shear stress and coronary plaque characteristics in humans: combined frequency-domain optical coherence tomography and computational fluid dynamics study. ***Circ Cardiovasc Imaging*** **7**, 905–911 (2014).
28. Papafaklis, M. I. ***et al.*** Effect of the local hemodynamic environment on the de novo development and progression of eccentric coronary atherosclerosis in humans: insights from PREDICTION. ***Atherosclerosis*** **240**, 205–211 (2015).
29. Han, D. ***et al.*** Relationship Between Endothelial Wall Shear Stress and High-Risk Atherosclerotic Plaque Characteristics for Identification of Coronary Lesions That Cause Ischemia: A Direct Comparison With Fractional Flow Reserve. ***J. Am. Heart Assoc.*** **5**, e004186 (2016).
30. Timmins, L. H. ***et al.*** Oscillatory wall shear stress is a dominant flow characteristic affecting lesion progression patterns and plaque vulnerability in patients with coronary artery disease. ***J R Soc Interface*** **14**, (2017).
31. Kumar, A. & Lindner, V. Remodeling With Neointima Formation in the Mouse Carotid Artery After Cessation of Blood Flow. ***Arterioscler. Thromb. Vasc. Biol.*** **17**, 2238–2244 (1997).
32. Castier, Y., Brandes, R. P., Leseche, G., Tedgui, A. & Lehoux, S. p47phox-dependent NADPH oxidase regulates flow-induced vascular remodeling. ***Circ. Res.*** **97**, 533–40 (2005).
33. Cheng, C. ***et al.*** Atherosclerotic lesion size and vulnerability are determined by patterns of fluid shear stress. ***Circulation*** **113**, 2744–53 (2006).
34. Nam, D. ***et al.*** Partial carotid ligation is a model of acutely induced disturbed flow , leading to rapid endothelial dysfunction and atherosclerosis. 1535–1543 (2009) doi:10.1152/ajpheart.00510.2009.
35. Thim, T. ***et al.*** Wall shear stress and local plaque development in stenosed carotid arteries of hypercholesterolemic minipigs. ***J Cardiovasc Dis Res*** **3**, 76–83 (2012).
36. Chen, Y.-C. ***et al.*** A novel mouse model of atherosclerotic plaque instability for drug testing and mechanistic/therapeutic discoveries using gene and microRNA expression profiling. ***Circ. Res.*** **113**, 252–265 (2013).
37. Pedrigi, R. M. ***et al.*** Influence of shear stress magnitude and direction on atherosclerotic plaque composition. ***R Soc Open Sci*** **3**, 160588 (2016).
38. Winkel, L. C., Hoogendoorn, A., Xing, R., Wentzel, J. J. & Van der Heiden, K. Animal models of surgically manipulated flow velocities to study shear stress-induced atherosclerosis. ***Atherosclerosis*** vol. 241 100–110 (2015).
39. Cheng, C. ***et al.*** The role of shear stress in atherosclerosis: action through gene expression and inflammation? ***Cell Biochem. Biophys.*** **41**, 279–94 (2004).
40. Xing, R. ***et al.*** Contrast-enhanced micro-CT imaging in murine carotid arteries: a new protocol for computing wall shear stress. ***Biomed. Eng. Online*** **15**, 621–633 (2016).
41. Winkel, L. C. J. ***et al.*** Folate receptor–targeted single-photon emission computed tomography/computed tomography to detect activated macrophages in atherosclerosis: can it distinguish vulnerable from stable atherosclerotic plaques? ***Mol. Imaging*** **13**, (2014).
42. van der Heiden, K., Hoogendoorn, A., Daemen, M. J. & Gijsen, F. J. H. Animal models for plaque rupture: a biomechanical assessment. ***Thromb. Haemost.*** **115**, 501–508 (2015).
43. Davies, P. F. Hemodynamic shear stress and the endothelium in cardiovascular pathophysiology. ***Nat. Clin. Pract. Cardiovasc. Med.*** **6**, 16–26 (2009).
44. Schrauwen, J. T. C. ***et al.*** Influence of the Accuracy of Angiography-Based Reconstructions on Velocity and Wall Shear Stress Computations in Coronary Bifurcations: A Phantom Study. ***PLoS One*** **10**, e0145114 (2015).
45. Peiffer, V., Sherwin, S. J. & Weinberg, P. D. SPOTLIGHT REVIEW Does low and oscillatory wall shear stress correlate spatially with early atherosclerosis? A systematic review. doi:10.1093/cvr/cvt044.
46. Mohamied, Y. ***et al.*** Change of direction in the biomechanics of atherosclerosis. ***Ann. Biomed. Eng.*** **43**, 16–25 (2015).
47. De Wilde, D. ***et al.*** Assessment of shear stress related parameters in the carotid bifurcation using mouse-specific FSI simulations. ***J. Biomech.*** (2015) doi:10.1016/j.jbiomech.2015.11.048.
48. Gijsen, F. J. H., Allanic, E., van de Vosse, F. N. & Janssen, J. D. The influence of the non-Newtonian properties of blood on the flow in large arteries: unsteady flow in a 90° curved tube. ***J. Biomech.*** **32**, 705–713

(1999).
49. Trachet, B. ***et al.*** An Integrated Framework to Quantitatively Link Mouse-Specific Hemodynamics to Aneurysm Formation in Angiotensin II-infused ApoE −/− mice. ***Ann. Biomed. Eng.*** **39**, 2430–2444 (2011).
50. Gage, G. J., Kipke, D. R. & Shain, W. Whole animal perfusion fixation for rodents. ***J. Vis. Exp.*** (2012) doi:10.3791/3564.
51. Seimon, T. A. ***et al.*** Macrophage deficiency of p38alpha MAPK promotes apoptosis and plaque necrosis in advanced atherosclerotic lesions in mice. ***J. Clin. Invest.*** **119**, 886–98 (2009).
52. Schürmann, C., Gremse, F., Jo, H., Kiessling, F. & Brandes, R. P. Micro-CT Technique Is Well Suited for Documentation of Remodeling Processes in Murine Carotid Arteries. ***PLoS One*** **10**, e0130374 (2015).
53. Van Doormaal, M., Zhou, Y.-Q., Zhang, X., Steinman, D. A. & Mark Henkelman, R. Inputs for subject-specific computational fluid dynamics simulation of blood flow in the mouse aorta. ***J. Biomech. Eng.*** **136**, 101008 (2014).
54. Wang, Y. ***et al.*** High shear stress induces atherosclerotic vulnerable plaque formation through angiogenesis. ***Regen. Biomater.*** **3**, 257–67 (2016).
55. Pedrigi, R. M. ***et al.*** Thin-Cap Fibroatheroma Rupture Is Associated With a Fine Interplay of Shear and Wall Stress. ***Arterioscler. Thromb. Vasc. Biol.*** **34**, 2224–2231 (2014).
56. VanderLaan, P. A., Reardon, C. A. & Getz, G. S. Site specificity of atherosclerosis: site-selective responses to atherosclerotic modulators. ***Arterioscler. Thromb. Vasc. Biol.*** **24**, 12–22 (2004).
57. Pedrigi, R. M. ***et al.*** Inducing Persistent Flow Disturbances Accelerates Atherogenesis and Promotes Thin Cap Fibroatheroma Development in D374Y-PCSK9 Hypercholesterolemic Minipigs. ***Circulation*** **132**, 1003–1012 (2015).
58. Getz, G. S. & Reardon, C. A. Animal models of atherosclerosis. ***Arterioscler. Thromb. Vasc. Biol.*** **32**, 1104–15 (2012).

Chapter 5 Data processing pipeline for lipid profiling of carotid atherosclerotic plaque with mass spectrometry imaging

Mirjam Visscher*, Astrid M. Moerman*, Peter C. Burgers, Heleen M.M. van Beusekom, Theo M. Luider, Hence J.M. Verhagen, Antonius F.W. van der Steen, Kim van der Heiden#, Gijs van Soest#
**# These authors contributed equally*

Based on: Data processing pipeline for lipid profiling of carotid atherosclerotic plaque with mass spectrometry imaging, J. Am. Soc. Mass Spectrom, 2019

Abstract

Atherosclerosis is a lipid and inflammation-driven disease of the arteries that is characterized by gradual buildup of plaques in the vascular wall. A so-called 'vulnerable plaque', consisting of a lipid-rich necrotic core contained by a thin fibrous cap, may rupture and trigger thrombus formation, which can lead to ischemia in the heart (heart attack) or in the brain (stroke). In this study, we present a protocol to investigate the lipid composition of advanced human carotid plaques using matrix-assisted laser desorption ionization (MALDI) mass spectrometry imaging (MSI), providing a framework that should enable the discrimination of vulnerable from stable plaques based on lipid composition. We optimized the tissue preparation and imaging methods by systematically analyzing data from three specimens: two human carotid endarterectomy samples (advanced plaque) and one autopsy sample (early stage plaque). We show a robust data reduction method and evaluate the variability of the endarterectomy samples. We found diacylglycerols to be more abundant in a thrombotic area compared to other plaque areas and could distinguish advanced plaque from early stage plaque based on cholesteryl ester composition. We plan to use this systematic approach to analyze a larger dataset of carotid atherosclerotic plaques.

Introduction

Atherosclerosis is the cause of more than 10 million deaths worldwide, and a major contributor to long-term morbidity and disability [1]. This disease of the artery walls is characterized by the gradual formation of depositions in the vascular wall that are called atherosclerotic plaques. Plaque growth is initiated by endothelial dysfunction and driven by impaired lipid transport mechanisms, which trigger an inflammatory response. Lipids thus play a key role in the pathogenesis of atherosclerosis. Besides a variety of lipid species, these plaques contain calcifications, fibrous tissue, smooth muscle cells and necrotic material [2,3]. Depending on the tissue composition and structure of the plaque, plaques can be either 'stable' or 'vulnerable', the latter means they are prone to rupture. Plaque rupture may trigger embolization of fragments of plaque tissue in the bloodstream, which, depending on the anatomical location of the plaque, can lead to stroke or myocardial infarction [4,5]. The mechanisms driving the evolution of a stable plaque to a vulnerable phenotype are not known in detail, although it is clear that defective or unbalanced lipid transport plays a key role [6-10]. The recent LRP study (presented at TCT2018 [11]) demonstrated that coronary vessel segments with lipid-rich plaque have a >4 times higher clinical event rate than vessel segments without such plaque, highlighting the impor-

tance of plaque lipid content for triggering ischemia. We aim to study whether the lipid profile differs between stable and vulnerable plaque types. To determine whether a plaque's lipid profile can be correlated to plaque phenotype and, therefore, risk of rupture, variation between and within plaque samples needs to be assessed. In this study we present a mass spectrometry imaging (MSI) method for systematically studying plaque lipid distribution at various stages of development. MSI is an emerging experimental technique in the molecular characterization of biological samples. Using MSI, the molecular composition of thin tissue sections can be imaged at a micron-scale resolution. As an initial step, MSI requires ionization of the tissue section. Different methods of ionization exist, including matrix-assisted laser desorption ionization (MALDI), a commonly used ionization method for biological samples [12]. The main advantages of MALDI are its ability to generate singly charged ions, which greatly simplifies analysis of mass spectra, and its ability of so-called 'soft' ionization, preventing molecules from fragmenting during the ionization process [12]. MALDI-MSI is suitable for the detection of small molecules, such as lipids.

To date, few studies of (MALDI-)MSI on human arteries have been published [13-19].They explored the parameter space of atherosclerotic plaque composition as sampled by MSI along various dimensions. Prior work examined different arterial beds, i.e. aorta [17], carotid [15,16,18], coronary arteries [14], femoral or popliteal [13,19], and in the ionization method used, i.e. MALDI [13,17-19], secondary ion mass spectrometry (SIMS) [14,15] or desorption electrospray ionization (DESI) [16]. Clinically relevant plaques, those that are likely to precipitate ischemic events, contain a variable mix of lipids [7]. In studying the role of various lipids [8,20] in the atherosclerotic disease process, it is therefore important to optimize the analysis for accurately sampling the lipid spectrum, and to quantitatively understand the variance in measured ion abundances. We consequently chose to focus on lipid-rich plaques only, and moreover restricted ourselves to carotid plaques, as these are a major precursor of ischemic stroke [21].

Our aim is to develop a MALDI-MSI pipeline for the analysis of lipids in human carotid artery plaques, suitable for assessing the variation in lipid profile, both between different plaque specimens and within different locations in the same specimen. To that aim, we add the following insights to the existing MSI knowledge: (1) We describe how arterial tissue should be processed, such that the combination of MALDI-MSI and histological information enables contextualization of MSI data in terms of the known morphological features of plaque pathology. (2) We combine various MSI data analysis methods into a robust data processing pipeline that reliably reduces an MSI dataset into manageable lipid-specific results. We describe this pipeline in detail to encourage other researchers to follow similar pipelines in their own research. (3) We assess the reproducibility of measurements by calculating the coefficient of variation of MALDI-MSI measurement results of tissue sections that were located close

together.
In addition, we discuss tentative observations in three human carotid plaques that illustrate the potential for imaging lipid biochemistry in atherosclerosis. This method is readily applicable to larger collections, limited by scan time, of carotid plaque specimens, allowing to assess the relation between the carotid plaque's molecular lipid composition and plaque type using statistical methods.

Methods

Materials

DPBS (without Calcium and Magnesium), KP Haematoxyline mayer (VWRK4085-9002), Resorcin (1075930100), SuperFrostPlus glass slides (76 × 26mm) were purchased from VWR (The Netherlands). Eosine (HT110232-1L), Oil Red O (00625-25G), Basic Fuchsin (857343-25G), Ferric(III) Chloride (157740-100G), 2,5-dihydroxybenzoic acid (98%, 149357-100G) and porcine type A gelatin were purchased from Sigma-Aldrich (The Netherlands). HPLC grade acetone was purchased from Fisher Scientific (The Netherlands). Mouse anti-human CD31 (JC/70A, ab9498) and, mouse anti-human CD68 (KP1, ab955) were purchased from Abcam (United Kingdom). EnVision+Kit (HRP, mouse, 1100 tests, 110 ml, K4001) was purchased from Agilent (the Netherlands). Lipid standards Cholest-5-en-3ß-yl heptadecanoate (CE 17:0) 1mg/mL (700186M-1mg) and 1,2-diheptadecanoyl-sn-glycero-3-phosphocholine (PC 17:0) 10 mg/mL (850360C-25mg) were purchased from Avanti Polar Lipids (USA).

Tissue collection

Carotid endarterectomy (CEA) surgery was performed by carefully opening the outer wall of the carotid artery and excising the plaque by separating the intima and media. This protocol preserves an intact lumen and plaque morphology [22] . Two human carotid plaque specimens, harvested at carotid endarterectomy (CEA) surgery, were rinsed in phosphate-buffered saline (DPBS), snap frozen and stored at -80°C until further processing. A third carotid artery specimen, without apparent atherosclerotic disease, was collected at autopsy within 24 hours postmortem, from a subject with a non-cardiovascular cause of death. This specimen was rinsed in DPBS and stored in the same manner. Tissue collection was performed according to protocols sanctioned by the Ethics Board at Erasmus MC (MEC 2008-147 for carotid endarterectomy samples, MEC 2017-300 for the autopsy sample).

Sample preparation

One CEA specimen, referred to as P1, was transversally divided into 1 mm segments to study intraplaque variability. We hypothesize that the plaque's molecular lipid composition may change along the length of the vessel. Five 1 mm segments, originating ≈3mm apart, evenly spaced along the axial length of the CEA sample, were used for imaging. Three of the segments were located caudal to the carotid bifurcation and two segments originated from the internal carotid artery, see Fig. 1. The second CEA specimen, referred to as P2, and the autopsy specimen, referred to as A, were imaged in a single axial location. The imaged 1 mm segment of P2 was located cranial to the bifurcation, in the internal carotid artery, where atherosclerotic disease stage is generally maximal. The imaged 1 mm segment of A originated from the common carotid artery, where no or minimal plaque formation is expected.

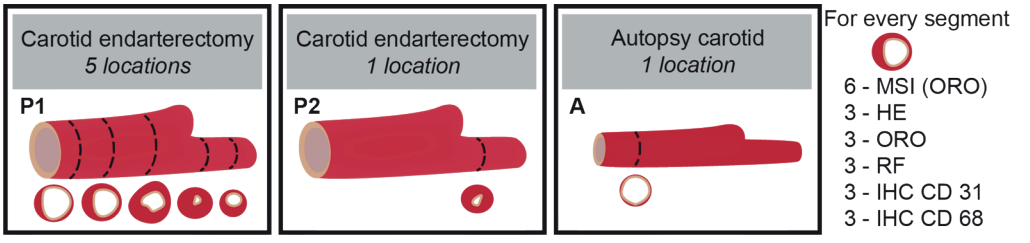

Figure 1: Overview of tissue samples. *Five segments from carotid endarterectomy specimen 1 (P1), one segment from carotid endarterectomy specimen 2 (P2) and, one segment from the autopsy carotid (A). Number of MALDI-MSI measurements and adjacent histological stains*

All 1 mm segments were embedded in 10% porcine type A gelatin and cryo-sectioned (CM3050 S, Leica Biosystems (cutting temps: OT -21°C; CT -19°C)), into 10µm sections which were then thaw mounted onto non-conductive glass slides. After sectioning, the slides were stored at -80°C until imaging or histological staining. Per segment, 6 sections were imaged; the distance between MALDI-MSI sections was 30-50 µm. All sections were imaged or stained within 2 months after sectioning.
Prior to imaging, the slides were desiccated under vacuum at room temperature for 10 minutes. The matrix, 2,5-dihydroxybenzoic acid (DHB), was applied using sublimation (home-built sublimation system as described in Dekker et al.[23]) at 125°C for 10 minutes; 50 mg of DHB was dissolved in 5 ml acetone. No washing, re-crystallization, or addition of ionization agents was used.

Histological staining

Histological staining was performed on adjacent slides, which were histochemically stained by Hematoxylin-Eosin (HE), Oil Red O (ORO) and Resorcin-Fuchsin (RF) staining, to visualize general structure, lipids, and collagen and elastin, respectively. Immunohistochemical (IHC) staining was performed to visualize endothelial cells and macrophages. The slides imaged with MALDI-MSI were stained by ORO after MSI.
We assessed the plaque tissue according to the plaque classification scheme of Virmani et al. [2,3] and examined the tissue for features of plaque vulnerability (i.e. necrotic core, calcification, thrombus). We also assessed the tissue's structural variability over consecutive tissue sections that originate from the same 1mm segment. We used the histopathological data as a guidance to interpret the MALDI-MSI data.

Data acquisition

MALDI-MSI was performed on a MALDI-q-TOF mass spectrometer (Waters Synapt G2Si-TOF, Manchester, UK), operated in positive mode, at the instrument's "resolution mode" (single-pass reflectron TOF) with a spatial resolution of 50 µm. An Nd:YAG (355 nm) laser was operated at 2,000 Hz, at 50% of the maximum laser energy available (250/500 laser energy). At this energy level, the laser spot was ≈40µm in size. The mass range was 300-1,200 *m/z* and the scan time per pixel was 0.5 seconds using a left-right scanning pattern. The data was acquired using MassLynx v4.1 software (Waters, Manchester, UK) and HDimaging v1.4 software was used to export the data to imzML format. Prior to imaging, the machine was calibrated with red phosphorus spotted onto a steel plate.

Mass identification

For the identification of the various lipid components, lipids were extracted [24] by homogenizing 5 mg of tissue in 250 µL of Milli-Q water. The tissue was taken between sections P1-4 and P1-5. 10µL homogenized sample was combined with 10µl 10% TEA solution (trimethylamine (10/90, v/v) in methanol/dichloromethane (DCM) (50/50, v/v)) and mixed thoroughly. Subsequently, 450µl methanol/DCM (50/50, v/v) was added to this mixture. Samples were incubated on the roller bank for 30 minutes at 4°C. After incubation, samples were centrifuged at 14,000 rpm for 20 minutes at 4°C. Supernatant was transferred to a glass vial, and freeze dried until further use.
The extract was subjected to high resolution MS for accurate mass data and

MS/MS experiments for structural information, as described in Angel et. al (2016)[25]. Ten µL of the extract was mixed with 190µL of a methanol/chloroform (1/1, v/v) mixture and infused at a rate of 240µL/hr. In a second set of experiments, ammonium acetate was added to efficiently detect the cholesteryl esters (CE), a 10µL of the extract was mixed with 180µL of a methanol/chloroform (1/1, v/v) and 10µL of a 10mM ammonium acetate solution was added; the cholesteryl esters appear as NH_4^+ adducts [26].
High resolution mass data were obtained with an LTQ Orbitrap XL mass spectrometer with an electrospray ion source operated in the positive ion mode using the following settings: source voltage 4~kV and capillary temperature 300°C. In such experiments, the analyte molecules appear as $[M+H]^+$ or as $[M+NH_4]^+$ species, whereas in MALDI imaging experiments they are usually cationized by residual Na^+ and/or K^+. Peaks within 2 ppm of the expected *m/z* values were taken into consideration for identification by MS/MS experiments. For lipids such as the phosphatidylcholines (PC) and sphingomyelins (SM), product ions in MS/MS spectra (for example *m/z* 184.1) may lie below the cut-off mass of the ion trap (27% of precursor mass). To circumvent such discrimination effects and to reliably identify such species, MS/MS spectra were recorded on a triple quadrupole mass spectrometer, in our case an AB Sciex API-3000 mass spectrometer operated in the positive ion mode, using the following settings: source temperature 200°C, capillary voltage 5.5kV and collision energy 20V.
Many of the ionized lipids undergo a common dissociation reaction giving a common product ion, for example *m/z* 369.3 for the CE and *m/z* 184.1 for PC and SM. In such cases a precursor ion scan (i.e. a scan of MS1 at fixed MS2) allows the identification of the CE, PC and SM precursor ions. Thus, both PC and SM components are identified by setting MS2 at *m/z* 184.1, and then scanning MS1, whereas the CE molecules are identified by selecting MS2 at *m/z* 369.1, followed by an MS1 scan. Such experiments were performed to identify all CE components using cholesteryl heptadecanoate (CE 17:0) as internal standard as described by Liebisch et. al (2006)[26]. The identified peaks were matched with the internally calibrated MSI data (Fig. 3) and identification was deemed positive if the masses agreed to within 2 ppm. Identified PCs, SMs and CEs are listed in supplementary information A.

Development of data processing pipeline

MSI data in the form of imzML files were loaded into MATLAB™ 2017a (Natwick, USA) unbinned, resulting in dataset with 20,000 to 40,000 pixels per section, depending on the imaged area, and 79,413 mass bins. Data processing steps that were used to reduce this complex data set and retain the lipid spec-

trum exclusively are described below.

Pre-processing

Spectral processing imaging data

For each image pixel, the spectrum was smoothed using a second order Savitzky-Golay filter with a frame length of nine data points. After smoothing, a post-measurement calibration was performed using DHB cluster peaks as lock-mass and a linear fit, see Fig. 3. In Fig. 2 a representative mean spectrum of calibrated MALDI-MSI data is shown.

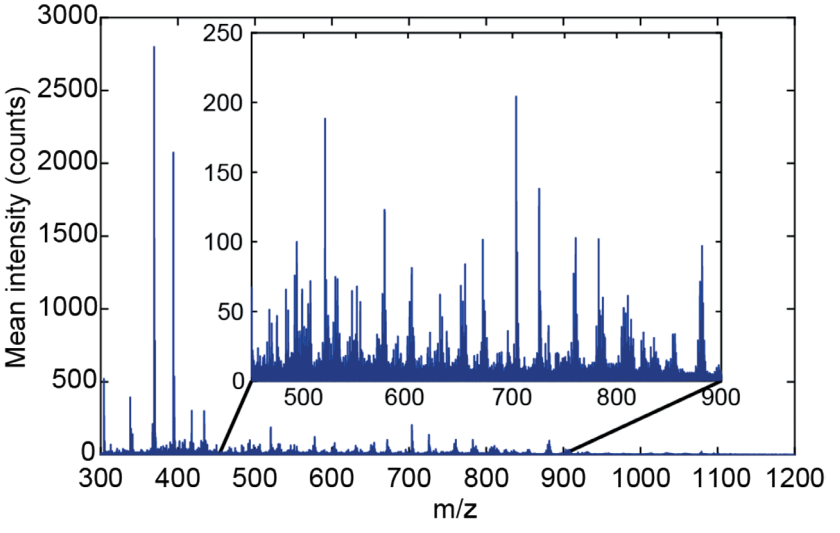

Figure 2: Typical MALDI-MSI spectrum. *P1-4 calibrated, mean spectrum, non-normalized*

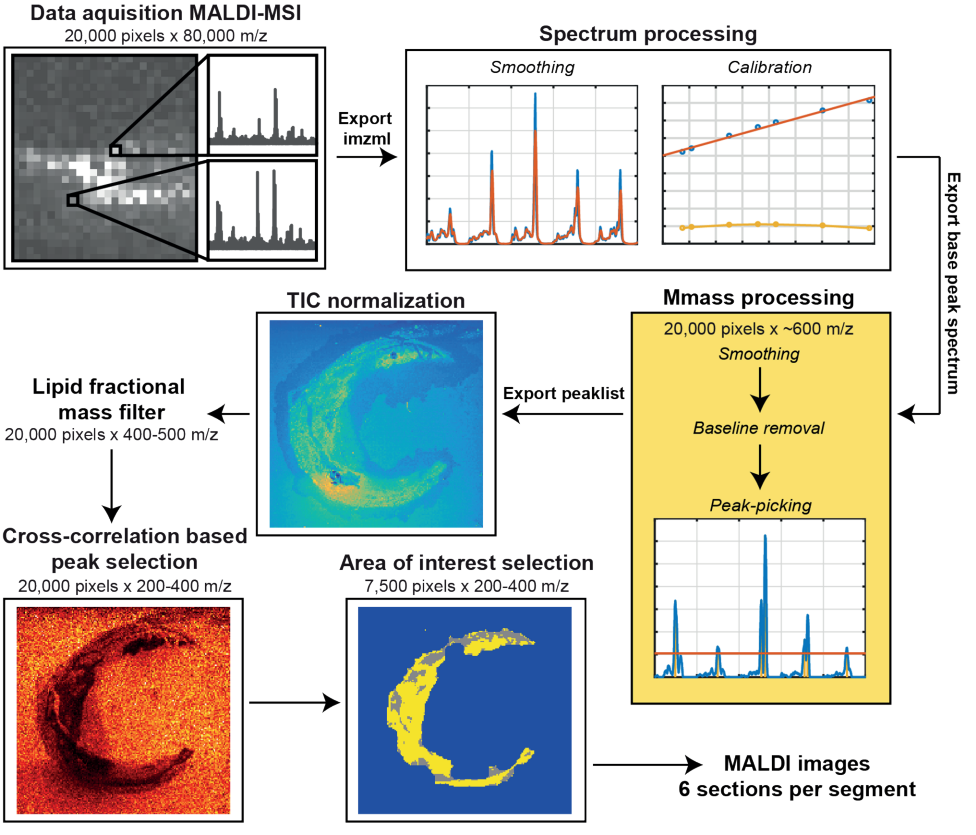

Figure 3: Flowchart of MSI data processing, showing the consecutive data processing steps of the MSI data. *The number of m/z data points is reduced from 80,000 to 200-400 by peak picking, elimination of non-lipid peaks, and cross-correlation-based background filtering. Also the number of informative pixels is reduced from 20,000 to 7,500*

Peak-picking

We perform peak-picking to make a pre-selection of the most important features of the data, for which we used the base peak (BP) spectrum because of the heterogeneous nature of our samples. The BP spectrum shows for each *m/z* value its maximum intensity measured over the entire MSI dataset [27]. Thus, the BP spectrum allows for detection of high intensity lipids that are only present in a small region. After calibration the BP spectrum was computed for the entire image and exported to mMass v5.5.0 [28]. We performed peak-picking in mMass by: (1) smoothing (Savitzky-Golay filter: window size 0.1 *m/z* and 2 cycles), (2) baseline correction (precision 15, relative offset 25), and (3) peak-picking (S/N threshold 10.0, peak-picking height 80%), see Fig. 3. The filter settings used

in this process were chosen heuristically: the additional peaks that are selected with less restrictive parameter settings are found to be removed in later processing steps. This supports the internal consistency of the work flow we propose here. The peak list was exported as a text file.

Imaging data processing

TIC-normalization and peak matching

The calibrated imzML measurement and the peak list were imported into MATLAB™ (The MathWorks, Natick, MA, USA). The data was normalized using Total-Ion Current (TIC) normalization, see Fig. 3. The peak list exported from mMass was used to make a pre-selection and to that aim, the peaks of the mMass-derived peak list were matched to the MSI data. The peak list was generated in mMass because the mMass peak-picking algorithm is better suited to process mass spectrometry data than the MATLAB `findpeaks` algorithm. For instance, in mMass the noise level is calculated locally and adjusted for every *m/z* value, which results in fewer false-positive peaks compared to the `findpeaks` algorithm of MATLAB.
Because the data processing pipeline was developed in MATLAB, the peaks of the mMass-derived peak list were matched to the MSI data imported in MATLAB. Using the `findpeaks` algorithm of MATLAB™ the peaks in the mean TIC normalized spectrum of the image were detected. Subsequently, these peaks were matched to the peaks found in the mMass BP spectrum with a mass tolerance of ±0.02 *m/z*; this resulted in ≈600 peaks. The data was subsequently binned around these peaks, with a bin width of ±1 data point. The sample pitch of the TOF mass analyzer used varied with mass-to-charge ratio, increasing from ±0.0075 *m/z* at 300 *m/z* to ±0.015 *m/z* at 1,200 *m/z*.

Lipid fractional mass filter

At this point, the dataset contains only the 600 most intense *m/z* peaks, which includes the lipids of interest as well as background and other non-lipid ions. To eliminate these unwanted signals, we applied several data reduction steps, aiming to maintain only lipid-representing *m/z* values. First, we applied a lipid fractional mass filter [27,29] to remove non-lipid peaks from the dataset. Masses that have a fractional mass outside the lipid fractional mass boundaries cannot be lipids and are therefore discarded, see Fig. 4.

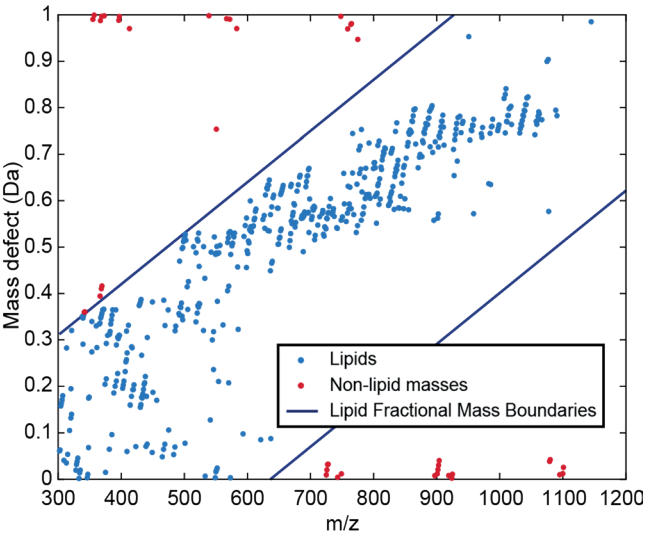

Figure 4: Lipid fractional mass filter. *Masses outside the lipid fractional mass boundaries cannot be lipids*

Cross-correlation-based peak selection

Subsequently, we performed peak selection based on background peaks to remove non-biological *m/z* values, similar to Fonville et al.[30]. In this method the correlation of images with a background reference peak was used to find matrix-related peaks and embedding medium-related peaks. Only masses that correlated negatively with this background reference mass were retained. The reference mass was chosen upon visual inspection; for all samples we used 419.2 *m/z* as the background reference mass, see Fig. 4 step 5. Features that are important for choosing a good reference mass are: (1) high intensity in background area, (2) low intensity in tissue area and, (3) smooth transitions between the two areas.
We use the background reference mass and compute the cross-correlation using the Pearson correlation coefficient;
We then took the 9 highest correlations to this reference mass and used these to calculate the reference to all masses in the spectrum. We then calculated the mean correlation of all these 10 references. If this was negative a mass would be marked as being non-background and retained. This step reduced the number of *m/z* values to 200-400 peaks.
For sections with highly calcified regions, as were present in P1, an extra processing step was necessary due to noise allocated to the presence of these regions. This additional step is further explained in the supplementary information B.

Area of interest selection

After elimination of the background and non-lipid peaks, we used a K-means clustering algorithm with N=2 clusters to identify lipid-rich tissue areas, see Fig. 5a. Small gaps in the data were filled by first dilating the positive structures in the image with a six pixel circular kernel (MATLAB™ function `imdilate`), see Fig. 5b, and subsequent removal with the same kernel (`imerode`), resulting in a continuous region of interest for lipid analysis, see Fig. 5c.

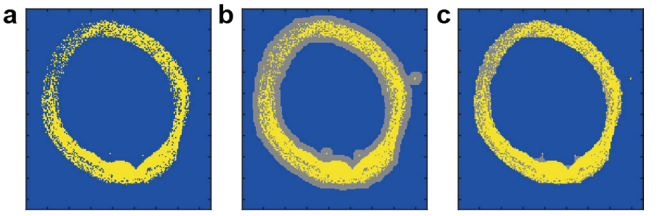

Figure 5: Pixel classification. *a. Pixel selection based on K-means clustering (yellow) (N=2), b.Dilated pixel selection to ensure continuity (gray), and c.Final continuous pixel selection.*

This selection of pixels containing lipid-rich tissue was additionally used to remove the last background peaks, by discarding masses that were more intense in the background pixels than in the lipid-rich tissue pixels. The combination of data processing steps reduced the datasets to 3,000-14,000 pixels, depending on section size, and 200-400 *m/z* values per measurement.

Reproducibility

With the data processing pipeline presented here, we intend to compare lipid profiles along the length of the carotid artery within a patient and between different patients. Therefore, we need to estimate the variability between experiments and the biological variation within the samples.
The coefficient of variation (CV) is a standardized measure for the variability in relation to the mean of the population, and was previously applied in MSI by Tillner et al.[31,32]. It is defined as the ratio of the standard deviation of a population(σ) to the mean of a population (μ): , expressed as a percentage. CV is invariant to the size of the population which makes it applicable to our relatively small dataset of six sections per segment [33]. Also, CV is applicable to data with a wide variation in mean values, which is the case for our MSI dataset. The CV represents population variability: the lower the CV in a set of repeated experiments, the higher is the reproducibility of the MSI measurement.
The quantitative reproducibility of these MSI datasets depends on the repeata-

bility of the measurement, which includes instrument parameters but also the stochastic ionization process and efficiency of transfer into the analyzer, the heterogeneity in the sample as prepared for imaging, and variability between the sections within one segment. We assessed the baseline reproducibility of the instrument by spotting two lipid standards on top of homogenized carotid artery tissue. 2 µL of ≈1000 pmol/µL PC 17:0/17:0 and 2 µL of ≈1560 pmol/µL CE 17:0 were spotted onto the homogenate. Both lipid standards were spotted and measured six times with the instrument settings reported in the methods section and from that data we calculated the CV value.
After data reduction, the tissue image dataset contains 200-400 *m/z* values, however, this data selection still contains isotopes. When calculating the CV, we used the de-isotoped *m/z* values (≈160) to avoid bias of similar isotope peaks. Every segment contains six tissue sections of which we calculate the mean intensity of the lipid-rich pixels for every *m/z* value. Resulting in 6 × 160 mean intensities, making up 160 populations for which we calculate the CV. We then calculated the mean CV value for every dataset () to allow comparison between the different segments.
We used the histopathology images to verify if all 6 sections within one segment were the same from a morphological perspective.

Results

Reproducibility

We found that the CV of the measurement of the lipid standard PC(17:0/17:0), is 10% for $[M+H]^+$, 8% for $[M+Na]^+$ and 16% for $[M+K]^+$. For cholesteryl esters we only looked at [M+Na]+, since it is the only ion that is stable in time of flight [34], and we found a CV of 16%. The relative intensity of the PC $[M+H]^+$ peak is about 100 times higher than that of PC $[M+K]^+$ and CE $[M+Na]^+$, which have about the same relative intensity. This means that PC $[M+H]^+$ is less susceptible to the influence of noise on the signal, explaining the lower CV value.
In the imaging data, tissue structure and content was not apparently different in the series of histologically stained sections within 1 mm segments. We thus assume that the CV values per segment represent MALDI-MSI measurement variability and not biological variability.
Fig. 6 shows the CV distribution of all measured segments. P2 shows the lowest of 12%, also P1-1, P1-2, P1-4 and P1-5 show relatively limited variability ranging from 14 - 25% for Furthermore, P1-1, P1-2 and P1-4 show some *m/z* values with a higher CV; most of these peaks could not be identified. P1-3 and A show significantly higher values of 44% and 40%, respectively. Computing the total variability across all peaks in all datasets without matching the segments,

results in a of 54%.
Furthermore, we expected to find that would be lower when only comparing adjacent sections (30-50µm apart), since biological variation between these sections is relatively minimal. Also we hypothesized that two sections that were measured on the same glass slide, and thus have had the exact same sample preparation and storing conditions, would show a lower . However, we did not find these conditions to influence .

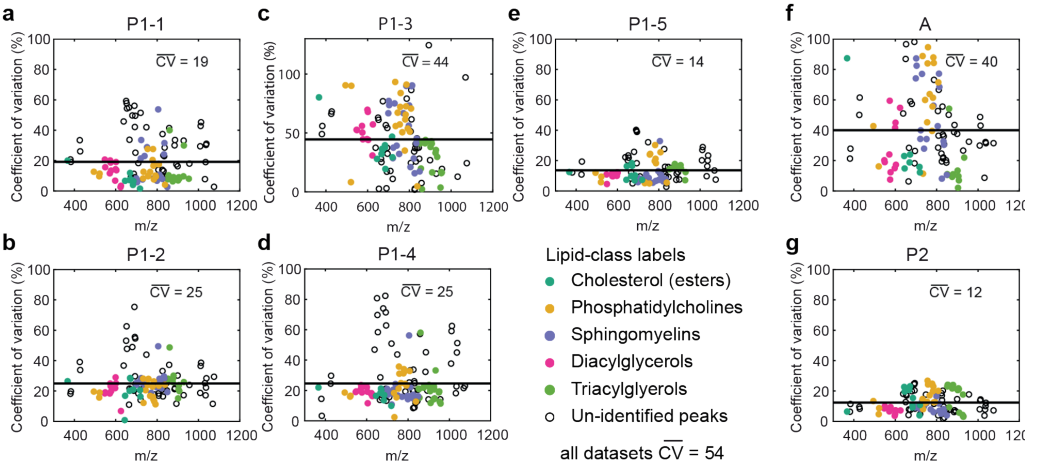

Figure 6: Coefficient of variation calculated using the mean intensity of every m/z value and comparing these values over all six measurements per segment. *The mean CV value across the m/z values is given, and depicted as a horizontal line. The different assigned lipid classes have been clustered and are color coded. a. P1-1, b. P1-2, c. P1-3, d. P1-4, e. P1-5, f. A, and g. P2.*

Relation between lipid content and plaque phenotype - preliminary observations

We hypothesize that the lipid composition of a plaque reflects plaque phenotype, and therefore expect to find specific lipid signatures in phenotypically different plaque structures. In our dataset we could examine thrombus, a key component in ischemic events, and changes in lipid profile occurring with development stage.

Thrombus

Segment P1-4 contained thrombus, see Fig. 7c, in which monoacylglycerols (MAG), diacylglycerols (DAG) and, triacylglycerols (TAG) were abundantly present. When we compared 300x300 µm regions of interest (ROIs) in tissue

segments, we found the DAGs to be more abundant in the thrombus region of P1-4 compared to another region in the same segment and also compared to other segments and other tissue samples. As such, a high concentration of DAGs appears to be thrombus-specific. In Fig. 7 an example of the distribution and intensity of DAG 34:2 is shown, in comparison to the other tissue sections measured. In the supplementary information C, a list of all peaks assigned as DAGs with distributions similar to DAG 34:2 are given.

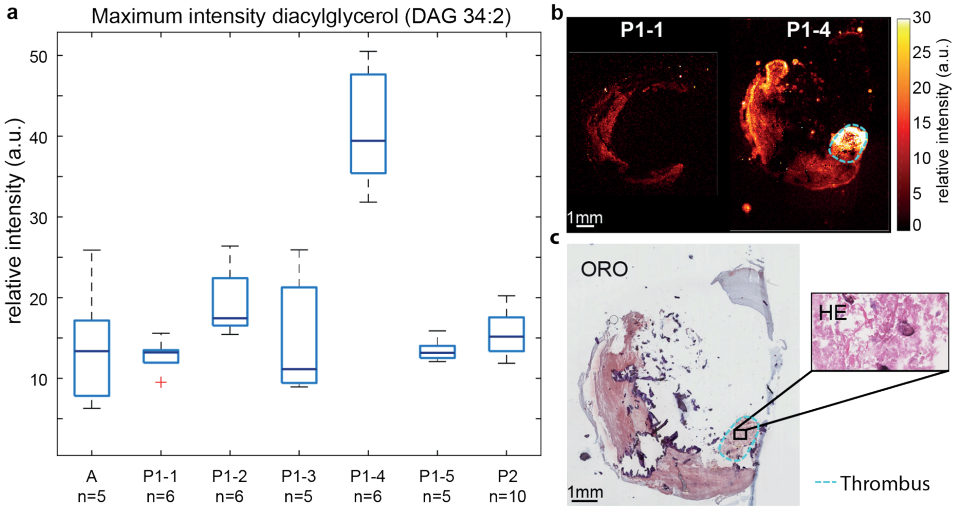

Figure 7: Distribution of diacylglycerol (DAG) 34:2 (m/z 575.51) *a. Boxplot of average intensity of diacylglycerol (DAG 34:2, [M+H-H2O]+) in a 300x300 µm region of interest in tissue segments. Expression in the thrombus-containing ROI of segment P1-4 (P1-4 Thr) is highly elevated, b. MALDI MSI of P1 segment 1 and 4. The thrombus region is outlined in cyan c. ORO staining of MALDI section and HE staining of adjacent section indicating thrombus*

Plaque development stage

The autopsy sample (sample A) contained a small fatty streak, which is an early manifestation of atherogenic changes in the vessel wall, as can be seen on the histological staining Fig. 8e, f and g. This sample was marked as an early stage plaque whereas the two CEA samples, P1 and P2, were advanced atherosclerotic plaques. We compared the differences in abundance of prominent lipid peaks between early- and late stage disease, and found that the early lesion is significantly enhanced in cholesteryl oleate, whereas the advanced plaques exhibits higher concentrations of cholesteryl linoleate, see Fig. 8a and Fig. 8c.

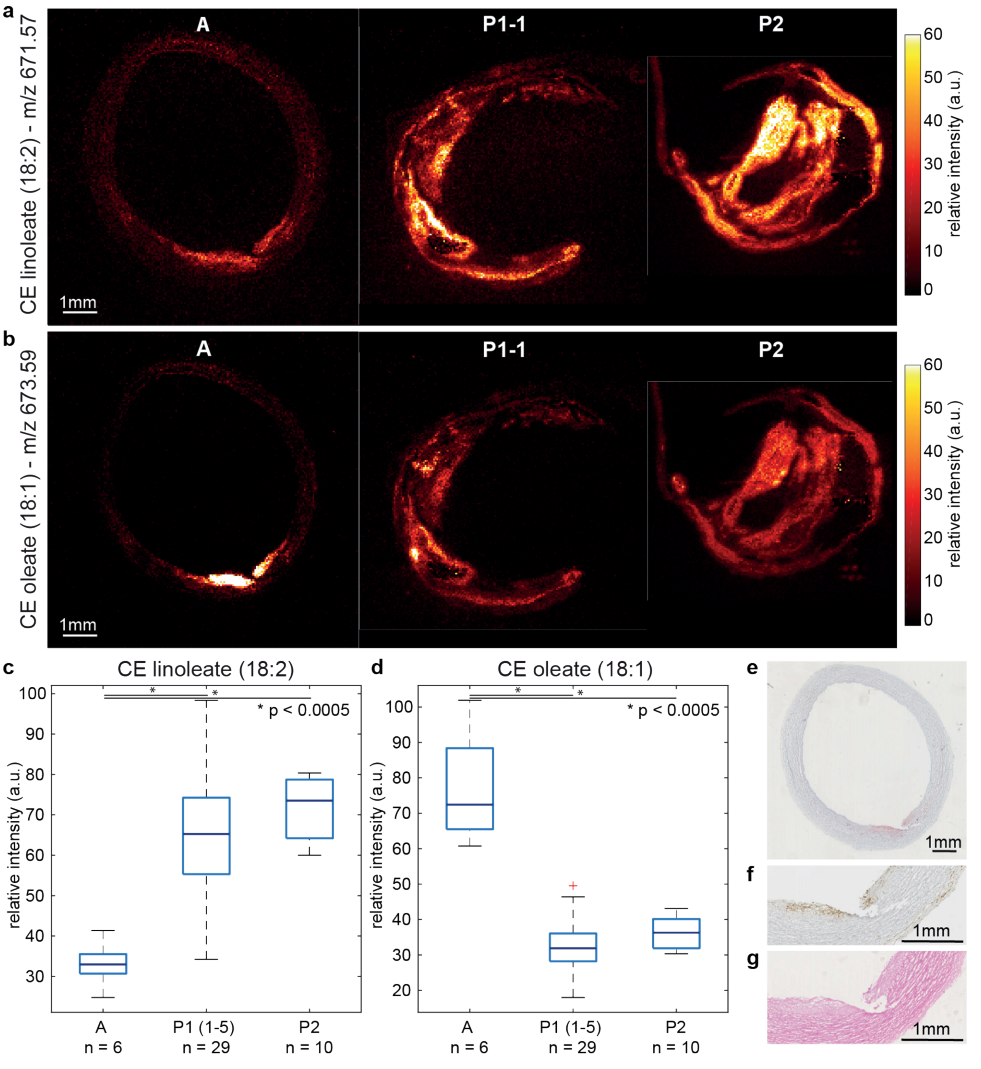

Figure 8: Distribution of cholesteryl linoleate (m/z 671.57) and cholesteryl oleate (m/z 673.59) *a. MALDI MSI of CE 18:2 in autopsy sample, P1-1 and, P2, b. MALDI MSI of CE 18:1 in autopsy sample, P1-1 and, P2, c. Box plot of maximum intensity (99th percentile) cholesteryl linoleate (CE 18:2), with over-expression in advanced plaques (P1 and P2), *p-value<0.0005, d. Box plot of maximum intensity (99th percentile) cholesteryl oleate (CE 18:1), with over-expression in early plaque (Autopsy), *p-value<0.0005, e. Oil Red O staining of MALDI MSI section, showing fatty streak, f. Immunohistochemistry CD68 stain (zoom, adjacent section), showing macrophages in fatty streak g. HE stain (zoom, adjacent section), showing fatty streak*

Discussion

In this study, we composed a framework to investigate the lipid content of human carotid atherosclerotic plaques. Arterial tissue was systematically processed for both MSI and histology, ensuring that MSI findings could be contextualized in terms of histopathology. Also, the data-processing pipeline presented here, can effectively and reproducibly assess the complex MALDI-MSI dataset in a way that focusses on the lipid distribution in the relevant tissue locations. Our protocol differs from previous MALDI-MSI studies on human atherosclerotic tissue [13,17-19] in the following ways. To our knowledge, this is the first study in which multiple carotid artery plaque specimens have been measured by MALDI-MSI. Based on this collection of carotid artery measurements, we optimized our data processing protocol. We have observed that the settings for discriminating tissue signal from background signal by negative cross-correlation, are dependent on the composition of the tissue investigated, in particular the presence of calcifications. We expect that this data-processing step may need to be adjusted when investigating other arterial beds, the method allows these adjustments. Secondly, this is the first MSI study on arterial tissue that allows measuring both differences between- and within-specimen lipid content and determines intra and inter variations in the tissue. Finally, we quantified the reproducibility of the samples.

We designed the data processing pipeline to be easily adjustable for other MALDI-MSI research purposes. We processed the data to the standard imzML format, which is supported by all MS instruments. Moreover, the processing pipeline is generated in mMass and MATLAB, which are both software packages in common use and easily available. The design of our processing pipeline makes the method applicable and adjustable for research in other labs.

We quantified the variability of the MALDI-MSI measurements by determining the coefficient of variation for the 6 tissue sections measured per segment. varied between 12-44%, with an average value of 25%. Two segments, P1-3 and A, showed relatively larger variability which may be attributed to different factors. In the case of segment P1-3, there were large calcifications present in the sample. This influenced the quality and amount of tissue per glass slide, which can be seen from the K-means pixel segmentation of these sections shown in the supplementary information D. These large variations in sections most likely contribute to an elevated CV.

In the case of segment A, this tissue is biologically different from P1 and P2, because it also contains the outer vessel wall layers, i.e. the tunica media and tunica adventitia. These layers are typically not as lipid-rich as the intimal layer. Therefore, the MALDI-MSI signal is much lower in these areas, resulting in a lower mean intensity value. When the mean values in the population are smaller,

the CV becomes more sensitive to relatively small changes. Also, differences in sample collection may have had an -- unknown -- impact. These results indicate that, in sections of lipid-rich atherosclerotic plaque, this protocol allows us to achieve a quantitative accuracy of approximately 12-20% for abundant lipids, which sets a lower limit for the detection of individual, local, or longitudinal variations in lipid profile.

Our analysis of three carotid plaque samples indicates that abundance of specific subtypes of cholesteryl esters may be related to atherosclerotic disease stage. Several studies have associated the presence of cholesteryl oleate (*m/z* 673.59) with early stage plaques [35-40]. Our MALDI-MSI data also showed significantly higher cholesteryl oleate intensity in the early plaque of sample A, compared to the advanced plaques in the CEA tissue specimens. In addition, cholesteryl linoleate (*m/z* 671.57) has been shown to be more abundant in advanced plaques, compared to early stage plaques [41]. While our limited number of samples does not allow us to draw quantitative conclusions, strikingly, we find cholesteryl oleate-to-linoleate ratios that are in close agreement with previous literature [42].

In our dataset, we also observed relatively high signal of DAG species in thrombus tissue. With the current dataset we cannot rule out the possibility that these DAG molecules represent fragmented TAGs. However, relative intensities of MALDI-MSI data of DAG molecules were different for thrombus compared to other segments, whereas their presumed TAG precursor molecules did not show this trend, indicating that we might be observing original DAG molecules, not TAG fragments. DAGs have at least two roles in biology, first, as an intermediate molecule for the synthesis of TAG and phospholipids, and second, as a regulator of protein kinase C (PKC) isozymes, which modulate several cellular processes[43]. Accumulation of DAGs has been associated with diabetes, cancer and cardiovascular disease [44]. PKC isoforms have also been associated with platelet activation and phosphatidylserine (PS) exposure [45], underlining our finding of a high abundance of DAGs in a thrombus.

In this study we imaged 6 sections per segment and quantified the reproducibility of these sections, which is indicative for the minimum fold change in intensity necessary to be significant. In future studies, in which we plan to investigate a larger collection of specimens, it is therefore possible to reduce the number of sections per site that we measure. Together with the semi-automated analysis presented here, and technological advances such as continuous scanning modes, this makes it feasible to perform systematic analyses of molecular lipid composition in larger sets of atherosclerotic specimens.

In conclusion, we have developed a protocol for MALDI-MSI measurements of lipids in human carotid plaque tissue using a new analysis pipeline. This method can now be applied to larger collections of carotid plaque specimens, allowing to assess whether the carotid plaque's lipid signature is correlated to plaque phenotype and vulnerability. If so, this opens up new opportunities in terms of diagnosis and patient stratification, and could enable the investigation of the effect of lipid-lowering medication on plaque composition and rupture-risk.

References

1 WHO | Cardiovascular diseases (CVDs). ***WHO*** (2018).

2 Virmani, R., Burke, A. P., Farb, A. & Kolodgie, F. D. Pathology of the Vulnerable Plaque. ***Journal of the American College of Cardiology*** **47**, doi:10.1016/j.jacc.2005.10.065 (2006).

3 Virmani, R., Kolodgie, F. D., Burke, A. P., Farb, A. & Schwartz, S. M. Lessons From Sudden Coronary Death A Comprehensive Morphological Classification Scheme for Atherosclerotic Lesions. (2000).

4 Schaar, J. ***et al.*** Terminology for high-risk and vulnerable coronary artery plaques. ***European Heart Journal*** **25**, 1077-1082, doi:10.1016/j.ehj.2004.01.002 (2004).

5 Virmani, R., Kolodgie, F. D., Burke, A. P., Farb, A. & Schwartz, S. M. Lessons from sudden coronary death: a comprehensive morphological classification scheme for atherosclerotic lesions. ***Arterioscler Thromb Vasc Biol*** **20**, 1262-1275 (2000).

6 Duewell, P. ***et al.*** NLRP3 inflammasomes are required for atherogenesis and activated by cholesterol crystals. ***Nature*** **464**, 1357-1361, doi:10.1038/nature08938 (2010).

7 Felton, C. V., Crook, D., Davies, M. J. & Oliver, M. F. Relation of plaque lipid composition and morphology to the stability of human aortic plaques. ***Arteriosclerosis, thrombosis, and vascular biology*** **17**, 1337-1345 (1997).

8 Rader, D. J. & Puré, E. Lipoproteins, macrophage function, and atherosclerosis: Beyond the foam cell? ***Cell Metabolism*** **1**, 223-230, doi:10.1016/j.Cmet.2005.03.005 (2005).

9 Silvestre-Roig, C. ***et al.*** Atherosclerotic Plaque Destabilization. ***Circulation Research*** **114**, 214-226, doi:10.1161/circresaha.114.302355 (2014).

10 Small, D. M. George Lyman Duff memorial lecture. Progression and regression of atherosclerotic lesions. Insights from lipid physical biochemistry. ***Arteriosclerosis (Dallas, Tex)*** **8**, 103-129 (1988).

11 Waksman, R. & Investigators, o. b. o. t. L. R. P. (TCT2018, San Diego).

12 Norris, J. L. & Caprioli, R. M. Analysis of Tissue Specimens by Matrix-Assisted Laser Desorption/Ionization Imaging Mass Spectrometry in Biological and Clinical Research. ***Chem Rev*** **113**, 2309-2342, doi:10.1016/j.biotechadv.2011.08.021.Secreted (2013).

13 Hutchins, P. M., Moore, E. E. & Murphy, R. C. Electrospray MS/MS reveals extensive and nonspecific oxidation of cholesterol esters in human peripheral vascular lesions. ***Journal of Lipid Research*** **52**, 2070-2083, doi:10.1194/jlr.M019174 (2011).

14 Lehti, S. ***et al.*** Spatial Distributions of Lipids in Atherosclerosis of Human Coronary Arteries Studied by Time-of-Flight Secondary Ion Mass Spectrometry. ***The American Journal of Pathology*** **185**, 1216-1233, doi:10.1016/j.Ajpath.2015.01.026 (2015).

15 Malmberg, P. ***et al.*** Localization of lipids in the aortic wall with imaging TOF-SIMS. ***Biochimica et Biophysica Acta - Molecular and Cell Biology of Lipids*** **1771**, 185-195, doi:10.1016/j.bbalip.2006.12.003 (2007).

16 Manicke, N. E. ***et al.*** Imaging of lipids in atheroma by desorption electrospray ionization mass spectrometry. ***Analytical Chemistry*** **81**, 8702-8707, doi:10.1021/ac901739s (2009).

17 Martin-Lorenzo, M. ***et al.*** Lipid and protein maps defining arterial layers in atherosclerotic aorta. ***Data in Brief*** **4**, 328-331, doi:10.1016/j.dib.2015.06.005 (2015).

18 Patterson, N. H. ***et al.*** Three-dimensional imaging MS of lipids in atherosclerotic plaques: Open-source methods for reconstruction and analysis. ***Proteomics*** **16**, 1642-1651, doi:10.1002/pmic.201500490 (2016).

19 Zaima, N. ***et al.*** Imaging mass spectrometry-based histopathologic examination of atherosclerotic lesions. ***Atherosclerosis*** **217**, 427-432, doi:10.1016/j.atherosclerosis.2011.03.044 (2011).

20 Edsfeldt, A. ***et al.*** Sphingolipids contribute to human atherosclerotic plaque inflammation. ***Arteriosclerosis, Thrombosis, and Vascular Biology*** **36**, 1132-1140, doi:10.1161/atvbaha.116.305675 (2016).

21 Zavodni, A. E. H. ***et al.*** Carotid Artery Plaque Morphology and Composition in Relation to Incident Cardiovascular Events: The Multi-Ethnic Study of Atherosclerosis (MESA). ***Radiology*** **271**, 381-389, doi:10.1148/radiol.14131020 (2014).

22 Wijeyaratne, S. M., Abbott, C. R. & Gough, M. J. A modification to the standard technique for carotid endarterectomy allowing removal of intact endarterectomy specimens: implications for research and quality control of preoperative imaging. ***Eur J Vasc Endovasc Surg*** **23**, 370-371 (2002).

23 Dekker, L. J. M. ***et al.*** A mass spectrometry based imaging method developed for the intracellular detection of HIV protease inhibitors. ***Rapid Communications in Mass Spectrometry*** **23**, 1183-1188, doi:10.1002/rcm.3981 (2009).

24 de Wit, N. M. ***et al.*** Altered Sphingolipid Balance in Capillary Cerebral Amyloid Angiopathy. ***Journal of Alzheimer's Disease*** **60**, 795-807, doi:10.3233/jad-160551 (2017).

25 Angel, P. M. ***et al.*** MALDI Imaging Mass Spectrometry as a Lipidomic Approach to Heart Valve Research. ***The Journal of heart valve disease*** **25**, 240-252 (2016).
26 Liebisch, G. ***et al.*** High throughput quantification of cholesterol and cholesteryl ester by electrospray ionization tandem mass spectrometry (ESI-MS/MS). ***Biochimica et Biophysica Acta (BBA) - Molecular and Cell Biology of Lipids*** **1761**, 121-128, doi:10.1016/j.Bbalip.2005.12.007 (2006).
27 McDonnell, L. A., van Remoortere, A., de Velde, N., van Zeijl, R. J. M. & Deelder, A. M. Imaging Mass Spectrometry Data Reduction: Automated Feature Identification and Extraction. ***Journal of the American Society for Mass Spectrometry*** **21**, 1969-1978, doi:10.1016/j.jasms.2010.08.008 (2010).
28 Strohalm, M., Hassman, M., Košata, B. & Kodíček, M. mMass data miner: an open source alternative for mass spectrometric data analysis. ***Rapid Communications in Mass Spectrometry*** **22**, 905-908, doi:10.1002/rcm.3444 (2008).
29 Jones, J. J., Stump, M. J., Fleming, R. C., Lay, J. O. & Wilkins, C. L. Strategies and data analysis techniques for lipid and phospholipid chemistry elucidation by intact cell MALDI-FTMS. ***Journal of the American Society for Mass Spectrometry*** **15**, 1665-1674, doi:10.1016/j.jasms.2004.08.007 (2004).
30 Fonville, J. M. ***et al.*** Robust data processing and normalization strategy for MALDI mass spectrometric imaging. ***Analytical Chemistry*** **84**, 1310-1319, doi:10.1021/ac201767g (2012).
31 Dill, A. L., Eberlin, L. S., Costa, A. B., Ifa, D. R. & Cooks, R. G. Data quality in tissue analysis using desorption electrospray ionization. ***Analytical and Bioanalytical Chemistry*** **401**, 1949-1961, doi:10.1007/s00216-011-5249-z (2011).
32 Tillner, J. ***et al.*** Faster, More Reproducible DESI-MS for Biological Tissue Imaging. ***Journal of The American Society for Mass Spectrometry*** **28**, 2090-2098, doi:10.1007/s13361-017-1714-z (2017).
33 Eisenberg, D. T. A., Kuzawa, C. W. & Hayes, M. G. Improving qPCR telomere length assays: Controlling for well position effects increases statistical power. ***American journal of human biology : the official journal of the Human Biology Council*** **27**, 570-575, doi:10.1002/ajhb.22690 (2015).
34 Fuchs, B., Süß, R. & Schiller, J. An update of MALDI-TOF mass spectrometry in lipid research. ***Progress in Lipid Research*** **49**, 450-475, doi:10.1016/j.plipres.2010.07.001 (2010).
35 Brown, J. M. ***et al.*** Combined Therapy of Dietary Fish Oil and Stearoyl-CoA Desaturase 1 Inhibition Prevents the Metabolic Syndrome and Atherosclerosis. ***Arteriosclerosis, Thrombosis, and Vascular Biology*** **30**, 24-30, doi:10.1161/atvbaha.109.198036 (2010).
36 Degirolamo, C., Shelness, G. S. & Rudel, L. L. LDL cholesteryl oleate as a predictor for atherosclerosis: evidence from human and animal studies on dietary fat. ***Journal of lipid research*** **50 Suppl**, S434-439, doi:10.1194/jlr.R800076-JLR200 (2009).
37 Lang, P. D. & Insull, W. Lipid droplets in atherosclerotic fatty streaks of human aorta. ***Journal of Clinical Investigation*** **49**, 1479-1488, doi:10.1172/jci106365 (1970).
38 Lee, E.-S., Shon, H. K., Lee, T. G., Kim, S.-H. & Moon, D. W. The regional ratio of cholesteryl palmitate to cholesteryl oleate measured by ToF-SIMS as a key parameter of atherosclerosis. ***Atherosclerosis*** **226**, 378-384, doi:10.1016/j.atherosclerosis.2012.11.003 (2013).
39 Melchior, J. T. ***et al.*** LDL particle core enrichment in cholesteryl oleate increases proteoglycan binding and promotes atherosclerosis. ***Journal of Lipid Research*** **54**, 2495-2503, doi:10.1194/jlr.M039644 (2013).
40 Weinmann, P. ***et al.*** Quantitative analysis of cholesterol and cholesteryl esters in human atherosclerotic plaques using near-infrared Raman spectroscopy. ***Atherosclerosis*** **140**, 81-88 (1998).
41 Spector, A. A. & Haynes, W. G. LDL Cholesteryl Oleate: A Biomarker for Atherosclerosis? ***Arteriosclerosis, Thrombosis, and Vascular Biology*** **27**, 1228-1230, doi:10.1161/atvbaha.107.147082 (2007).
42 Rapp, J. H., Connor, W. E., Lin, D. S., Inahara, T. & Porter, J. M. Lipids of human atherosclerotic plaques and xanthomas: clues to the mechanism of plaque progression. ***Journal of lipid research*** **24**, 1329-1335 (1983).
43 Bowden, J. A., Albert, C. J., Barnaby, O. S. & Ford, D. A. Analysis of cholesteryl esters and diacylglycerols using lithiated adducts and electrospray ionization-tandem mass spectrometry. ***Analytical Biochemistry*** **417**, 202-210, doi:10.1016/j.ab.2011.06.015 (2011).
44 Werner, M. H., Bielawska, A. E. & Hannun, Y. A. Quantitative analysis of diacylglycerol second messengers in human platelets: correlation with aggregation and secretion. ***Molecular pharmacology*** **41**, 382-386 (1992).
45 Heemskerk, J. W. M., Mattheij, N. J. A. & Cosemans, J. M. E. M. Platelet-based coagulation: different populations, different functions. ***Journal of Thrombosis and Haemostasis*** **11**, 2-16, doi:10.1111/jth.12045 (2013).

A Supplementary information: Identified lipids in plaque

Table S1. Identification of phosphatidylcholines (PC) and sphingomyelines (SM) by high resolution mass spectrometry (orbitrap) and MS/MS (triple quadrupole)

Experimental mass[a]	Calculated mass [M+H]+[b]	Delta (ppm)[c]	Identification by MS[2] [d]
369.35175	369.35156 [M-H_2O+H]+	-0.5	cholesterol
703.57471	703.57487	0.2	SM 16 18 1
725.55659	725.55922	3.6	Identified as [M+Na]+
731.60597	731.60617	0.3	SM 18 18 1
734.56912	734.56938	0.4	PC 16 16 0
758.56916	758.5694	0.3	PC 16 18 2
760.58483	760.58504	0.3	PC 16 18 1
780.55191	780.55373	2.3	Identified as [M+Na]+
782.56889	782.56938	0.6	PC 18 18 4
784.58494	784.58503	0.1	PC 18 18 3
786.60048	786.60068	0.3	PC 18 18 2
788.61586	788.61633	0.6	PC 18 18 1
810.60037	810.60068	0.4	PC 18 20 4
813.68395	813.68437	0.5	SM 18 24 2

a. Experimental mass (Orbitrap) for protonated species

b. Calculated mass (http://www.lipidmaps.org/tools/structuredrawing/GPmasscalc.php) for protonated species

c. Difference calculated and experimental mass (in ppm)

d. Identification by exact mass and MS/MS data (triple quadrupole). Numbers refer to chain lengths and number of unsaturations (e.g. SM 16 18 1 represents a sphingomyeline with one C16 and one C18 chain and one double bond; position double bond(s) not determined)

Table S2. Identification of phosphatidylcholines (PC) and sphingomyelines (SM) Na+ adducts by high resolution mass spectrometry (orbitrap) and MS/MS (triple quadrupole)

Experimental mass[a]	Calculated mass [M+Na]+[b]	Delta (ppm)[c]	Identification by MS[2] [d]
725.55659	725.5568	0.3	SM 16 18 1
780.55191	780.5514	-0.7	PC 16 18 2

a. Experimental mass (Orbitrap) for Na+ adduct

b. Calculated mass (http://www.lipidmaps.org/tools/structuredrawing/GP

masscalc.php) for Na+ adduct

c. Difference calculated and experimental mass (in ppm)

d. Identification by exact mass and MS/MS data (triple quadrupole). Numbers refer to chain lengths and number of unsaturations (e.g. SM 16 18 1 represents a sphingomyeline with one C16 and one C18 chain and one double bond; position double bond(s) not determined)

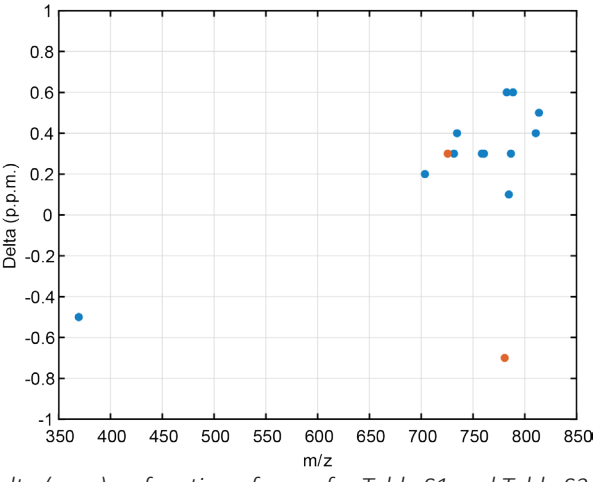

Figure S1. Delta (ppm) as function of mass for Table S1 and Table S2

Table S3.Identification of cholesteryl esters (CE) by triple quadrupole (precursor ion scan)

Experimental mass[a]	Calculated mass $[M+NH_4]^+$[b]	Identification by MS^2 [c]
614.6	614.5870	14:0
628.6	628.6026	15:0
640.6	640.6027	16:1
642.6	642.6183	16:0
654.6	654.6183	17:1
656.6	656.6340	17:0
666.6	666.6183	18:2
668.7	668.6340	18:1
682.7	682.6497	19:1
684.7	684.6653	19:0
696.7	696.6653	20:1
698.7	698.6809	20:0
716.5	716.6340	22:5

a. Experimental mass (triple quadrupole)
b. Calculated mass (http://www.lipidmaps.org/tools/structuredrawing/GPmasscalc.php) for NH4+ adduct
c. Peak present at mz 369.3 in precursor ion scan

B Supplementary information: Calcifications

Inspection of the images after filtering the background peaks, the retained lipid-rich peaks revealed areas of prominent chemical noise [1] associated with calcifications in the tissue as seen in histopathology, see Figure S2. Calcified tissue is often present in advanced atherosclerotic plaques. This hard material causes sectioning artefacts and has a limited adhesion to the glass slide. We hypothesize that the non-planarity and poor thermal coupling affect the observed peak structure.
After the first selection round, with the first reference mass, the masses remaining in the dataset are slightly different per dataset. This is due to the a-specific distributions in the images associated with calcifications, which cause the correlation of these images with our first reference mass to be located around the threshold value, causing erratic performance of this filter step. For this reason, it was not possible to select one specific reference mass to remove these peaks in all measurements. Consequently, for each measurement we determine a second reference mass by finding the most negatively correlated mass in comparison to a number of highly abundant lipids in the samples. These highly abundant lipids are stated in Table 1.

Table 1: Highly abundant lipids in all samples

m/z	Ion	Peak assignment
369.35	$[M\text{-}H_2O+H]^+$	Cholesterol
603.54	$[M\text{-}H_2O+H]^+$	Diacylglycerol (DAG) 36:2
671.57	$[M+Na]^+$	Cholesteryl ester (CE) 18:2
703.57	$[M+H]^+$	Sphingomyelin (SM) 34:1
725.56	$[M+Na]^+$	Sphingomyelin (SM) 34:1
782.57	$[M+Na]^+$	Phosphatidylcholines (PC) 34:1
804.55	$[M+Na]^+$	Phosphatidylcholines (PC) 36:4
881.76	$[M+Na]^+$	Triacylglycerol (TAG) 52:2

The second background mass was only accepted if it was highly anticorrelated to at least six of these eight lipids. With this second background mass, the same algorithm as with the first background mass was applied, and again

only masses with a negative correlation to this second background peak were retained.

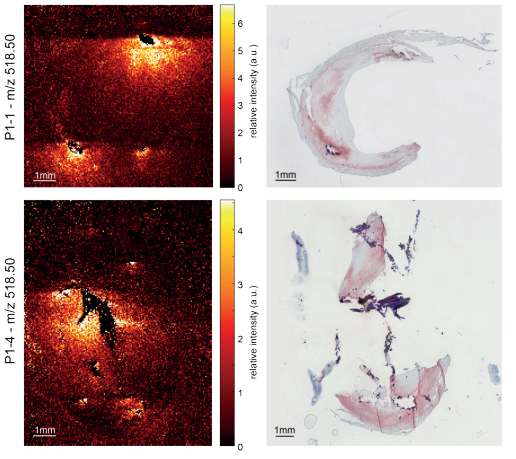

Figure S2. Examples of noise resulting from calcified regions in P1-1 and P1-4

C Supplementary information: Diacylglycerols in thrombus

Table S4. Diacylglycerols (DAG) associated with thrombus area

m/z [M-$H_2$0+H]+	Peak assignment
549.49	DAG 32:1
551.50	DAG 32:0
573.49	DAG 34:3
575.50	DAG 34:2
577.52	DAG 34:1
579.53	DAG 34:0
599.50	DAG 36:4
601.52	DAG 36:3
603.53	DAG 36:2
605.55	DAG 36:1
607.57	DAG 36:0
623.50	DAG 38:6
625.52	DAG 38:5
627.53	DAG 38:4
629.55	DAG 38:3

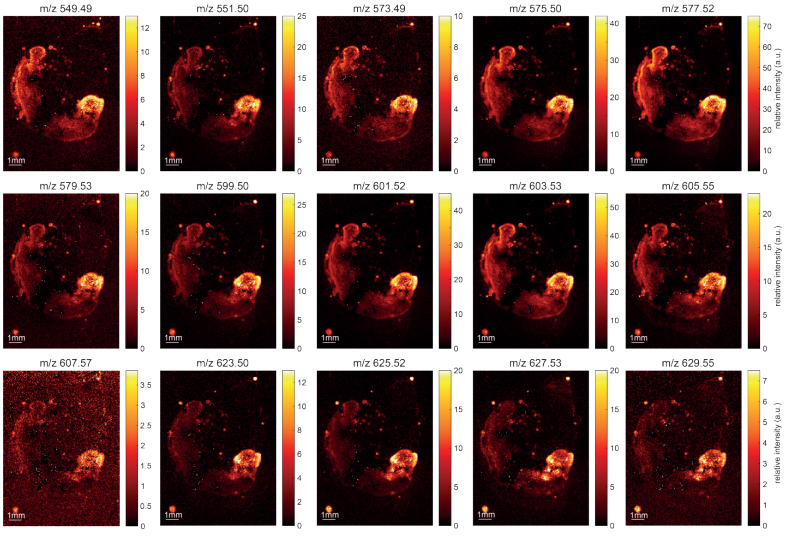

Figure S3. Distribution of all diacylglycerols(DAG)

D Supplementary information: Variability sections P1-3

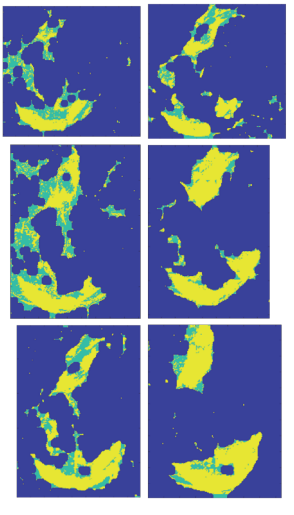

Figure S4. Lipid-rich tissue pixels, selected by K-means, for all P1-3 sections.

1. Krutchinsky AN, Chait BT. On the nature of the chemical noise in MALDI mass spectra. Journal of the American Society for Mass Spectrometry. 2002;13(2):129-34.

Chapter 6 A lipid atlas of human carotid atherosclerosis

Astrid M. Moerman*, Mirjam Visscher*, Nuria Slijkhuis, Kim van Gaalen, Bram Heijs, Theo Klein, Peter C. Burgers, Yolanda B. de Rijke, Heleen M.M. van Beusekom, Theo M. Luider, Hence J.M. Verhagen, Antonius F.W. van der Steen, Frank J.H. Gijsen, Kim van der Heiden#, Gijs van Soest#
*# These authors contributed equally

Based on: Lipid signature of advanced human carotid atherosclerosis assessed by mass spectrometry imaging, in rebuttal for Journal of Lipid Research

Abstract

Carotid atherosclerosis is a risk factor for ischemic stroke, one of the main causes of mortality and disability worldwide. The disease is characterized by plaques, heterogeneous deposits of lipids and necrotic debris in the vascular wall, which grow gradually and may remain asymptomatic for decades. However, at some point a plaque can evolve to a high-risk plaque phenotype, which may trigger a cerebrovascular event. Lipids play a key role in the development and progression of atherosclerosis. Using matrix-assisted laser desorption/ionization mass spectrometry imaging, we visualized the distribution of 194 lipids in 106 tissue sections of 12 human carotid atherosclerotic plaques. We performed unsupervised classification of the mass spectrometry dataset, as well as a histology-driven multivariate analysis. These data allowed us to compare the spatial lipid patterns with morphological plaque features that have been associated with high-risk plaque phenotype. The abundances of sphingomyelin and oxidized cholesteryl ester species were elevated specifically in necrotic intima areas, while diacylglycerols and triacylglycerols were spatially correlated to areas containing the coagulation protein fibrin. This study systematically investigates spatial lipid patterns in atherosclerosis, analyzes their relation to histological tissue type, and demonstrates a clear co-localization between plaque features and specific lipid classes and individual lipid molecules in high-risk atherosclerotic plaques.

Introduction

Atherosclerosis, a lipid-driven inflammatory disease of arteries, is one of the main causes of death worldwide [1]. The main driving mechanism for atherosclerotic plaque initiation is the gradual accumulation of lipids, originating from circulating lipoproteins, at sites of endothelial dysfunction in the vessel wall[2]. The influx of lipids and their subsequent modification in the vessel wall triggers inflammatory reactions that exacerbate the atherogenic process [3,4]. With disease progression, lipids start to play a dual role: they are deposited as metabolites of inflammatory processes but also form lipoproteins that act as signaling molecules, binding to a variety of macrophage-borne receptors [5]. Previous studies have found that the lipid content of atherosclerotic plaques is different at various stages of disease progression [6,7]. Thus, visualizing the molecular lipid composition of a plaque will give insight into local metabolic processes and may reflect the stage of the disease [8].
Matrix-assisted laser desorption/ionization mass spectrometry imaging (MALDI-MSI) is a label-free molecular imaging technique and is suitable for detection and visualization of lipids in tissue sections [9,10]. Systematic MSI studies of

lipid distribution in human atherosclerotic plaques have not been performed to date, and only small numbers of samples have been studied experimentally using a limited spectrum of lipid species [11–17]. We use a previously established MALDI-MSI pipeline for systematic imaging of lipids [18] to visualize the spatial distribution of 194 lipids in 106 tissue sections of 12 carotid atherosclerotic plaques, harvested at carotid endarterectomy surgeries in 12 patients. Analysis of this dataset identifies spatial lipid patterns in advanced atherosclerosis that transcend individual variability.

We processed tissue sections adjacent to those studied by MSI for a series of histological staining procedures to identify compositional features of plaque vulnerability, i.e. necrotic core, the thrombus-associated protein fibrin, erythrocytes and foam cells [19–21]. In this way we were able to compare spatial lipid patterns with gold standard histological assessment of plaque composition.

In this paper, we describe the systematic analysis of our highly dimensional MALDI-MSI dataset. Our initial approach was to assess the MALDI-MSI data for spatial correlations between lipids. Secondly, we considered the histological results and investigated correlations between lipids and compositional features of plaque vulnerability.

Thus, this unique study, in which the molecular lipid content of 12 human atherosclerotic plaques was systematically visualized with high resolution and contextualized in terms of gold standard histological plaque assessments, provides a first step towards identification of vulnerable plaque phenotypes based on a plaque's lipid signature. Its findings might guide the development of imaging techniques that can detect the lipid profile of a plaque *in vivo* and drive the identification of plaques, and thus patients, in need of focal or systemic preventive treatment.

Methods

Tissue collection and processing

Twelve human carotid endarterectomy (CEA) plaque specimens were surgically excised and were snap frozen and stored at -80°C until further processing. The surgery was performed using a protocol that preserves an intact lumen and plaque morphology [22]. Upon processing, CEA specimens were divided in 2 mm thick cross-sections. Each cross-section was embedded in 10% porcine type A gelatin (Sigma-Aldrich, The Netherlands) and cryosectioned (CM3050 S, Leica Biosystems) into 10 µm thick sections. Tissue sections were thaw-mounted on glass slides and stored at -80 °C. One slide was processed for MALDI-MSI, 6 other slides were histochemically stained. This study was performed according to the ethical guidelines sanctioned by the Ethics Board of Erasmus MC.

MALDI-MSI sample preparation, measurement and data reduction

MALDI-MSI experiments and data processing were performed according to the methods described in Visscher et al [18]. In short, we desiccated the tissue sections and applied 2,5-dihydroxybenzoic acid (DHB) matrix by sublimation (home-built sublimation system as described in Dekker et al.[23]). MALDI-MSI experiments were performed on a Synapt G2Si-TOF system (Waters, Manchester, UK), operated in positive ion mode at the instrument's resolution mode (single-pass reflectron TOF, mass resolution of 20,000), using a 2000Hz Nd:YAG (355 nm) laser with a pixel-size of 45x45 μm^2 and using Waters Research Enabled Software suite (WREnS). The mass range was 300-1,200 *m/z* and the laser fired 100 shots per pixel. The data was acquired using MassLynx v4.2 software (Waters, Manchester, UK), and HDI v1.4 was used to export the MSI data in imzML format and an in-house developed data processing pipeline in MATLAB™ 2017a (Natick, USA) and mMass software [24] was used to select tissue-specific lipid *m/z* values. We selected the lipid *m/z* values that were measured in more than 30% of all tissue sections and removed isotopes from the dataset, different adducts of the same molecule were retained. The data was log transformed for statistical analysis to comply with the assumptions of these methods[25]. All figures in this chapter show Synapt G2Si-TOF data.

Spatial cross-correlation

Per tissue section, the spatial correlation of a selection of 70 lipid images was calculated using the Pearson correlation coefficient:

$$R^2 = \frac{\sum((x_i-\bar{x})(y-\bar{y}))}{\sigma_x \sigma_y} .$$

The results of all tissue sections were averaged to obtain the average Pearson correlation coefficients for our dataset.

Unsupervised clustering algorithm

We calculated the optimal number of spectral components for this dataset and we applied non-negative matrix factorization (NMF) dimension reduction to the combined spectral data of all tissue sections, using an NMF toolbox for biological datamining [26–28]. We determined the optimum number of components based on dispersion coefficients [29].
Histology, histology segmentation and image registration The tissue section used in the MALDI-MSI experiment was stained for lipids by Oil Red O. Adjacent tissue sections were histochemically stained by: Miller's elastic stain, Martius

scarlet blue trichrome and hematoxylin-eosin. Based on the histological information, a segmentation image of the tissue section was drawn, in which plaque components were identified: necrotic core (NC), fibrin, foam cells (FC), erythrocytes and calcium. The segmentation images were registered to the MALDI tissue section by translation and scaling using an in-house developed point-based rigid image registration framework in MeVisLab (MeVis Medical Solutions AG, Germany), to enable correlation of histology and MALDI-MSI data. After registration, the mean spectrum for each plaque component was calculated per tissue section.

Multivariate analysis

To investigate the presence of lipids characteristic for a plaque component, we performed multivariate analysis. For all plaque components, we fitted an Orthogonal Projections to Latent Structures Discriminant Analysis (OPLS-DA) model [30] in SIMCA 15 (Umetrics, Sweden) comparing the mean spectra of the plaque component to the mean spectra of the rest of the tissue. In these models the intensities of the *m/z* values in the mean spectrum were defined as variables and the histological components were defined as the observations. Quality of fit and predictability of the model were reported by R^2 and Q^2 values respectively. Significance of OPLS-DA models was checked by seven-fold cross-validation analysis of variance (CV-ANOVA) [31] and the models were validated by permutation tests. If the model was significant, we extracted the Variable Influence on Projection (VIP) values >1.0, which were considered to be present in significantly different amounts [32].

Comparison unsupervised NMF clustering to histology-based multivariate analysis

Per NMF component spectrum we calculated a cut-off value of 0.4 times the normalized weight of that NMF component. We identified the *m/z* values with intensities above this cut-off value. We compared these *m/z* values to the *m/z* values with VIP > 1.0 in the multivariate analyses to check the correspondence between the NMF unsupervised clustering and the histology-based multivariate analysis.

Statistics

The VIP values > 1.0 of the significant OPLS-DA models were separately tested on all data, including the patients for which the MVA model was not significant. Wilcoxon Signed Rank test was used to statistically test the non-log fold chan-

ges in intensity between the segmented and all other tissue areas. *M/z* values that had a p-value ≤ 0.05 were considered statistically significant. Receiver operating characteristic (ROC) was used to determine the optimal cut-off intensity (maximum Youden's index) for the VIP *m/z* values.

Lipid identification

We performed lipid identification experiments in two ways. Firstly, we performed a lipidomics analysis on homogenized carotid endarterectomy tissue using the Lipidyzer platform (Sciex, Framingham, MA). Nine pieces of 50 mg CEA tissue was homogenized in 2 mL ice-cold methanol/MilliQ water (50/50 % (v/v)) with three 10 s bursts using an ultraturrax homogenizer. Homogenates were transferred to 2 mL Eppendorf tubes and stored on ice until centrifugation at 20,000 x g. The supernatant was collected and submitted to lipidomics analysis. 50 µL of tissue homogenate was mixed with the software pre-calculated amount of isotopically-labelled internal standard compounds in 13 lipid classes before liquid-liquid extraction with dichloromethane (DCM) /methanol. After 30 minutes, the lower phase was collected and the sample re-extracted with DCM. The combined extracts were dried under flowing N2 and re-suspended in running buffer (10 mM ammonium acetate in DCM/methanol 50/50 (% v/v)). The extracted samples were analyzed using the manufacturer-provided Lipidyzer SRM methods on a Shimadzu Nexera 20 UPLC system hyphenated to a Sciex 5500 Q-TRAP mass spectrometer equipped with a Selexion differential ion mobility module run with 1-propanol as a modifier. After analysis, lipid species quantification was performed using the Lipidyzer software.
Additionally, we performed MALDI-FTICR-MSI on a 12 T Bruker Daltonics solariX xR mass spectrometer equipped with dynamically harmonized ParaCell™, and a CombiSource™ (Bruker Daltonics, Bremen, Germany). The instrument was operated using ftmsControl (v2.1.0 Build 98; Bruker Daltonics), and data were collected using a transient length of 0.4194 s (512k data point time domain), resulting in an estimated resolution of 97,000 at *m/z* 400. MALDI-measurements were performed using the SmartBeam™-II laser (λ = 355 nm) operating at 200 Hz, at 21% power, and using the "Small" focusing setting (ablation area approximately 70x70 μm^2). A total of 50 shots were acquired per pixel, with a mass range covering 295-1,500 *m/z*. MSI analyses were performed at 70x70 μm^2 and 100x100 μm^2 pixel-size. Acquired data was loaded in SCiLS Lab (v2016b; Bruker Daltonics), and converted to imzML before further processing. We uploaded the FTICR data to the METASPACE annotation platform [33] and we searched the available annotation databases with a false-discovery rate (FDR) < 10%.

Results

MALDI-MSI of plaque lipids shows lipid class-specific spatial patterns

Twelve human carotid endarterectomy samples were processed into a series of 106 axial tissue sections to be imaged by MALDI-MSI and histology. Processing of MALDI-MSI data resulted in lipid images of 194 unique lipids, see supplementary Table S1. Demographic and histological information of the twelve human carotid plaque specimens can be found in Table 1 and Fig. 1, this demonstrates the heterogeneity in histological tissue composition between patients and within patients. Fig. 2 illustrates the variety in spatial distributions over 6 tissue sections, these tissue sections embody a representative subset of the 106 tissue sections, in terms of histological plaque composition. That is, all representative sections contained NC, four out of six sections contained fibrin areas of variable sizes (section 3, 4, 5, 6), section 2 and 4 contained a large FC area and in section 3 a large erythrocyte area was observed, see Fig. 2. We describe the observations in lipid patterns using these as examples, although the quantitative results we report were obtained on the complete data set.
In our dataset we observed lipids belonging to different lipid classes: cholesterol and cholesteryl esters (CEs), lysophosphatidylcholines (LPCs), phosphatidylcholines (PCs), sphingomyelin (SMs), diacylglycerol (DAGs) and triacylglycerol (TAGs). When stratifying the data by lipid class, we found that lipids belonging to the same lipid classes were distributed similarly over the plaque cross-sections, as quantified by their positive correlation coefficients. The average correlation heatmap of all tissue sections (Fig. 3a) and the heatmaps of the 6 representative tissue sections (Fig. 3b) are shown.

Patient	Age [yrs]	Sex	Intima area (μ ± SD (max)) [mm²]	% Necrotic core (μ ± SD)	% Foam cells (μ ± SD)	% Fibrin (μ ± SD)	% Erythrocytes (μ ± SD)	Number of sections	Representative tissue section*
A	56	F	19.0 ± 10.4 (34.4)	10.1 ± 9.0	1.1 ± 1.7	0.9 ± 1.9	0.0 ± 0.1	9	
B	69	M	22.2 ± 16.2 (54.5)	14.4 ± 18.9	6.1 ±7.8	10.3 ± 17.4	0.6 ± 2.1	12	
C	65	M	22.6 ± 6.9 (30.1)	5.2 ± 4.8	5.1 ± 6.7	1.7 ± 3.5	0.0 ± 0.0	7	1
D	75	M	23.0 ± 13.9 (54.5)	11.9 ± 17.6	4.6 ± 4.8	0.6 ± 1.1	3.7 ± 6.5	11	
E	75	M	25.4 ± 11.4 (47.2)	8.5 ± 9.4	2.9 ± 1.8	14.4 ± 13.6	0.0 ± 0.1	8	
F	63	M	26.6 ± 11.6 (43.8)	16.1 ± 11.0	3.1 ± 6.3	1.5 ± 2.3	0.3 ± 0.7	8	2
G	81	M	28.9 ± 17.2 (59.2)	24.8 ± 17.1	0.6 ± 1.3	5.0 ± 5.9	0.0 ± 0.1	10	
H	62	F	35.7 ± 11.1 (51.0)	8.7 ± 3.1	0.3 ± 0.4	5.6 ± 4.4	10.2 ± 7.7	5	3
I	69	M	49.6 ± 16.4 (70.1)	48.6 ± 23.8	3.0 ± 5.1	15.7 ± 14.2	0.0 ± 0.1	7	4
J	79	M	52.1 ± 28.5 (101.0)	35.3 ± 17.5	0.6 ± 1.1	23.6 ± 22.9	0.0 ± 0.0	8	5
K	69	M	53.3 ± 18.3 (77.4)	47.5 ± 21.3	0.9 ± 1.4	13.8 ± 14.5	0.3 ± 1.1	12	6
L	82	M	57.3 ± 37.9 (120.0)	25.6 ± 21.4	0.4 ± 0.7	32.0 ± 31.3	0.8 ± 1.4	9	

Table 1: Demographic information an histological tissue compositions per patient.
% area of histological component relative to total intima area. μ = mean, SD = standard deviation. μ ± SD: percentages were averaged over all tissue sections of a patient
μ ± SD intima area is given in mm2, areas were averaged over all tissue sections of a patient. Intima area of largest tissue section is reported between brackets
** Representative tissue sections are referred to in Fig. 1, 2 and 4.*

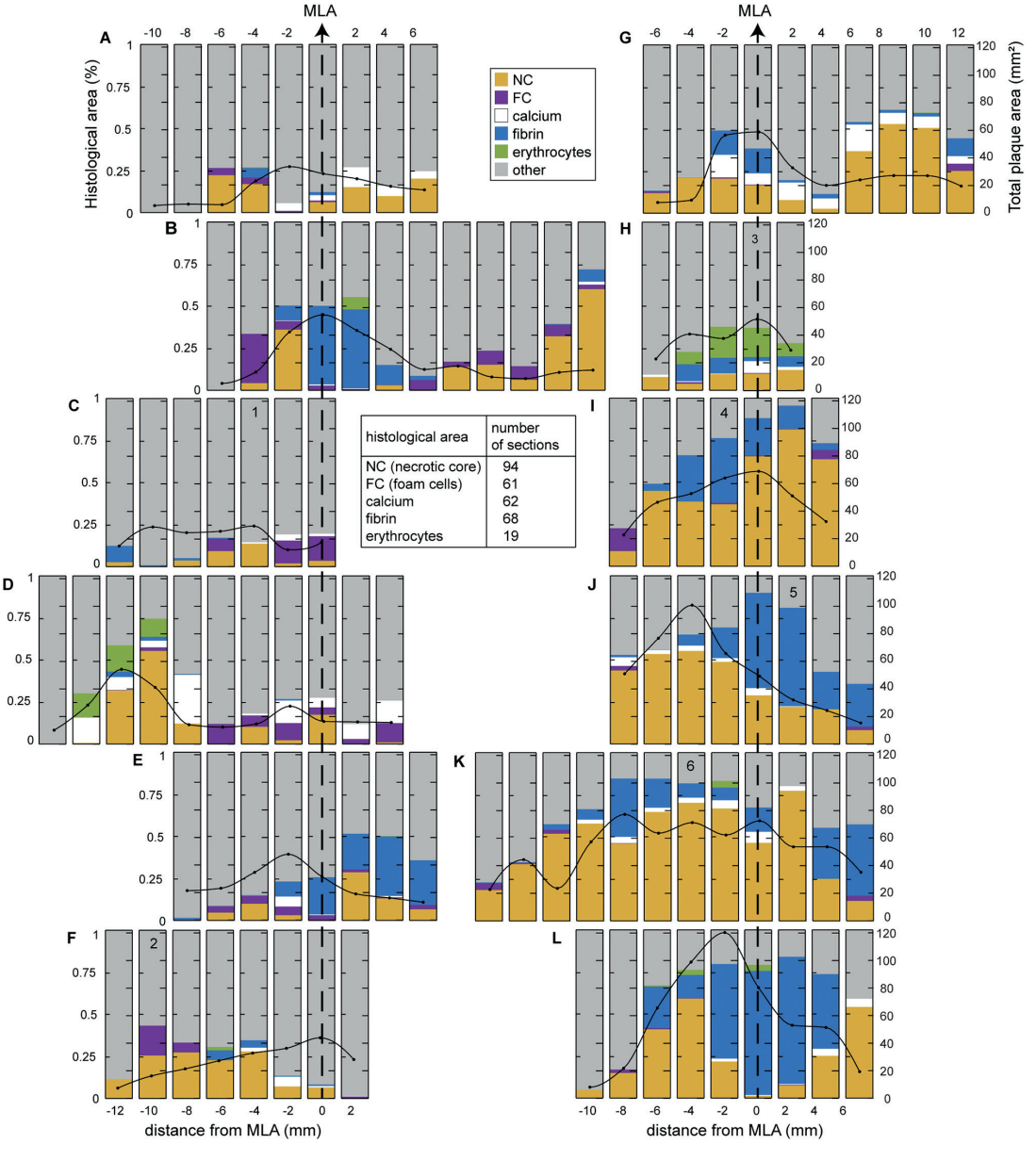

Figure 1: Histological tissue composition of 12 carotid plaques. *Overview of plaque components present in each carotid endarterectomy (CEA) sample. A-L: Bar graphs show the relative proportions (%) of necrotic core (NC), foam cells (FC), calcifications, fibrin and erythrocytes compared to the total intima area, see left axes.Tissue labeled as other was not segmented, this part of the tissue was histologically heterogeneous, but did not fit into any accepted classifications of atherosclerotic tissues. Total intima area represents the area of the intima layer of the vessel. The black line superimposed on the*

bargraph shows the total intima area in mm2, see right axis. The numbers in the graphs correspond to the exemplatory sections shown in Fig. 2, 3 and 5. The table in the middle shows the frequency of occurance of each histological component. MLA = minimal lumen area. Per CEA sample, the tissue section containing the minimal lumen area is denoted.

The spatial patterns of two prominent CEs, CE(18:2) and CE(18:1), show striking differences (Fig. 2). While CE(18:2) is often present throughout the cross-section, CE(18:1) is observed in high intensity spots around the lumen, while not abundant throughout the rest of the tissue sections (Fig. 2). CE lipids in general showed mild spatial cross-correlation with TAGs (Fig. 3).

In general, the spatial distribution of most CEs was similar to the distribution of cholesterol itself. However, the spatial distribution of a lipid with *m/z* 401.343, which can be annotated as 7-ketocholesterol[13], was distinct from that of other cholesterol-related molecules (Fig. 3-oxoChol/CE first row). The spatial location of *m/z* 401.343 and cholesterol and CE is depicted in Fig. 4b for two tissue sections. In addition, this molecule showed a unique spatial distribution as it did not show any cross-correlation with other lipids in our dataset and was also not correlated with histological components.

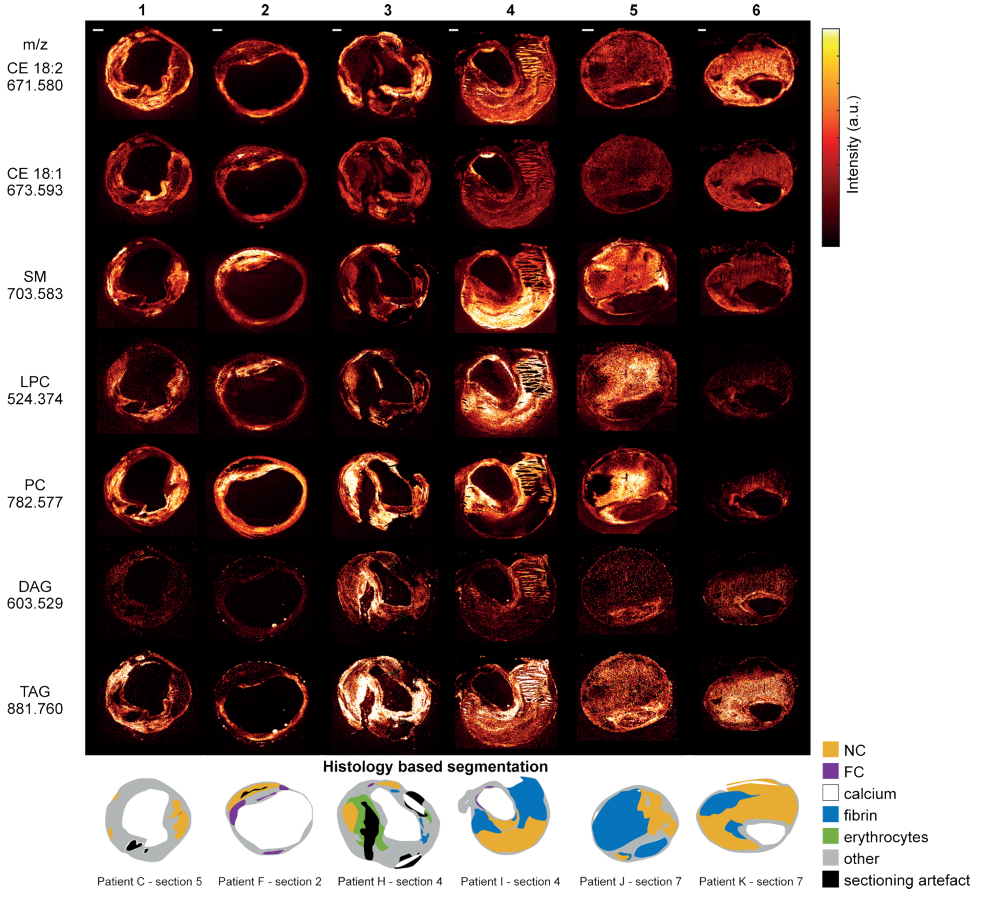

Figure 2: Overview of MALDI-MSI data for a selection of 7 lipids. *Data is shown for 6 tissue sections representative of the 106 section dataset, in terms of histological plaque composition. For comparison, histology segmentation images are also shown. The lipid images were normalized per m/z value, to enable reliable comparison of the distribution of a specific lipid in different tissue sections. Also, CE(18:2) and CE(18:1) are shown on the same intensity scale, as are DAG and TAG. Scalebars are 1 mm.*

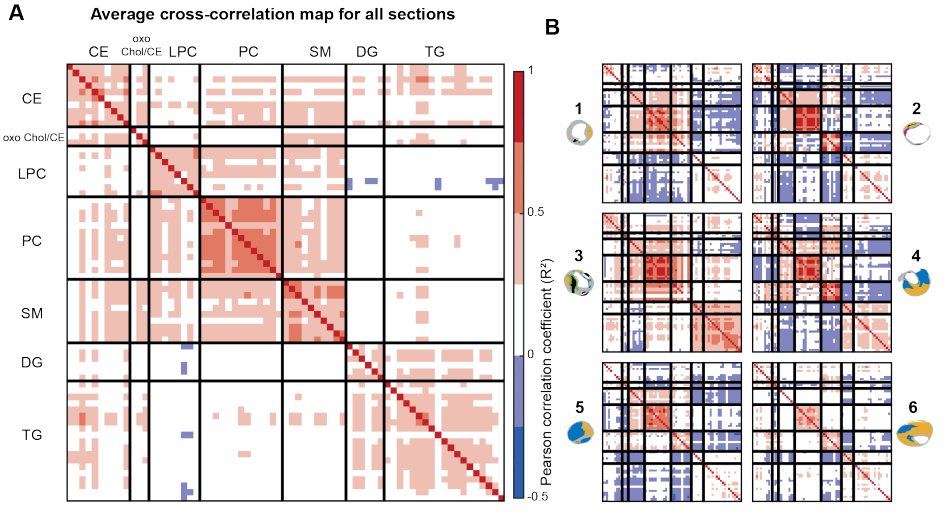

Figure 3: Spatial cross-correlation heatmaps. *X- and Y-axes are the same and represent a selection of 70 m/z values (Table S1), classified by lipid class. Per lipid class, the lipids are sorted from low to high m/z value. a) Average heatmap of all 106 tissue sections, showing a correlation within lipid classes and showing a moderate correlation between LPCs, PCs and SMs and also between DAGs and TAGs. b) Individual heatmaps of the 6 representative sections shown in Fig. 1. Heatmaps of section 1 and 3 show moderate positive correlation between PC and SM lipids, whereas section 2 shows a negative between these lipids.*

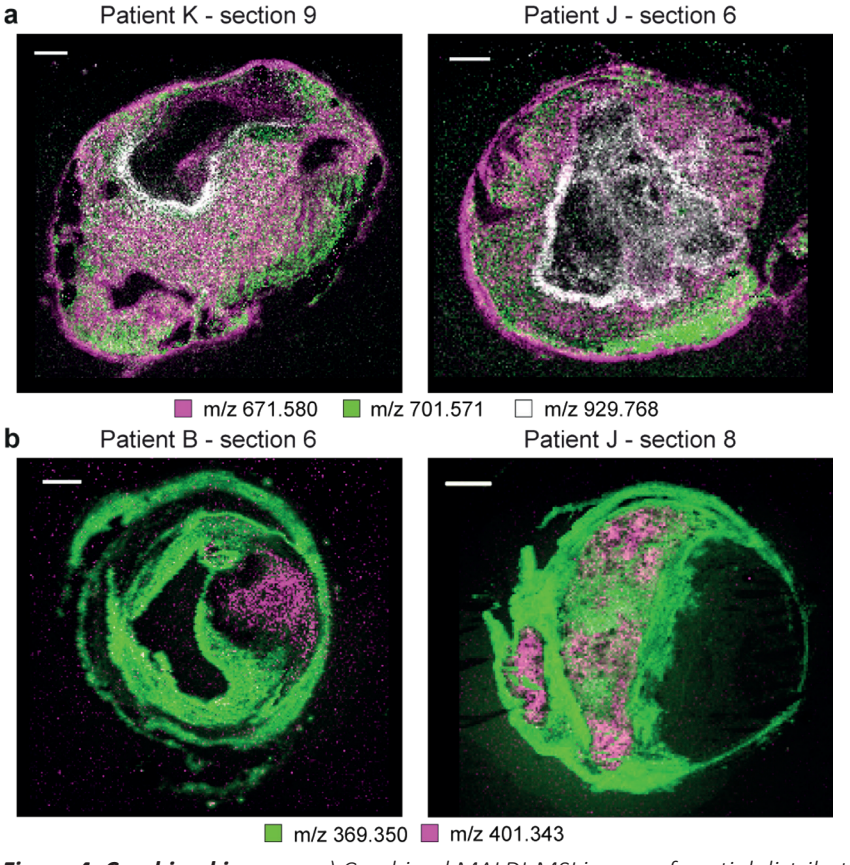

Figure 4: Combined images. *a) Combined MALDI-MSI image of spatial distributions of a CE in purple (m/z 671.580), SM in green (m/z 701.571) and a TAG in white (m/z 929.767) for three tissue sections. CE is found throughout the tissue section, while SM and TAG show a more localized spatial pattern. b) Spatial distribution of m/z 401.343, which can be annotated as 7-ketocholesterol, in purple and m/z 369.350, identified as cholesterol and CE fragments, in green. m/z 401.343 shows a spatial distribution distinct from that of other lipids in our dataset. Scalebars are 1 mm.*

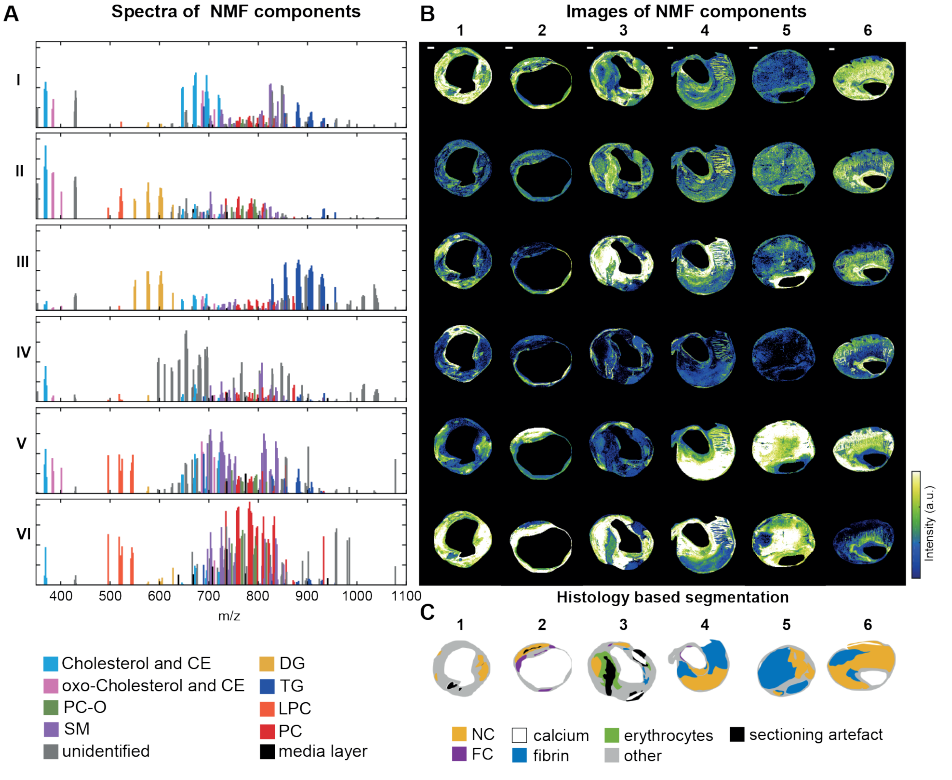

Figure 5: Unsupervised NMF of the 194 m/z-containing MALDI-MSI data. *a) NMF spectra of the components showing the weight of each m/z value to that NMF component. M/z values in the NMF component spectra are labelled according to their assigned lipid class, showing a clear separation of lipid classes by means of NMF. b) Corresponding NMF-weighted images of the representative sections, showing the spatial distribution and relative intensities of the NMF components. c) Corresponding histology-based segmentation suggesting co-localization between certain NMF components and histologically-relevant features. Scalebars are 1 mm.*

We found that the co-localization of SM, LPC and PC lipids varied strongly depending on the tissue section. In general, PCs were found to surround the lumen (Fig. 2 – section 2, 6) and sometimes to exude into thrombotic or inflamed areas (Fig. 2 – section 1, 3, 4, 5). The distribution of SMs did not deviate much of that of PCs in some tissue sections (Fig. 2 – section 1) but in others SMs were clearly more abundant in the necrotic parts of the tissue section (Fig. 2 – section 2, 4). These observations were quantified in the cross-correlation analysis: the degree of spatial correlation between SMs and PCs ranged from strong positive correlation, i.e. R^2>0.75, to strong negative correlation, i.e. R^2<-0.25 (Fig. 3b – tissue section 2). In most tissue sections, the highest mutual spatial correlation was found between PC lipids (Fig. 3). The distribution of PCs and LPCs was found to be weakly positively correlated in most tissue sections (Fig. 3). LPCs are structurally similar to PCs but lack one fatty acid branch. When assessing the tissue sections that showed marked variations in PC and SM distributions (i.e. Fig. 2 – section 2, 4, 5, 6) for the LPC distribution pattern, LPCs were highly abundant at the intersection of the locations that showed high SM and PC intensity.

In contrast, in most tissue sections, the spatial patterns of the DAG and TAG lipids showed moderate to high correlation and were distinctive from the distributions of other lipids except for some CEs (Fig. 3b - section 2, 4, 5, 6). However the intensities of measured DAG were much lower than those of TAG. Fig. 4a shows overlay images of three lipids identified as a CE, a SM and a TAG for two tissue sections. The variation in spatial distributions between these lipids, which belong to different lipid classes, can clearly be seen.

The spectral variety in the dataset can be captured by 6 spectral components

We reduced the dimensionality of the spectral data by unsupervised NMF, thereby extracting the major spectral patterns, using 6 components. Fig. 5a and b, shows the spectra of the NMF components and the spatial distributions of the 6 spectral components, respectively. Component I consisted mostly of oxidized and non-oxidized cholesterol and CE lipids. Component II was a combination of cholesterol, both oxidized and non-oxidized, DAGs and a proportion of LPCs. Component III was dominated by DAGs and TAGs. Component IV represented unidentified *m/z* values. Component V consisted of LPCs, SMs and cholesterol, both oxidized and non-oxidized, while component VI represented the PC moiety of the data.

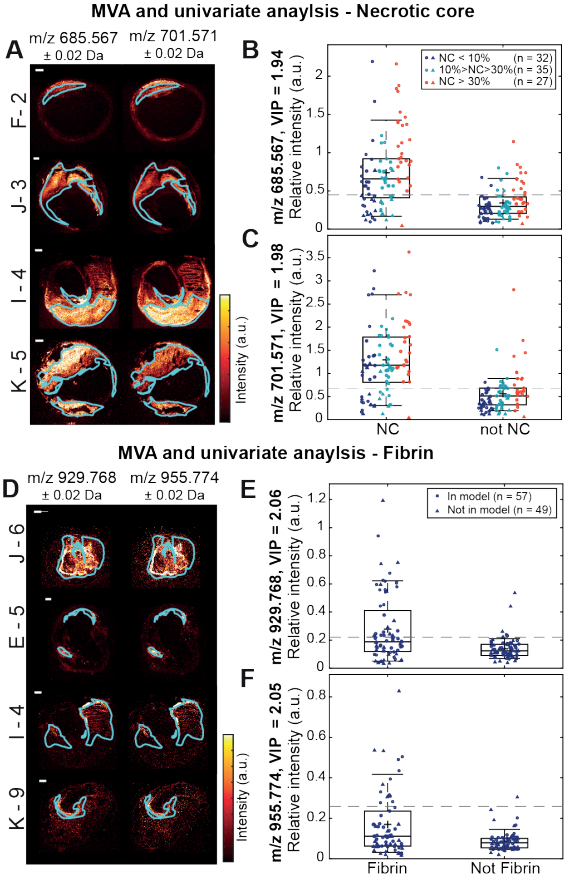

Figure 6: Univariate analysis comparing intensities in necrotic core (NC) versus not-NC areas and fibrin versus not-fibrin areas for two lipids. *a) MALDI-MSI images of m/z 685.567 (oxoODE-CE [M+Na]+) and m/z 701.571 (SM(34:2) [M+H]+) of 4 different tissue sections with superimposed the outlines of the NC segmentation b) Boxplots of m/z 685.567 and c) m/z 701.571 showing the mean intensity of the pixels in the NC area and in the not-NC area. Datapoints are colored according to the size of NC present in the corresponding tissue section. d) MALDI-MSI images of m/z 929.768 (TAG(58:9) [M+H]+ or TAG(56:6) [M+Na]+) and m/z 955.774 (TAG(60:10) [M+H]+ or TAG(58:7) [M+Na]+) of 4 different tissue sections with the outlines of the fibrin segmentation e) Boxplots of m/z 929.768 and f) m/z 955.774 showing the mean intensity of the pixels in the fibrin area and in the not-fibrin area. Only tissue sections containing NC or fibrin were included in these analyses. The dotted lines depict the maximum Youden's index, representing the optimal cut-off intensity value above which the m/z value is more likely to be associated with NC or fibrin. For m/z 685.567 the threshold is 0.45 and for m/z 701.571 it is 0.67, for m/z 929.768 it is 0.22 and for m/z 955.774 it is 0.26. All m/z values showed significantly different intensities between NC and not-NC or between fibrin and not-fibrin (p-value < 0.001). ○: data of the patients included in the multivariate model, Δ: data of patients that did not fit the model. Scalebars are 1 mm.*

Histological area	***R^2***	***Q^2***	***CV-ANOVA***	***Patients included in model*** *(number of patients in model / total number of patients)* **
NC	0.57	0.51	5.34E-19	All except D, H, L *(9/12)*
Fibrin	0.68	0.52	2.53E-07	B, C, F, G, J, K *(6/12)*
Foam cells	0.63	0.55	7.33E-15	All except D *(11/12)*
Erythrocytes	0.67	0.61	5.57E-05	B, F, H, I, K, L *(6/12)*

Table 2: OPLS-DA model parameters. *This table summarizes the parameters for OPLS-DA models comparing the mean spectrum of a histological area (NC, fibrin, FCs or erythrocytes) to the mean spectrum of tissue outside this histological area. The patients included in the model are reported in the last column of this table, all tissue sections of included patients were added to the model. R^2 and Q^2 values represent the quality of fit and predictability of the model respectively. Significance of OPLS-DA models was checked by sevenfold cross-validation analysis of variance (CV-ANOVA).*
** The number of patients for which R^2 and Q^2 values were highest. Minimal 6 out of 12 patients were included in the model.*

Correlation between spatial lipid patterns and histological plaque components

We compared the average spectra of different histological components by fitting a multivariate model. Four multivariate models, discriminating NC, fibrin, FCs and erythrocytes from all other tissue, were significant, i.e. $R^2 > 0.5$ and $Q^2 > 0.5$, for the combined data of at least 6 out of 12 patients. Model parameters of the significant models are listed in Table 2. The multivariate models determine the *m/z* values that have the highest influence on separation between two histological components, reported as Variable Influence for Projection (VIP) values. VIP values > 1.0 are considered significant[32] and these are reported in Table S2. We found SMs and oxidized CEs to be more abundant in NC than in other intima tissue, while DAGs and TAGs were found to be distinctive for areas containing fibrin. The VIP values resulting from the FC model were mostly SMs, while the erythrocyte-related VIP values were mostly PCs.

In order to quantitatively establish the contrast in lipid composition between various tissues, we performed two univariate analyses of the intensities of *m/z* values with VIP > 1.0 appearing in the multivariate models: one contrasting NC and not-NC, and another contrasting fibrin and not-fibrin. Fig. 6 illustrates the results for two *m/z* values. All *m/z* values that had significant VIP values in the multivariate model were significantly (p-value < 0.005) different between NC and not-NC in the univariate model, and the difference became stronger with increasing NC sizes. In the univariate analysis of fibrin, 58 out of 62 VIPs > 1.0

were significantly different between fibrin and not-fibrin. The four non-significant *m/z* values had VIP values lower than 1.14.

Comparison NMF – multivariate analysis – histology

Since certain NMF components appeared to co-localize with areas identified in histology (Fig. 5b and 5c), we investigated the similarities between the NMF spectra and the VIP values that were distinctive for histological components. The majority of the NC *m/z* values with VIP > 1.0, was found in NMF component V, i.e. mostly SMs and oxidized CEs (Fig. 7a).
For fibrin, most VIP *m/z* values were found in NMF component III (Fig. 7c). These VIP values are a set of DAG and TAG lipids that discriminated areas containing the thrombus-associated protein fibrin.
Fig. 7b and Fig. 7d illustrate the correspondence between the histology-based multivariate analysis and the NMF analysis for NC and fibrin areas. The majority of the significant VIP values for erythrocyte areas were most abundant in components VI and III and the VIP values associated with FCs corresponded to NMF component VI (Table 3).

Discussion

With this study, we aimed to visualize the spatial distribution of lipids over the human carotid atherosclerotic plaque and to investigate the relation between lipids and compositional features of plaque vulnerability. We imaged the spatial distribution of 194 lipids in 106 tissue sections of carotid atherosclerotic plaques. This study collects the largest MSI atherosclerosis dataset to date, spatially mapping the molecular lipid content of a series of human plaques, obtaining information on both the cross-sectional and the longitudinal composition of these plaques. Moreover, since we simultaneously processed adjacent tissue sections for histology, this study enabled the comparison of MALDI-MSI results with gold standard histological assessment of plaque stage.

In our dataset we observed lipids belonging to different lipid classes: cholesterol and CEs, LPCs, PCs, SMs, DAGs and TAGs. When stratifying the data by lipid class, we found that lipids belonging to the same lipid classes were distributed similarly over the plaque cross-sections, as quantified by their correlation coefficients. PC lipids in particular showed high mutual spatial correlation. PCs also showed spatial overlap with SMs and LPCs, while CEs were spatially correlated to DAGs and TAGs. However, the degree of spatial correlation was found to differ per tissue section. SMs and oxidized CEs co-localize in NC areas, and this co-localization became more apparent with greater NC size and thus with

bigger intima area. The presence of oxidized CEs in NC is in line with theories on pathogenesis of atherosclerosis: during plaque progression, LDL proteins are thought be become oxidized and trapped inside the vessel wall [2,38,39]. The presence of oxidized CE species in plaques, and their increase in abundance with lesion complexity, has been reported in literature [11,40–42]. Increased SM levels in plaques, compared to healthy artery have also been described before [14,43], as well as the higher abundance of SMs, relative to PCs, with increasing plaque severity [12,44]. Yet no previous study was able to visualize a clear co-localization of SM and oxidized CE lipid patterns with NC segmentations. We showed that the increased SM and oxidized CE levels concentrate in necrotic regions of the plaque, a finding that forms an important addition to the current understanding of the pathophysiology of atherosclerosis, and which also provides us a potential target for imaging NC presence or size in advanced plaques.

In literature, high levels of ceramides in serum, lipids that are structurally-related to SMs, have been associated with high-risk plaque [49,50]. We detected low levels of ceramides in CEA tissue using the Lipidyzer platform, but ceramide levels were probably below the detection limit of the MALDI-MSI experiments in this study or were suppressed by other ions.

Cholesterol, *m/z* 369, was abundantly present in the mass spectra of all tissue sections. Its presence was detected over the whole intimal area, though with local variations in intensity. However, in the MALDI-MSI analysis, in source fragmentation of cholesterol esters occurs, which forms the same fragment as cholesterol. Therefore, the annotation of *m/z* 369 to cholesterol is unreliable and no further conclusions can be drawn.

Most cholesterol esters showed a similar spatial distribution. Interestingly, however, the spatial distribution of an oxidized cholesterol lipid with m/z 401.343 was distinct from that of other cholesterol-related molecules. In addition, this molecule showed a unique spatial distribution as it did not show any cross-correlation with other lipids in our dataset, and was also uncorrelated with histological components. According to literature, m/z 401.343 can be annotated as 7-ketocholesterol [13], however, since identification based on MS/MS or chromatographic data is missing other possible isomers or isobars cannot be excluded. 7-ketocholesterol has been found in atherosclerotic tissue before [41,42,45] and shown to play a pro-atherogenic role, e.g. by mediating cell death [46,47].

DAGs and TAGs showed a spatial distribution that was distinct from that of PCs, SMs and LPCs. DAGs are present in tissue but may also form by in-source fragmentation of TAGs or PCs. The observation of distinct spatial patterns, captured by the appearance of DAGs but not TAGs in NMF component II, supports

the hypothesis that we detect intact species, although others may represent fragments of TAGs. When comparing the MALDI-MSI images of DAG and TAG molecules, we see similarities in the spatial patterns of DAG molecules and their presumed TAG precursor molecules. However, some specific patterns are only visible in the DAG images, which evidently proves the detection of endogenous DAG species.
Our multivariate analysis showed that a set of DAG and TAG lipids discriminated areas containing the thrombus-associated protein fibrin. A subset of TAG lipids was also associated with erythrocyte areas in the multivariate model. Previously [18], we described a co-localization between DAGs and thrombus in one of our tissue sections and this finding is thus confirmed in our current dataset. We hypothesize that the co-localization of DAGs and thrombotic plaque elements can be explained by the role that DAGs play in regulating protein kinase C (PKC), an enzyme known to induce an array of pro-atherogenic responses [34], including impairment of fibrinolysis [35] and platelet activation [36,37].

The tissue areas that contained FCs and erythrocytes were generally smaller than those of NC and fibrin. The lipids that were found to be distinctive for FC areas in the multivariate model were mostly PCs. When comparing the FC VIP values and the NMF component spectra, the majority of FC VIPs were present in the PC-dominated NMF component VI. Thus, there was large spatial overlap between the outcomes of the histology-based multivariate model and the NMF classification (Fig. 7). A subset of erythrocyte-associated *m/z* values – as found by the multivariate analysis – were also PC lipids. PC lipids are major constituents of healthy cell membranes [48], which probably explains why the spatial distribution of PC lipids was found to correlate with areas of high cellularity, e.g. FC- and erythrocyte-rich areas.

Limitations

Lipid identities could not be assigned to a subset of the 194 *m/z* values that were measured in the MALDI-MSI experiments. Most of the unknown masses in the MALDI-MSI data were not detected in the data captured by the Lipidyzer and FTICR measurements that were used for mass identification purposes. In addition, these unknown *m/z* values were not reported in the databases we consulted (Human Metabolome Database, SwissLipids and LipidMaps). The unidentified *m/z* values were dominating the spectrum of NMF component IV, while barely contributing to the spectra of the other NMF components. The distribution images of NMF component IV indicate that the unidentified *m/z* values were mostly present at the edges of the MALDI-MSI cross-sections. We assume that these images represent artefacts of the MALDI-MSI measurement

method.
In our FTICR dataset we detected some isobaric species. However, the possible lipid class the isobars belong to differ so much in terms of sensitivity and likelihood to be detected in MSI analysis that we are still able to annotate those isobaric lipids with high confidence.

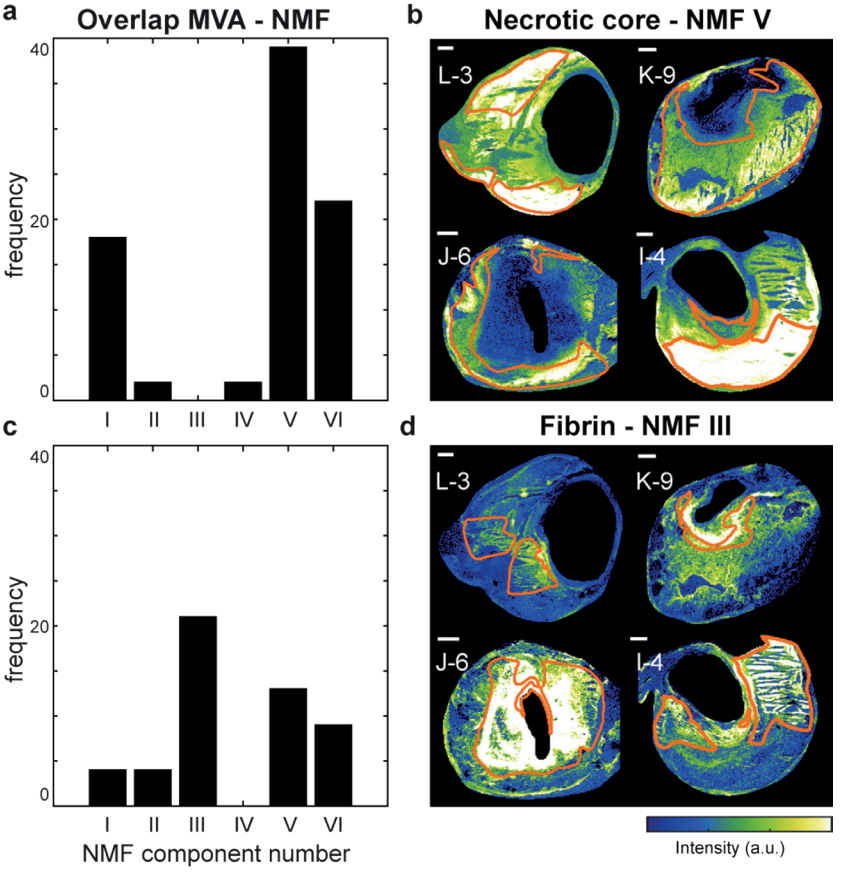

Figure 7. Overview of the correspondence between the histology-based multivariate analysis and the NMF analysis for NC- and fibrin-containing areas*. a) Bar graphs showing the number of NC VIP values above 1.0 that were allocated to the different NMF component spectra. Most NC VIP values were allocated to NMF component V. b) The results in a are illustrated by depicting the NMF weight images of component V for four tissue sections with superimposed NC segmentation. c) The number of fibrin VIP values above 1.0 allocated to the different NMF component spectra. Most fibrin VIP values were present in NMF component III. d) The NMF weight images of component III with fibrin segmentation for four tissue sections. Scalebars are 1 mm.*

NMF component	*NC*	*Fibrin*	*FC*	*Erythrocytes*
1	18	4	9	0
2	2	4	0	0
3	0	21	2	10
4	2	0	0	0
5	39	13	1	0
6	22	9	21	29

Table 3. *Number of **m/z** values with VIP > 1.0 for the different multivariate models and the NMF component in which these **m/z** values are most abundant.*

Conclusion

In our effort to identify lipids characteristic of high-risk plaque phenotype, we conclude that certain SMs and oxidized CEs are significantly higher expressed in NC and that the abundance of these molecules is correlated to the size of the NC. Interesting observations to build further studies on are the correlation between DAGs and TAGs and thrombus fragments, i.e. erythrocytes and fibrin, providing a possible marker for intra-plaque bleeding. Additionally, erythrocytes and FCs are correlated with PCs. These findings add to the current understanding of atherosclerosis pathogenesis. In the future, these marker lipids may be used as targets for imaging and therapeutic applications.

References

1. Global, regional, and national age-sex specific mortality for 264 causes of death, 1980-2016: a systematic analysis for the Global Burden of Disease Study 2016. ***Lancet*** **390**, 1151–1210 (2017).
2. Lusis, A. J. Atherosclerosis. ***Nature*** **407**, 233–241 (2000).
3. Duewell, P. ***et al.*** NLRP3 inflammasomes are required for atherogenesis and activated by cholesterol crystals. ***Nature*** **464**, 1357–1361 (2010).
4. Rajamaki, K. ***et al.*** Cholesterol crystals activate the NLRP3 inflammasome in human macrophages: a novel link between cholesterol metabolism and inflammation. ***PLoS One*** **5**, e11765 (2010).
5. Rader, D. J. & Puré, E. Lipoproteins, macrophage function, and atherosclerosis: Beyond the foam cell? ***Cell Metab.*** **1**, 223–230 (2005).
6. Rapp, J. H., Connor, W. E., Lin, D. S., Inahara, T. & Porter, J. M. Lipids of human atherosclerotic plaques and xanthomas: clues to the mechanism of plaque progression. ***J Lipid Res*** **24**, 1329–1335 (1983).
7. Small, D. M. George Lyman Duff memorial lecture. Progression and regression of atherosclerotic lesions. Insights from lipid physical biochemistry. ***Arterioscler. (Dallas, Tex)*** **8**, 103–129 (1988).
8. Felton, C. V, Crook, D., Davies, M. J. & Oliver, M. F. Relation of plaque lipid composition and morphology to the stability of human aortic plaques. ***Arterioscler. Thromb. Vasc. Biol.*** **17**, 1337–1345 (1997).
9. Norris, J. L. & Caprioli, R. M. Analysis of Tissue Specimens by Matrix-Assisted Laser Desorption/Ionization Imaging Mass Spectrometry in Biological and Clinical Research. ***Chem Rev*** **113**, 2309–2342 (2013).
10. Eberlin, L. S. ***et al.*** Desorption electrospray ionization then MALDI mass spectrometry imaging of lipid and protein distributions in single tissue sections. ***Anal Chem*** **83**, 8366–8371 (2011).
11. Hutchins, P. M., Moore, E. E. & Murphy, R. C. Electrospray MS/MS reveals extensive and nonspecific oxidation of cholesterol esters in human peripheral vascular lesions. ***J. Lipid Res.*** **52**, 2070–2083 (2011).
12. Lehti, S. ***et al.*** Spatial distributions of lipids in atherosclerosis of human coronary arteries studied by time-of-flight secondary ion mass spectrometry. ***Am. J. Pathol.*** **185**, 1216–1233 (2015).
13. Malmberg, P. ***et al.*** Localization of lipids in the aortic wall with imaging TOF-SIMS. ***Biochim. Biophys. Acta - Mol. Cell Biol. Lipids*** **1771**, 185–195 (2007).
14. Manicke, N. E. ***et al.*** Imaging of lipids in atheroma by desorption electrospray ionization mass spectrometry. ***Anal. Chem.*** **81**, 8702–8707 (2009).
15. Martin-Lorenzo, M., Alvarez-Llamas, G., McDonnell, L. A. & Vivanco, F. Molecular histology of arteries: Mass spectrometry imaging as a novel ex vivo tool to investigate Atherosclerosis. ***Expert Rev. Proteomics*** **13**, 69–81 (2016).
16. Mezger, S. T. P., Mingels, A. M. A., Bekers, O., Cillero-Pastor, B. & Heeren, R. M. A. Trends in mass spectrometry imaging for cardiovascular diseases. ***Anal Bioanal Chem*** **411**, 3709–3720 (2019).
17. Patterson, N. H. ***et al.*** Three-dimensional imaging MS of lipids in atherosclerotic plaques: Open-source methods for reconstruction and analysis. ***Proteomics*** **16**, 1642–1651 (2016).
18. Visscher, M. ***et al.*** Data Processing Pipeline for Lipid Profiling of Carotid Atherosclerotic Plaque with Mass Spectrometry Imaging. ***J Am Soc Mass Spectrom*** **30**, 1790–1800 (2019).
19. Stary, H. C. ***et al.*** A definition of advanced types of atherosclerotic lesions and a histological classification of atherosclerosis. A report from the Committee on Vascular Lesions of the Council on Arteriosclerosis, American Heart Association. ***Circulation*** **92**, 1355–1374 (1995).
20. Virmani, R., Ladich, E. R., Burke, A. P. & Kolodgie, F. D. Histopathology of carotid atherosclerotic disease. ***Neurosurgery*** **59**, S219-27; discussion S3-13 (2006).
21. Virmani, R., Kolodgie, F. D., Burke, A. P., Farb, A. & Schwartz, S. M. Lessons from sudden coronary death: a comprehensive morphological classification scheme for atherosclerotic lesions. ***Arter. Thromb Vasc Biol*** **20**, 1262–1275 (2000).
22. Wijeyaratne, S. M., Abbott, C. R. & Gough, M. J. A modification to the standard technique for carotid endarterectomy allowing removal of intact endarterectomy specimens: implications for research and quality control of preoperative imaging. ***Eur J Vasc Endovasc Surg*** **23**, 370–371 (2002).
23. Dekker, L. J. M. ***et al.*** A mass spectrometry based imaging method developed for the intracellular detection of HIV protease inhibitors. ***Rapid Commun. Mass Spectrom.*** **23**, 1183–1188 (2009).
24. Strohalm, M., Hassman, M., Košata, B. & Kodíček, M. mMass data miner: an open source alternative for mass spectrometric data analysis. ***Rapid Commun. Mass Spectrom.*** **22**, 905–908 (2008).
25. Veselkov, K. A. ***et al.*** Chemo-informatic strategy for imaging mass spectrometry-based hyperspectral profiling of lipid signatures in colorectal cancer. ***Proc Natl Acad Sci U S A*** **111**, 1216–1221 (2014).
26. Lee, D. D. & Seung, H. S. Learning the parts of objects by non-negative matrix factorization. ***Nature*** **401**, 788–791 (1999).

27. Li, Y. & Ngom, A. The non-negative matrix factorization toolbox for biological data mining. ***Source Code Biol Med* 8**, 10 (2013).
28. Verbeeck, N., Caprioli, R. M. & Van de Plas, R. Unsupervised machine learning for exploratory data analysis in imaging mass spectrometry. ***Mass Spectrom. Rev.* n/a**, 245–291 (2020).
29. Kim, H. & Park, H. Sparse non-negative matrix factorizations via alternating non-negativity-constrained least squares for microarray data analysis. ***Bioinformatics* 23**, 1495–1502 (2007).
30. Bylesjö, M. ***et al.*** OPLS discriminant analysis: combining the strengths of PLS-DA and SIMCA classification. **20**, 341–351 (2006).
31. Eriksson, L., Trygg, J. & Wold, S. CV-ANOVA for significance testing of PLS and OPLS® models. **22**, 594–600 (2008).
32. Galindo-Prieto, B., Eriksson, L. & Trygg, J. Variable influence on projection (VIP) for orthogonal projections to latent structures (OPLS). **28**, 623–632 (2014).
33. Palmer, A. ***et al.*** FDR-controlled metabolite annotation for high-resolution imaging mass spectrometry. ***Nat. Methods* 14**, 57–60 (2017).
34. Rask-Madsen, C. & King, G. L. Proatherosclerotic Mechanisms Involving Protein Kinase C in Diabetes and Insulin Resistance. ***Arterioscler. Thromb. Vasc. Biol.* 25**, 487–496 (2005).
35. D'Souza, A. ***et al.*** Pathogenesis and pathophysiology of accelerated atherosclerosis in the diabetic heart. ***Mol Cell Biochem* 331**, 89–116 (2009).
36. Konopatskaya, O. ***et al.*** Protein kinase C mediates platelet secretion and thrombus formation through protein kinase D2. ***Blood* 118**, 416–424 (2011).
37. Harper, M. T. & Poole, A. W. Diverse functions of protein kinase C isoforms in platelet activation and thrombus formation. ***J Thromb Haemost* 8**, 454–462 (2010).
38. Steinberg, D. The LDL modification hypothesis of atherogenesis: an update. ***J Lipid Res* 50 Suppl**, S376-81 (2009).
39. Steinbrecher, U. P., Zhang, H. F. & Lougheed, M. Role of oxidatively modified LDL in atherosclerosis. ***Free Radic Biol Med* 9**, 155–168 (1990).
40. Upston, J. M. ***et al.*** Disease stage-dependent accumulation of lipid and protein oxidation products in human atherosclerosis. ***Am J Pathol* 160**, 701–710 (2002).
41. Suarna, C., Dean, R. T., May, J. & Stocker, R. Human atherosclerotic plaque contains both oxidized lipids and relatively large amounts of alpha-tocopherol and ascorbate. ***Arter. Thromb Vasc Biol* 15**, 1616–1624 (1995).
42. Brown, A. J., Leong, S. L., Dean, R. T. & Jessup, W. 7-Hydroperoxycholesterol and its products in oxidized low density lipoprotein and human atherosclerotic plaque. ***J Lipid Res* 38**, 1730–1745 (1997).
43. Stegemann, C. ***et al.*** Lipidomics profiling and risk of cardiovascular disease in the prospective population-based bruneck study. ***Circulation* 129**, 1821–1831 (2014).
44. Smith, E. B. Intimal and medial lipids in human aortas. ***Lancet* 1**, 799–803 (1960).
45. Crisby, M., Nilsson, J., Kostulas, V., Bjorkhem, I. & Diczfalusy, U. Localization of sterol 27-hydroxylase immuno-reactivity in human atherosclerotic plaques. ***Biochim Biophys Acta* 1344**, 278–285 (1997).
46. Martinet, W. ***et al.*** 7-ketocholesterol induces protein ubiquitination, myelin figure formation, and light chain 3 processing in vascular smooth muscle cells.
47. Anderson, A. ***et al.*** 7-Ketocholesterol in disease and aging. ***Redox Biol.* 29**, 101380 (2020).
48. van Meer, G., Voelker, D. R. & Feigenson, G. W. Membrane lipids: where they are and how they behave. ***Nat. Rev. Mol. Cell Biol.* 9**, 112–124 (2008).
49. Cheng, J. M. ***et al.*** Plasma concentrations of molecular lipid species in relation to coronary plaque characteristics and cardiovascular outcome: Results of the ATHEROREMO-IVUS study. ***Atherosclerosis* 243**, 560–566 (2015).
50. Hilvo, M. ***et al.*** Development and validation of a ceramide- and phospholipid-based cardiovascular risk estimation score for coronary artery disease patients. ***Eur Hear. J* 41**, 371–380 (2020).

Supplemental material

Table S1. List of 194 lipids measured in human carotid atherosclerotic plaques.
m/z = mass measured in MALDI-MSI experiment using Synapt G2Si TOF system. For exact mass measured with FTICR and ppm values, we refer to the online available METASPACE at https://metaspace2020.eu/ data named Human CEA Patient H - section 4 and Human CEA Patient I - section 4.
lipid group = assigned lipid group based on database search, i.e. LipidMaps, HMDB.
ID = proven lipid identity, superscript denotes identification method: a. Lipidyzer MRM analysis, b. FTICR measurement combined with METASPACE database (FDR of maximum 10%), c. Identified in previous study [3], d. Identified from literature, LM: assigned from search in LipidMaps, HMDB: assigned from search in HMDB
adduct = positive ion adduct in identification experiment.
** Asterisks denote the lipids that were included in the cross-correlation analysis*
[d] Lipid identity not confirmed in identification experiments due to methodological limitations. However m/z values have been identified as 7-ketocholesterol [2,4], other cholesterol derivatives [4], LPCs [5] and oxo-ODE-CE [1] in literature and have been included as such in our cross-correlation analysis.

1. Hutchins, P. M., E. E. Moore, and R. C. Murphy. 2011. Electrospray MS/MS reveals extensive and nonspecific oxidation of cholesterol esters in human peripheral vascular lesions. J. Lipid Res. 52: 2070–2083.
2. Malmberg, P., K. Börner, Y. Chen, P. Friberg, B. Hagenhoff, J.-E. Månsson, and H. Nygren. 2007. Localization of lipids in the aortic wall with imaging TOF-SIMS. Biochim. Biophys. Acta - Mol. Cell Biol. Lipids. 1771: 185–195.
3. Visscher, M., A. M. Moerman, P. C. Burgers, H. M. M. Van Beusekom, T. M. Luider, H. J. M. Verhagen, A. F. W. Van der Steen, K. Van der Heiden, and G. Van Soest. 2019. Data Processing Pipeline for Lipid Profiling of Carotid Atherosclerotic Plaque with Mass Spectrometry Imaging. J. Am. Soc. Mass Spectrom. 30: 1790–1800.
4. Hasegawa, M., H. Hakamata, I. Matsunaga, and F. Kusu. 2011. Detection of oxysterols in oxidatively modified low density lipoprotein by MALDI-TOF MS. Eur. J. Lipid Sci. Technol. 113: 423–429.
5. Ravandi, A., S. Babaei, R. Leung, J. C. Monge, G. Hoppe, H. Hoff, H. Kamido, and A. Kuksis. 2004. Phospholipids and oxophospholipids in atherosclerotic plaques at different sTGes of plaque development. Lipids. 39: 97–109.

m/z ± 0.02	lipid class	ID	adduct	m/z ± 0.02	lipid class	ID	adduct
353.331	unknown			638.472	unknown		
367.343	Chol	Cholesterol derivative[LM,d]	[M-H2O+H]+	638.587	unknown		
369.350*	Chol	Cholesterol[c]	[M-H2O+H]+	640.603	unknown		
371.358	Chol	Cholesterol derivative[LM,d]	[M-H2O+H]+	645.561*	CE	CE(16:1)[a,b,c]	[M+Na]+
383.333	oxChol	Cholesterol derivative[LM,d]		647.577*	CE	CE(16:0)[a,b,c]	[M+Na]+
385.348	oxChol	Dehydro-cholesterol[LM,d]	[M+H]+	652.610	unknown		
401.343*	oxChol	7-keto-cholestol[d]	[M+H]+	654.628	unknown		
428.370	unknown			656.630	unknown		
429.375	unknown			666.495	unknown		
430.379	unknown			668.525	unknown		
431.385	unknown			668.622	unknown		
496.346*	LPC	LPC(16:0)[d]	[M+H]+	669.563	CE	CE(18:3)[a]	[M+Na]+
518.335*	LPC	LPC(18:3)[d]	[M+H]+	671.580*	CE	CE(18:2)[a,b,c]	[M+Na]+
520.351*	LPC	LPC(18:2)[d]	[M+H]+	673.593*	CE	CE(18:1)[a,b,c]	[M+Na]+
522.371*	LPC	LPC(18:1)[d]	[M+H]+	675.573	SM	SM(d32:1)[a,b]	[M+H]+
524.374*	LPC	LPC(18:0)[d]	[M+H]+	676.560	unknown		
542.322*	LPC	LPC(20:5)[d]	[M+H]+	678.623	unknown		
544.340*	LPC	LPC(20:4)[d]	[M+H]+	680.636	unknown		
546.351*	LPC	LPC(20:3)[d] LPC(18:0)[b]	[M+H]+ [M+Na]+	681.643	unknown		
549.488*	DAG	DG(32:1)[a]	[M-H2O+H]+	682.653	unknown		
551.509	DAG	DG(32:0)[a]	[M-H2O+H]+	683.658	unknown		
575.510*	DAG	DG(34:2)[a] DG(O-32:1)[b]	[M-H2O+H]+ [M+Na]+	685.567*	oxCE	Oxo-ODE-CE[d]	[M+Na]+
577.520*	DAG	DG(34:1)[a] DG(O-32:0)[b]	[M-H2O+H]+ [M+Na]+	687.566*	oxCE* CE	HODE-CE[b] CE(18:2)[a]	[M+Na]+ [M+K]+
579.534	DAG	DG(34:0)[a]	[M-H2O+H]+	689.570	CE TG	CE(18:1)[b] TG(38:1)[b]	[M+K]+ [M+Na]+
596.540	unknown			692.638	unknown		
598.558	unknown			693.567*	CE	CE(20:5)[a,b]	[M+Na]+
599.497*	DAG	DG(36:4)[a]	[M-H2O+H]+	695.581*	CE	CE(20:4)[a,b]	[M+Na]+
601.512*	DAG	DG(36:3)[a] DG(O-34:2)[b]	[M-H2O+H]+ [M+Na]+	695.659	unknown		
603.530*	DAG	DG(36:2)[a] DG(O-34:1)[b]	[M-H2O+H]+ [M+Na]+	696.673	unknown		
605.555	DAG	DG(36:1)[a]	[M-H2O+H]+	697.535*	SM	SM(32:1)[a,b]	[M+Na]+
610.572	unknown			697.591*	CE	CE(20:3)[a,b]	[M+Na]+
624.567	unknown			697.672	unknown		
626.591	unknown			699.606	CE	CE(20:2)[a,b]	[M+Na]+
627.544	DAG	DG(38:4)[a] DG(O-36:3)[b]	[M-H2O+H]+ [M+Na]+	701.571	SM	SM(34:2)[b]	[M+H]+

m/z ± 0.02	lipid class	ID	adduct	m/z ± 0.02	lipid class	ID	adduct
703.583*	SM	SM(34:1)[a,b,c]	[M+H]+	796.541	PC	PC(34:2)[a,b]	[M+K]+
705.589	SM	SM(34:0)[b]	[M+H]+	796.615	PC-O	PC(O-38:4) LM,HMDB,b	[M+H]+
707.542	unknown			798.548	PC	PC(34:1)[a,b]	[M+K]+
711.550*	oxCE* CE	CE(11:1D3) HMDB CE(20:4)[a]	[M+Na]+ [M+K]+	802.610	unknown		
717.578	unknown			803.617	unknown		
719.571*	CE	CE(22:6)[a,b]	[M+Na]+	807.641*	SM	SM(40:2)[a,b]	[M+Na]+
721.586*	CE	CE(22:5)[a,b,c]	[M+Na]+	808.609	PC	PC(36:2)[b]	[M+Na]+
723.544	SM	SM(34:2)[b]	[M+Na]+	810.610*	PC	PC(38:4)[b,c]	[M+H]+
725.565*	SM	SM(34:1)[a,b,c]	[M+Na]+	811.676*	SM	SM(40:0)[b]	[M+Na]+
727.566	SM	SM(34:0)[b]	[M+Na]+	813.695*	SM	SM(42:2) a,b,c	[M+H]+
729.590*	SM	SM(36:2)[a,b]	[M+H]+	815.710	SM	SM(42:1)[a,b]	[M+H]+
731.614*	SM	SM(36:1)[a,b,c]	[M+H]+	816.597	PC-O	PC(O-38:5) LM,HMDB,b	[M+Na]+
732.584	unknown			820.539*	PC	PC(36:4)[a]	[M+K]+
733.561	unknown			822.555	PC	PC(36:3)[a]	[M+K]+
734.580*	PC	PC(32:0)[a,b,c]	[M+H]+	823.592	SM	SM(40:2)[a]	[M+K]+
735.572	unknown			824.584	unknown		
736.577	unknown			825.610	SM	SM(40:1)[a]	[M+K]+
739.550	SM	SM(34:2) LM,HMDB	[M+K]+	827.622	unknown		
741.545*	SM	SM(34:1)[a,b]	[M+K]+	827.709*	TAG	TG(48:1)[a]	[M+Na]+
743.555	SM	SM(34:0) LM,HMDB	[M+K]+	828.620	unknown		
746.606	PC-O	PC(O-34:1) LM,HMDB,b	[M+H]+	829.619	unknown		
750.565	unknown			829.717*	TAG	TG(48:0)[a]	[M+Na]+
751.574	SM	SM(36:2)[a,b]	[M+Na]+	830.574	PC	PC(40:8)[b] PC(38:5)[b]	[M+H]+ [M+Na]+
753.585	SM	SM(36:1)[a,b]	[M+Na]+	832.600	PC	PC(38:4)[b]	[M+Na]+
755.552	unknown			834.637	unknown		
756.558*	PC	PC(32:0)[a,b]	[M+Na]+	835.673*	SM	SM(44:5)[b] SM(42:2) a,b	[M+H]+ [M+Na]+
758.574*	PC	PC(34:2)[a,c]	[M+H]+	837.690	SM	SM(42:1)[a,b]	[M+Na]+
760.587*	PC	PC(34:1)[a,b,c]	[M+H]+	839.590	unknown		
762.618	PC	PC(34:0)[HMDB,b]	[M+H]+	846.661	unknown		
764.652	unknown			847.593	unknown		
766.578*	PC-O	PC(O-36:5) LM,HMDB,b	[M+H]+	848.588	unknown		
766.754	unknown			848.676	unknown		
768.581*	PC-O	PC(O-36:4) LM,HMDB,b	[M+H]+	849.611	unknown		
772.542	PC	PC(32:0)[a,b]	[M+K]+	850.605	unknown		
774.580	unknown			851.629	SM	SM(42:2)[a,b]	[M+K]+
776.584	unknown			853.721*	TAG	TG(50:2)[a,b]	[M+Na]+
780.564*	PC	PC(34:2)[a,b,c]	[M+Na]+	855.592	unknown		
782.577*	PC	PC(36:4)[a,c] PC(34:1)[a,b]	[M+H]+ [M+Na]+	855.737	TG	TG(50:1) LM,HMDB,b	[M+Na]+
784.591*	PC	PC(36:3)[a,b,c]	[M+H]+	856.596	PC	PC(42:9) PC(40:6) HMDB	[M+H]+ [M+Na]+
786.610*	PC	PC(36:2)[a,b,c]	[M+H]+	857.596	unknown		
788.620*	PC	PC(36:1)[c]	[M+H]+	857.750*	TAG	TG(50:0)[a]	[M+Na]+
790.585	unknown			860.774	unknown		
792.600	PC-O	PC(O-38:6) LM,HMDB,b	[M+H]+	862.790	unknown		
794.614	PC-O	PC(O-38:5) LM,HMDB,b	[M+H]+	870.684	PC	PC(42:2) HMDB	[M+H]+

m/z ± 0.02	lipid class	ID	adduct
872.693	PC	PC(42:1) [HMDB]	[M+H]+
877.738*	TAG	TG(52:4)[a,b]	[M+Na]+
879.738*	TAG	TG(52:3)[a,b]	[M+Na]+
881.760*	TAG	TG(52:2)[a,b]	[M+Na]+
883.768*	TAG	TG(52:1)[a,b]	[M+Na]+
885.781*	TAG	TG(52:0)[a]	[M+Na]+
888.804	unknown		
889.726	unknown		
895.725	unknown		
897.736	PE-Cer	PE-Cer(t38:0)[b]	[M+Na]+
901.569	unknown		
901.732*	TAG	TG(54:6)[a,b]	[M+Na]+
903.751*	TAG	TG(54:5)[a,b]	[M+Na]+
905.751*	TAG	TG(54:4)[a,b]	[M+Na]+
907.773*	TAG	TG(54:3)[a,b]	[M+Na]+
909.794*	TAG	TG(54:2)[a,b]	[M+Na]+
923.750	unknown		
927.744*	TAG	TG(56:7)[a]	[M+Na]+
929.768*	TAG	TG(56:6)[a,b]	[M+Na]+
931.778*	TAG	TG(56:5)[a,b]	[M+Na]+
932.570	unknown		
933.790*	TAG	TG(56:4)[a]	[M+Na]+
940.770	unknown		
955.774*	TAG	TG(58:7)[a]	[M+Na]+
956.570	unknown		
958.583	unknown		
980.570	unknown		
984.602	unknown		
986.769	unknown		
1,010.774	unknown		
1,012.783	unknown		
1,014.798	unknown		
1,034.772	unknown		
1,036.783	unknown		
1,038.805	unknown		
1,040.817	unknown		
1,042.824	unknown		
1,077.583	unknown		

Table S2. Lists of m/z values with VIP>1.0 resulting from significant OPLS-DA models

Necrotic core

M/z values with VIP>1.0, resulting from the OPLS-DA model comparing NC with not-NC areas.

***m/z* value**	**VIP**
811.676	2.00
701.571	1.98
729.590	1.95
685.567	1.94
839.590	1.93
675.573	1.92
689.570	1.91
813.694	1.86
705.589	1.85
703.583	1.84
717.578	1.80
857.596	1.79
687.565	1.78
676.560	1.77
855.592	1.77
815.710	1.76
721.585	1.73
711.550	1.72
834.637	1.72
719.571	1.71
522.371	1.69
723.544	1.68
727.566	1.63
697.535	1.62
856.596	1.61
835.673	1.59
671.580	1.58
673.593	1.58
544.340	1.54
731.614	1.53
746.606	1.50
796.615	1.50
645.561	1.50
520.351	1.47
794.614	1.47

***m/z* value**	**VIP**
743.555	1.45
849.610	1.44
647.577	1.42
901.568	1.41
823.592	1.41
739.549	1.41
751.574	1.41
837.690	1.39
766.578	1.39
524.374	1.37
725.565	1.36
669.563	1.33
825.610	1.32
496.346	1.31
807.641	1.31
768.581	1.30
542.322	1.29
792.600	1.28
851.629	1.26
850.605	1.23
695.581	1.21
816.597	1.20
695.659	1.18
753.585	1.15
546.351	1.14
847.593	1.14
696.673	1.12
790.585	1.12
518.335	1.11
697.672	1.07
1,077.583	1.06
692.638	1.05
827.622	1.05
385.347	1.01

Fibrin

M/z values with VIP>1.0, resulting from the OPLS-DA model comparing fibrin with not-fibrin areas

***m/z* value**	**VIP**
931.778	2.12
929.768	2.06
955.774	2.05
383.333	2.01
927.744	1.86
599.497	1.84
401.343	1.84
905.751	1.81
901.732	1.78
603.529	1.78
933.790	1.78
601.512	1.74
721.585	1.71
923.750	1.68
909.794	1.66
907.773	1.63
903.751	1.62
605.555	1.62
829.717	1.62
579.534	1.61
575.510	1.61
857.596	1.59
551.509	1.55
856.596	1.52
792.600	1.51
857.750	1.51
549.488	1.46
577.520	1.45
666.495	1.44
853.721	1.43
855.737	1.42

***m/z* value**	**VIP**
746.606	1.42
889.726	1.39
796.615	1.37
895.725	1.36
877.738	1.34
794.614	1.32
719.571	1.29
676.560	1.26
827.709	1.25
627.544	1.23
766.578	1.22
1,040.817	1.21
883.768	1.20
733.561	1.19
879.738	1.17
685.567	1.15
855.592	1.13
701.571	1.13
816.597	1.12
1,038.805	1.12
897.736	1.11
762.618	1.11
1,036.783	1.11
729.590	1.08
839.590	1.07
1,042.824	1.06
385.347	1.04
705.589	1.03
881.760	1.02
885.781	1.02
692.638	1.00

Foam cells

M/z values with VIP>1.0, resulting from the OPLS-DA model comparing foam cell with not-foam cell areas.

m/z value	VIP
697.591	1.52
888.804	1.47
729.590	1.42
862.790	1.41
1,010.774	1.41
685.567	1.40
986.769	1.38
756.558	1.35
780.564	1.33
848.588	1.32
885.781	1.30
782.577	1.28
827.709	1.28
638.472	1.26
1012.78	1.26
784.591	1.26
732.584	1.24
850.605	1.24
829.717	1.24
755.552	1.22
808.609	1.22
860.774	1.22
758.574	1.22
734.580	1.21
772.542	1.18
627.544	1.17
824.584	1.17
848.676	1.16
786.610	1.16
760.587	1.15

m/z value	VIP
1,042.824	1.15
1,038.805	1.15
697.672	1.14
1,036.783	1.14
849.610	1.13
830.574	1.13
822.555	1.13
764.652	1.12
731.614	1.12
870.684	1.12
851.629	1.12
798.548	1.12
825.610	1.11
832.600	1.11
673.593	1.11
1,034.772	1.10
735.572	1.10
796.541	1.07
827.622	1.07
810.610	1.05
733.561	1.05
701.571	1.05
1,014.798	1.04
855.592	1.04
839.590	1.04
932.570	1.04
676.560	1.02
846.661	1.01
687.565	1.00

Erythrocytes

M/z values with VIP>1.0, resulting from the OPLS-DA model comparing erythrocyte with not-erythrocyte areas.

m/z value	VIP
932.570	1.35
780.564	1.35
782.577	1.34
958.583	1.33
756.558	1.32
758.574	1.32
786.610	1.31
784.591	1.31
768.581	1.31
760.587	1.30
832.600	1.29
956.569	1.29
810.610	1.29
790.585	1.28
734.580	1.28
796.541	1.28
830.574	1.26
808.609	1.26
772.542	1.25
735.572	1.24
798.548	1.24
820.539	1.22
984.602	1.21
822.555	1.21
788.620	1.20
905.751	1.19
980.570	1.17
766.578	1.15

736.577	1.14
903.751	1.11
923.750	1.11
762.618	1.11
707.542	1.10
796.615	1.08
897.736	1.07
816.597	1.07
929.768	1.07
755.552	1.05
877.738	1.03
931.778	1.03
955.774	1.02
652.609	1.01

Chapter 7 General discussion

This thesis aims at visualizing hemodynamic and tissue compositional patterns in highly stenotic carotid bifurcations. We focused on two characteristics of plaque pathology that could be indicative of the vulnerability of the plaque: the distribution of WSS over the plaque surface and the molecular lipid content of the plaque. This thesis is subdivided in two parts, that both initiate with the description of an image registration and data processing pipeline to assess the correlation between plaque composition and either WSS (Chapter 2) or spatial lipid distribution (Chapter 5). These pipelines were applied on two datasets of human advanced carotid plaques (Chapter 3 and 6). In addition we reported the spatial and temporal changes in WSS distribution during plaque progression in mice (Chapter 4).

This Chapter first discusses the main developments of this thesis in terms of image registration and data processing pipelines. Next, the main findings with respect to the correlation of both WSS and lipid patterns with compositional characteristics of plaque vulnerability are discussed and put into perspective.

7.1 Main developments of this thesis

7.1.1 Image registration framework for correlation of local WSS patterns to plaque histology

When hemodynamic parameters and tissue compositional information are derived from different imaging modalities, accurate co-registration of the different imaging results is vital. Depending on the type of imaging modalities that need registration, rigid and/or non-rigid body transformations have to be taken into account. We developed a method for registration of *in vivo* atherosclerotic vessel MR images, and their derived WSS patterns, to the compositional images of the excised plaque. Correlation of 3D MR data with 2D axial histologic cross-sections required an image registration pipeline that consisted of multiple intermediate registration steps and encompassed rigid and non-rigid registrations. Using this set of images, the 3D MRI geometry functions as ground-truth for 3D artery shape. The intermediate *ex vivo* and en face imaging steps are used to track tissue deformation occurring due to surgical excision and tissue processing.

Two important challenges when designing an image registration pipeline exist: 1. The assumptions made in each registration step, in order to obtain an optimal trade-off between registration accuracy and computing time, and 2. The careful evaluation of introduced tissue deformations, processing artefacts and registration errors, necessary to report a reliable comparison.

Considering the assumptions for registration, the image resolution of the imaging modalities should be critically assessed. In our study, the resolution of the *in vivo* MRI was lowest, making this imaging modality the most limiting in obtaining correct image registration. If clinical scan time allows this, this parameter can easily be improved by higher resolution imaging sequences. Increasing *in vivo* MR resolution and/or adding additional MR sequences would improve the landmark-based registration of *in vivo* and *ex vivo* imaging modalities, that is, if movement artefacts between the *in vivo* sequences can be avoided. High imaging resolution enables the recognition of tissue characteristics in consecutive imaging modalities, which greatly improves the accuracy of the registration step. Using landmark-based registration, as performed in our rigid registration steps, the set of points to be registered is sparse compared to registration based on full 3D images. Thus in terms of computation time, landmark-based registration allows for a very efficient (initial) registration [1].
Our non-rigid registration steps were segmentation-based: we matched the 3D lumen segmentations of consecutive imaging modalities. As with the landmark-based registration, the input for this registration step were not the full images, but only the discretized 3D lumen segmentations. Again this resulted in relatively short computation time. The registration accuracy of segmentation-based registration depends on the quality of the manually-drawn segmentation. As the implemented MRI sequences were optimized to achieve a clear lumen visualization, segmentation of the lumen was a fairly simple task on all imaging modalities and this segmentation-based non-rigid registrations was not limiting for the finally achieved registration accuracy.
In general, the inclusion of intermediate imaging modalities, i.e. *ex vivo* MRI and en face, in our pipeline improved the overall *in vivo* MRI-to-histology registration accuracy relative to registration without intermediate modalities. The use of intermediate imaging modalities has the advantage of adding additional levels of resolutions between *in vivo* MR imaging and histology, which reduces the likelihood that transformation parameters get trapped in local optima [2].

After the assumptions have been taken into account, their effect on the registration result need to be reported. In our case, no golden standard existed to assess the obtained registration quality of the complete pipeline. The validity of image registration frameworks can usually only be quantified by phantom studies, simulations or other registration methods [1]. The performance of sub-

parts of our registration framework could be tested by artificial perturbation of the imaging results and reverse registration [2]. For instance, the 3D *ex vivo* MRI scan could be converted into slices with en face resolution and artificially introduced artefacts. We could subsequently register the original *ex vivo* MRI to these modified 'en face-like' images. The error between the original and reconstructed MRI stack represents a measure of the *ex vivo*-to-en face registration accuracy. However, to what extent this simulated method approaches the real life situation remains a question [3]. In addition, the combined performance of all registration steps of the pipeline is difficult to simulate. We therefore chose the approach of measuring the overlap between the registered images [3] by calculating Haussdorff distances between the lumen segmentations in different imaging modalities. Theoretically, assuming idealized input and perfect registration, the optimal registration accuracy that can be achieved by the complete pipeline should be in the order of magnitude of the coarsest imaging resolution. Indeed, we found that the axial registration accuracy of our pipeline, as reported by Hausdorff distances, was in the order of magnitude of the *in vivo* MRI resolution. In addition, we found that a simulated mismatch of one *in vivo* MRI slice did not alter the WSS-plaque thickness correlation and concluded, somewhat pragmatically and to the best of our knowledge, that the accuracy of our registration pipeline is sufficient to serve the purpose it was designed for. It should be noted however, that excision, decalcification and histological processing of the advanced carotid plaques led to deformations and artefacts in the images that the applied registration method could not account for. Thus, loss of data was to some extent unavoidable. On a more general note, the current pipeline involves too much steps to be feasible for use in large clinical datasets. If that is the aim, the pipeline requires more automation, which would imply a redesign of the registration process and probably a discarding of the intermediate imaging steps in exchange for more accurate *in vivo* MRI sequences. With time, technological improvements might allow higher *in vivo* imaging resolutions with only limited increase in clinical scan time.
The insights that applying this pipeline provided on the correlation WSS-histology in advanced human carotid plaques are discussed in 7.2.

7.1.2 Data processing pipeline for correlation of spatial lipid patterns to plaque histology

Compared to the WSS-histology image registration pipeline, the registration of MALDI-MSI-based spatial lipid patterns to histology was fairly straightforward. Namely, since both imaging methods were applied on 2D tissue cross-sections, registration of the imaging outputs only required a point-based rigid registration of the MALDI-MSI tissue section and the tissue section used for histology

segmentation (original axial distance ~10 µm). However, in terms of data processing, handling of this large multidimensional dataset was challenging. The data processing can be subdivided in multiple steps: 1. Spectral processing, 2. Selection of tissue-specific, lipid *m/z* values and their identification, 3. Data compression and analysis, both unsupervised, i.e. histology-independent, and supervised, i.e. histology-based. Spectral processing of data is required for all mass spectrometry datasets, whether involving imaging or not, and has been studied extensively. This first processing step is necessary for removing all measurement-related variation and/or noise, that is not biologically relevant and involves baseline correction, normalization, calibration, smoothing and peak detection. The procedures have been thoroughly described in literature, also in the context of MALDI-MSI, e.g. in the reviews of Norris et al. and Alexandrov et al. [4,5]. We performed a reproducibility analysis to quantify the non-biological measurement variability of our experimental setup and spectral processing workflow. This was determined by calculating the coefficient of variation (CV) of each *m/z* value in our dataset. In the investigated dataset an average CV of 25% was found. However, the sections with lipid-rich plaques and little calcium-related tissue processing artefacts had an even lower CV for abundant lipids, i.e. 12-20%. Thus, for our population of lipid-rich advanced plaques, variations in lipid profile above this CV value are likely to be caused by individual, local or longitudinal biological variations. This is relevant information when applying unsupervised data analysis approaches, since these data mining techniques are able to visualize group structures, e.g. lipid profiles characteristic of plaque components only when variation within-groups, e.g. measurement variability, is sufficiently small [6,7]. Previously reported CV values using DHB matrix were in the order of magnitude of the average CV of our complete dataset [8,9], indicating that our sample preparation and spectral processing pipeline achieves good quality data.

The second data processing step in our pipeline, i.e. selection and identification of tissue-specific lipid *m/z* values, performed well. That is, visual assessment of the *m/z* values and images that were retained in the dataset after filtering, showed that the selected lipids were indeed tissue-specific. The lipid species measured were determined by the choice of matrix and ionization polarity mode, as discussed in Chapter 1. In this first study, we measured in positive ion mode in combination with DHB matrix. We made this choice because DHB was the most commonly applied and reported matrix for cardiovascular lipid research [10] and was shown to be effective for visualization of a wide array of lipids in positive ion mode. In future, the lipid map of human atheroma can be systematically extended with the spatial information of other lipid classes, by implementing the developed pipeline on a new dataset using negative ionization mode and/or an alternative matrix.

Based on literature reporting the measurements in both positive and negative

ionization mode in the same cardiovascular tissue samples, we expect to detect greater abundances of fatty acids [11,12], sphingomyelins [11] and phosphoinositols [11,13] in negative mode compared to positive mode.
In addition, specific lipids have been found to be differentially present in plasma samples of coronary artery disease (CAD) patients versus non-CAD patients [14] and specific lipids might thus be associated with the development of symptomatic disease. Targeted MS imaging of the presence and spatial localization of these lipids in advanced human plaques would also be very informative with respect to the identification of plaque vulnerability by plaque lipid content. This will be discussed further in 7.3.

As final data processing step, we applied both unsupervised and histology-based data analysis approaches to visualize lipid patterns in our set of advanced carotid plaques. Unsupervised methods do not require prior knowledge of the data: their application is aimed at visualizing general data structure and identify regions that display correlated mass spectral profiles [5,15]. A wide array of unsupervised classification algorithms have been proposed and tested on MSI data, as reported in excellent reviews [5,15,16]. On our dataset we have tested multiple algorithms, e.g. principal component analysis (PCA), non-negative matrix factorization (NMF) and K-means clustering. Small differences were found in the spectral patterns yielded by the different algorithms. However, by the application of three independent classification algorithms on the same dataset, we found data structures that were identified by all three classification methods. In accordance with literature [16,17], we found that the data reduction results of K-means and NMF were easier to interpret than those of the PCA. For application of K-means, the number of clusters needs to be predefined, which makes this method not truly unsupervised, and its random initialization led to different cluster results each time the algorithm was run. After careful consideration of the pros and cons per data analysis technique, we chose to apply NMF clustering on our dataset. NMF is an established data reduction approach for MSI data [16], the algorithm did not raise issues in terms of computational capacity and a model was available to calculate the optimal number of NMF components [18] before running the algorithm. We compared the outcome of the unsupervised NMF clustering with a multivariate analysis of histology-based data. We found that the methods agreed in the lipid profiles that were associated with the largest tissue structural features, i.e. necrotic core and fibrin. Histology is regarded as the gold standard in tissue characterization. Our comparison between the two analyses and the found agreements indicate that in future, assessment of large MSI datasets might be performed unsupervised, without the need of time- and labor-intensive histological processing. However, this would require additional comparative studies, to increase the body of evidence of overlap between histologically-determined compositional featu-

res and lipid profiles. In addition, the spatial lipid profile might complement the current views on plaque vulnerability characteristics, e.g the presence or absence of specific lipids might be correlated to a certain plaque phenotype or disease state. However, such features might be very subtle, and not easy to extract by the type of exploratory analyses that we performed here. Rather, large-scale targeted lipidomic profiling of plaque extracts could yield clues as to which lipid species should be selectively investigated.

7.2 WSS and histological characteristics of plaque vulnerability

7.2.1 Findings in a cross-sectional study of human advanced carotid atherosclerosis

The existence and/or nature of the relation between WSS and compositional characteristics of plaque vulnerability in advanced atherosclerosis has been, and still is, a subject of debate. The image registration framework presented in Chapter 2, provided a measure to investigate this relation in human advanced disease. We found larger NCs at sites of high TAWSS. Also, we found low OSI to correlate with larger macrophage area and thicker caps, surprising findings that have not been reported before. Namely, these low OSI areas, unlike the general assumption, not always coincided with high TAWSS, and the effect of low OSI alone on the regulation of endothelial signaling pathways has, to the best of knowledge, not been studied yet. The composition of the intimal areas that were located within a depth of 250 μm or 400 μm from the lumen, was not correlated to local WSS patterns.

Investigating disease in human subjects naturally involves methodological constraints. As we aimed to investigate the relation between WSS metrics and histologically-determined plaque composition, we were designated to a cross-sectional study setup, providing information about one time point. However, as described in Chapter 4, it is assumed that, to unravel the effect of WSS on plaque composition, dynamic changes in WSS levels should be monitored, i.e. by assessing WSS at multiple time points. Thus ideally, the relation between WSS and plaque composition should rather be investigated in a longitudinal setup. At the same time, it could be argued that if two factors are strongly related, evidence for this relation is also expected to crystallize in a cross-sectional study. We found relations between TAWSS and NC, which was in agreement with literature [19–21], and between OSI and macrophages and cap thickness. Caution should be taken with interpreting the found TAWSS-NC relation in this

cross-sectional setup. Namely, larger NCs are generally found in larger plaques and plaque size – partly - influences stenosis and subsequently WSS patterns, thus reflecting a chicken-and-egg problem that cannot be elucidated by studying one point in time. As for the relation of OSI with features of vulnerability, it would be interesting to extend this line of research, to find out whether OSI and TAWSS are independent metrics with respect to plaque vulnerability.

As plaque histology could only be obtained from subjects that were eligible for an endarterectomy procedure, the study population involved elderly patients with advanced disease. As argued above, relations between WSS and plaque composition might be dynamic and might be disease stage-dependent. Previously reported relations between TAWSS and vulnerability features, e.g. cap thickness or macrophage infiltration [22–24], might be less obvious in this elderly group of patients. In advanced disease, the complex interplay of multiple processes and factors, e.g. solid and fluid mechanics, molecular processes and/or lifestyle-related blood composition, might complicate the recognition of a one-on-one relation in this study setup.
In future applications of this pipeline, it might be interesting to replace our histology-based compositional measures, i.e. NC area, fibrin area, macrophage area and cap thickness, for compositional measures of vulnerability focused at the molecular level. For example by looking at inflammatory markers shown to be up- or downregulated in response to varying WSS levels [25]. The applied registration framework can be of value in these kind of studies as well, e.g. by adding immuno-histochemical staining procedures for specific molecular markers, by implementing other types of molecular imaging of tissue sections, e.g. MALDI-MSI or laser-capture micro dissection, into the pipeline.

7.2.2 Temporal and spatial developments in mice – translatable to the human situation?

To study the temporal changes in WSS distribution during plaque progression, a question that could not be answered by the cross-sectional human study presented in Chapter 2 and 3, a longitudinal study using an atherosclerotic mouse model was designed (Chapter 4). Atherosclerosis was induced in ApoE knockout mice by placing a flow-modifying tapered cast in the carotid artery. The interplay between disease progression, as measured by stenosis degree, and corresponding WSS distribution was monitored at three time points. Over time, animal-specific variations in disease progression were found, that were uncorrelated to the degree of stenosis at the start and end points of the study. Also, blood flow through the diseased arteries dramatically reduced over time in almost all animals. This led to the counterintuitive observation of progressi-

ve lumen narrowing that was accompanied by decreasing absolute WSS levels over time. The notable conclusion of this study is the importance of taking into account both geometrical and flow information when studying WSS patterns, while many studies only look at geometry to make WSS assumptions. Whether the observed reduction in blood flow and concomitant decrease in WSS over time was inherent to this specific mouse model or a general pathological phenomenon, as it is related to the status of the distal vascular bed, is unclear. Previously-performed longitudinal studies in mice insufficiently report temporal and spatial changes in WSS during disease progression. In a recent longitudinal study in pig coronary arteries, flow levels did not markedly change over time and the largest plaque progression was found in segments with low initial TAWSS that over time developed into high TAWSS [26]. Though this study differed both in investigated vascular bed and in animal model, the results indicate that the observed dramatic decrease in flow and WSS over time in our study might be inherent to the mouse-cast model. Also, in human carotid arteries, WSS was mainly reported to increase over time [19,27,28].

Considering plaque growth, the plaque gradually developed upstream of the surgically-induced stenosis and axially progressed from distal to proximal over time. At each time point, the averaged WSS levels in the proximally-located healthy artery segment were lower than in the diseased segment, resulting in a positive correlation between TAWSS and plaque size. At the final time point, the correlation between histologically-determined plaque composition and WSS levels at the three imaging time points was investigated as well. Eccentric plaques with relatively large macrophage areas were found proximally, whereas closer to the cast larger concentric plaques with lower degrees of macrophage infiltration were found. Thus, an inverse correlation between TAWSS and macrophage area was shown in almost all animals. In addition, a trend towards higher relative NC area at higher TAWSS was seen, as in the human CEAs in Chapter 3. However, direct translation of these results to plaque composition and WSS found in humans, is difficult. In general, atherosclerosis in mice is associated with more inflammation than in humans [29], which might explain the relation between TAWSS and macrophages observed in the mouse model, but not in the human CEAs. Secondly, the biomechanical environment in mice is completely different, e.g. the Reynold's number differs [30], which directly influences WSS levels, and mouse vasculature experiences much lower stress compared to humans [31]. Since other biomechanical factors were not taken into account, their influence on plaque composition in both studies further hampers direct translation. While in the human CEA study, the use of patient-specific WSS tertiles was advocated above the use of absolute WSS values, in Chapter 4 animal-specific analysis of correlations was performed using absolute TAWSS values.

In the mouse study, the analysis could be performed using absolute TAWSS values because the ranges of TAWSS values were less wide, i.e. in the order of 0-10 Pa, than in the human carotids.

7.2.3 Potency of WSS as biomarker or correlative factor reflecting pathophysiology

What insights were gained from the combination of the cross-sectional human study and the longitudinal mouse model and how to proceed investigations in order to ultimately benefit clinical practice? Firstly, both studies point out that WSS is a factor that strongly depends on subject-specific geometry and flow conditions. Thus, general cut-off values, discriminating low, mid and high WSS, should not be aimed at. In addition, when including WSS at multiple time points, alterations in flow through the artery should also be assessed and taken into account. Secondly, though the found relations between local WSS and plaque composition varied, both studies stressed the spatial compositional heterogeneity of the plaque. This implies that future investigations should aim at achieving accurate co-localization of WSS and compositional information and limiting the degree of spatial averaging of WSS.
Considering these two main insights from Chapter 3 and 4, and focusing on human carotid atherosclerosis, performing an MRI-based longitudinal study into the WSS-plaque vulnerability relation will be an interesting direction to head into. Presuming that in the near future MRI technology will fulfill its potential of achieving very high spatial resolution [32,33], this technique will allow sequential scanning of plaques, thereby unraveling the dynamic compositional effects of disease progression over time. Also, as MRI sequences for direct WSS assessment are improving 18, WSS and plaque composition can be derived from the same imaging modality, thereby undoing all current limitations of studies involving multiple imaging modalities. An important question that remains however, is what timeline should be considered to capture the dynamic effect of WSS on plaque composition in humans? In the mouse-cast model, WSS at 4 and 2 weeks before histological assessment and at the time of sacrifice was monitored, but these numbers are difficult to translate to the human situation, as disease rate differs between mice and man. In the largest longitudinal cohort of coronary artery patients, mean follow-up time, determined by the occurrence of clinical events, was 3.4 years [34]. So when investigating advanced disease in a population comparable in age to the CEA population, we should consider designing a 4 year longitudinal study with yearly imaging time points to monitor the dynamic interplay of WSS and plaque composition.

7.3 Lipid patterns and histological characteristics of plaque vulnerability

7.3.1 Potency of spatial lipid signal as biomarker for plaque compositional characteristics

Chapter 6 describes a unique study, in which the spatial locations of almost 200 lipids in human CEA samples are compared and correlated to the local histologically-determined plaque composition in order to find lipid species indicative of plaque phenotype. We were the first to perform this analysis on a set of over 100 tissue sections, thereby gaining a wealth of information on both the inter- and intra-plaque variability in spatial lipid composition. As mentioned in 7.1, the choice of DHB matrix and positive polarity allowed for the visualization of an array of lipid classes that were recognized to play a role in atherosclerosis in earlier work [11,35].
Generally, lipids belonging to the same lipid class showed similar spatial patterns. Between lipid classes however, marked differences in distribution were observed. SMs and oxidized CEs, two lipid types that have been associated with plaque development before [35–40], were found to be significantly more abundant in NC. In addition, DAGs and TAGs were found in higher concentrations in regions histologically associated with thrombus. These results are promising, as they indicate a relation between specific lipids and vulnerability features.

Most studies investigating the lipid content of human atherosclerotic plaques have used CEA samples, as it is the most easily obtainable human plaque material. However, the composition of these tissue samples represents advanced, often symptomatic, disease. For extending our understanding of the role and significance of lipids in atherosclerosis, there is need for comparison of lipid profiles at different disease stages, as well as in stable versus unstable disease. In early studies, different disease stages have been characterized by varying relative ratios of lipid classes. That is, with plaque progression, the ratio esterified cholesterol to total cholesterol was found to decrease, while the ratio sphingomyelin to phosphocholine increased [41–43]. Since atherosclerosis is characterized by accumulation and local oxidation of lipids in the growing plaque, the degree and nature of oxidation products has also been compared between plaque stages [44]. Disease progression was expected to be accompanied by increasing levels of oxidized phospholipid species, and the most advanced plaques were expected to show the most stable oxidation products. However, this pattern was not found in a study comparing oxidation products of the major phospholipids in different plaque stages [44], indicating that atherosclerosis involves

a continuous process of lipid infiltration and peroxidation and that both formation and degradation of early and advanced products of lipid oxidation are present in each plaque stage. In a study comparing spatial lipid distributions in human coronary plaque cross-sections, the spatial distribution of lipid classes was reported to differ depending on histologically-defined plaque stage [11].

For studying stable versus unstable atherosclerosis, studies have focused on the lipid composition of blood plasma instead of plaque. As mentioned in 7.1.2, in large cohorts of CAD patients, specific phospholipids and sphingolipids have been associated with cardiovascular events [45–47] and can improve event risk prediction scores. Also, levels of distinct ceramide, phosphatidylinositol and phosphatidylethynolamine species were able to discern stable from unstable CAD [14]. As relations have been suggested between plasma lipids and the condition of the vascular wall [48], it will be interesting to specifically image the spatial distribution of these reported lipid species in different plaque stages, to find out whether these lipid molecules are associated with features of plaque vulnerability.

All in all, there is substantial evidence for a relation between plaque vulnerability and lipid profile, to which our MALDI-MSI study has significantly contributed. The finding that specific lipids are more abundant in NC or thrombus is crucially informative for the development of new imaging techniques. Spectral photoacoustics (sPA), an imaging modality that can reveal lipid composition based on optical absorption, is a very suitable technique for imaging a plaque's lipid profile. Using sPA, our findings can be translated to a clinical application able to improve assessment of a plaque's rupture risk and treatment plan.

References

1. Maintz, J. B. A. & Viergever, M. A. A survey of medical image registration. ***Med. Image Anal.*** **2**, 1–36 (1998).
2. Pichat, J., Iglesias, J. E., Yousry, T., Ourselin, S. & Modat, M. A Survey of Methods for 3D Histology Reconstruction. ***Med Image Anal*** **46**, 73–105 (2018).
3. Murphy, K. ***et al.*** Semi-automatic construction of reference standards for evaluation of image registration. ***Med. Image Anal.*** **15**, 71–84 (2011).
4. Norris, J. L. ***et al.*** Processing MALDI mass spectra to improve mass spectral direct tissue analysis. ***Int. J. Mass Spectrom.*** **260**, 212–221 (2007).
5. Alexandrov, T. MALDI imaging mass spectrometry: statistical data analysis and current computational challenges. ***BMC bioinformatics*** vol. 13 Suppl 1 S11 (2012).
6. Manier, S. K., Keller, A. & Meyer, M. R. Automated optimization of XCMS parameters for improved peak picking of liquid chromatography–mass spectrometry data using the coefficient of variation and parameter sweeping for untargeted metabolomics. ***Drug Test. Anal.*** **11**, 752–761 (2019).
7. Worley, B. & Powers, R. Multivariate Analysis in Metabolomics. ***Curr. Metabolomics*** **1**, 92–107 (2013).
8. Wang, Z. ***et al.*** Improved MALDI imaging MS analysis of phospholipids using graphene oxide as new matrix. ***Sci. Rep.*** **7**, (2017).
9. Zhu, Z. ***et al.*** An auxiliary matrix for routine analysis of small molecules and biological macromolecules using matrix-assisted laser desorption ionization mass spectrometry. ***Anal. Bioanal. Chem.*** **411**, 1041–1052 (2019).
10. Mezger, S. T. P., Mingels, A. M. A., Bekers, O., Cillero-Pastor, B. & Heeren, R. M. A. Trends in mass spectrometry imaging for cardiovascular diseases. ***Anal Bioanal Chem*** **411**, 3709–3720 (2019).
11. Lehti, S. ***et al.*** Spatial distributions of lipids in atherosclerosis of human coronary arteries studied by time-of-flight secondary ion mass spectrometry. ***Am. J. Pathol.*** **185**, 1216–1233 (2015).
12. Malmberg, P. ***et al.*** Localization of lipids in the aortic wall with imaging TOF-SIMS. ***Biochim. Biophys. Acta - Mol. Cell Biol. Lipids*** **1771**, 185–195 (2007).
13. Meisenbichler, C., Doppler, C., Bernhard, D. & Müller, T. Improved matrix coating for positive- and negative-ion-mode MALDI-TOF imaging of lipids in blood vessel tissues. ***Anal. Bioanal. Chem.*** **411**, 3221–3227 (2019).
14. Meikle, P. J. ***et al.*** Plasma lipidomic analysis of stable and unstable coronary artery disease. ***Arterioscler. Thromb. Vasc. Biol.*** **31**, 2723–2732 (2011).
15. Jones, E. A., Van Remoortere, A., Van Zeijl, R. J. M., Hogendoorn, P. C. W. & Bovée, J. Multiple Statistical Analysis Techniques Corroborate Intratumor Heterogeneity in Imaging Mass Spectrometry Datasets of Myxofibrosarcoma. ***PLoS One*** **6**, 24913 (2011).
16. Verbeeck, N., Caprioli, R. M. & Van de Plas, R. Unsupervised machine learning for exploratory data analysis in imaging mass spectrometry. ***Mass Spectrom. Rev.*** **n/a**, 245–291 (2020).
17. Siy, P. W. ***et al.*** Matrix factorization techniques for analysis of imaging mass spectrometry data. in ***8th IEEE International Conference on BioInformatics and BioEngineering, BIBE 2008*** vol. 2008 (NIH Public Access, 2008).
18. Kim, H. & Park, H. Sparse non-negative matrix factorizations via alternating non-negativity-constrained least squares for microarray data analysis. ***Bioinformatics*** **23**, 1495–1502 (2007).
19. Yang, C. ***et al.*** Advanced human carotid plaque progression correlates positively with flow shear stress using follow-up scan data: an in vivo MRI multi-patient 3D FSI study. ***J Biomech*** **43**, 2530–2538 (2010).
20. Samady, H. ***et al.*** Coronary artery wall shear stress is associated with progression and transformation of atherosclerotic plaque and arterial remodeling in patients with coronary artery disease. ***Circulation*** **124**, 779–788 (2011).
21. Park, J. B. ***et al.*** Computational fluid dynamic measures of wall shear stress are related to coronary lesion characteristics. ***Heart*** **102**, 1655–1661 (2016).
22. Wentzel, J. J. ***et al.*** In vivo assessment of the relationship between shear stress and necrotic core in early and advanced coronary artery disease. ***EuroIntervention*** **9**, 989–995 (2013).
23. Dirksen, M. T., van der Wal, A. C., van den Berg, F. M., van der Loos, C. M. & Becker, A. E. Distribution of inflammatory cells in atherosclerotic plaques relates to the direction of flow. ***Circulation*** **98**, 2000–2003 (1998).
24. Fagerberg, B. ***et al.*** Differences in Lesion Severity and Cellular Composition between in vivo Assessed Upstream and Downstream Sides of Human Symptomatic Carotid Atherosclerotic Plaques. ***J. Vasc. Res.*** **47**, 221–230 (2010).

25. Baeyens, N., Bandyopadhyay, C., Coon, B. G., Yun, S. & Schwartz, M. A. Endothelial fluid shear stress sensing in vascular health and disease. ***Journal of Clinical Investigation*** vol. 126 821–828 (2016).
26. Hoogendoorn, A. ***et al.*** Multidirectional wall shear stress promotes advanced coronary plaque development: comparing five shear stress metrics. doi:10.1093/cvr/cvz212.
27. Filipovic, N. ***et al.*** Computer simulation of three-dimensional plaque formation and progression in the carotid artery. ***Med. Biol. Eng. Comput.*** **51**, 607–616 (2013).
28. Sakellarios, A. I. ***et al.*** Natural History of Carotid Atherosclerosis in Relation to the Hemodynamic Environment. ***Angiology*** **68**, 109–118 (2017).
29. Falk, E. Pathogenesis of Atherosclerosis. ***J. Am. Coll. Cardiol.*** **47**, 0–5 (2006).
30. Suo, J. ***et al.*** Hemodynamic shear stresses in mouse aortas: Implications for atherogenesis. ***Arterioscler. Thromb. Vasc. Biol.*** **27**, 346–351 (2007).
31. Bond, A. R. & Jackson, C. L. The Fat-Fed Apolipoprotein E Knockout Mouse Brachiocephalic Artery in the Study of Atherosclerotic Plaque Rupture. ***J. Biomed. Biotechnol.*** **2011**, (2011).
32. Peper, E. S. ***et al.*** Highly accelerated 4D flow cardiovascular magnetic resonance using a pseudo-spiral Cartesian acquisition and compressed sensing reconstruction for carotid flow and wall shear stress. ***J. Cardiovasc. Magn. Reson.*** **22**, (2020).
33. Zhang, Q. ***et al.*** Comparison of four MR carotid surface coils at 3T. ***PLoS One*** **14**, (2019).
34. Stone, P. H. ***et al.*** Role of Low Endothelial Shear Stress and Plaque Characteristics in the Prediction of Nonculprit Major Adverse Cardiac Events: The PROSPECT Study. ***JACC Cardiovasc Imaging*** **11**, 462–471 (2018).
35. Stegemann, C. ***et al.*** Comparative lipidomics profiling of human atherosclerotic plaques. ***Circ. Cardiovasc. Genet.*** **4**, 232–242 (2011).
36. Hutchins, P. M., Moore, E. E. & Murphy, R. C. Electrospray MS/MS reveals extensive and nonspecific oxidation of cholesterol esters in human peripheral vascular lesions. ***J. Lipid Res.*** **52**, 2070–2083 (2011).
37. Manicke, N. E., Wiseman, J. M., Ifa, D. R. & Cooks, R. G. Desorption Electrospray Ionization (DESI) Mass Spectrometry and Tandem Mass Spectrometry (MS/MS) of Phospholipids and Sphingolipids: Ionization, Adduct Formation, and Fragmentation. ***J. Am. Soc. Mass Spectrom.*** **19**, 531–543 (2008).
38. Upston, J. M. ***et al.*** Disease stage-dependent accumulation of lipid and protein oxidation products in human atherosclerosis. ***Am J Pathol*** **160**, 701–710 (2002).
39. Suarna, C., Dean, R. T., May, J. & Stocker, R. Human atherosclerotic plaque contains both oxidized lipids and relatively large amounts of alpha-tocopherol and ascorbate. ***Arter. Thromb Vasc Biol*** **15**, 1616–1624 (1995).
40. Brown, A. J., Leong, S. L., Dean, R. T. & Jessup, W. 7-Hydroperoxycholesterol and its products in oxidized low density lipoprotein and human atherosclerotic plaque. ***J Lipid Res*** **38**, 1730–1745 (1997).
41. Smith, E. B., Slater, R. S. & Chu, P. K. The lipids in raised fatty and fibrous lesions in human aorta. A comparison of the changes at different stages of development. ***J. Atheroscler. Res.*** **8**, 399–419 (1968).
42. Katz, S. S., Shipley, G. G. & Small, D. M. Physical chemistry of the lipids of human atherosclerotic lesions. Demonstration of a lesion intermediate between fatty streaks and advanced plaques. ***J. Clin. Invest.*** **58**, 200–211 (1976).
43. Lundberg, B. Chemical composition and physical state of lipid deposits in atherosclerosis. ***Atherosclerosis*** **56**, 93–110 (1985).
44. Ravandi, A. ***et al.*** Phospholipids and oxophospholipids in atherosclerotic plaques at different stages of plaque development. ***Lipids*** **39**, 97–109 (2004).
45. Hilvo, M. ***et al.*** Development and validation of a ceramide- and phospholipid-based cardiovascular risk estimation score for coronary artery disease patients. ***Eur Hear. J*** **41**, 371–380 (2020).
46. Alshehry, Z. H. ***et al.*** Plasma Lipidomic Profiles Improve on Traditional Risk Factors for the Prediction of Cardiovascular Events in Type 2 Diabetes Mellitus. ***Circulation*** **134**, 1637–1650 (2016).
47. Cheng, J. M. ***et al.*** Plasma concentrations of molecular lipid species in relation to coronary plaque characteristics and cardiovascular outcome: Results of the ATHEROREMO-IVUS study. ***Atherosclerosis*** **243**, 560–566 (2015).
48. Didangelos, A., Stegemann, C. & Mayr, M. The -omics era: Proteomics and lipidomics in vascular research. ***Atherosclerosis*** **221**, 12–17 (2012).

Summary

Cerebrovascular events such as stroke can inflict sudden death or disability: either way they have a significant impact on personal lives as well as on society. One of the underlying diseases leading to cerebrovascular events is carotid atherosclerosis. Decades of research have been devoted to unravelling the pathophysiology of this disease, however the developments that lead to plaque rupture and clinical symptoms are still not fully elucidated. Thorough understanding of the pathophysiology of atherosclerosis is important for disease management, e.g. prevention and therapy, as well as for early diagnosis of the patient at risk of an event. The work described in this thesis focused on advanced carotid atherosclerotic plaques and aimed at investigating two characteristics of plaque pathology that might be indicative of the vulnerability of the plaque. These two characteristics are 1. the distributed wall shear stress (WSS) patterns over the plaque and 2. the spatial distribution of lipids in the plaque. Both are compared to local tissue compositional characteristics of plaque vulnerability identified by histology, which is the current golden standard to obtain compositional information. To achieve these goals we developed two image registration and data processing pipelines, that were applied on datasets of human carotid endarterectomy samples. This thesis is subdivided in two parts: In Part 1 the work aimed at investigating the correlation between local WSS patterns and histologically-determined tissue composition is described and in Part 2 histologically-determined plaque composition is correlated to spatial lipid patterns.

In **Chapter 1** we provide the biological background of atherosclerosis. We explain the influence of hemodynamics on disease initiation and shortly review the current knowledge on the role of WSS in carotid atherosclerosis progression. We explain that lipids play a crucial role in the pathophysiology of atherosclerosis and might be indicative of plaque phenotype, which is why they embody a potential powerful diagnostic imaging marker.

To correlate local WSS levels directly to plaque compositional information derived from histology we developed an image registration pipeline, which is described in **Chapter 2**. The pipeline was designed to process imaging and histology data of carotid endarterectomy specimens. Four types of images of the plaque were required as input: *in vivo* carotid MRI before surgery, *ex vivo* MRI of the excised plaque, en face photos of 1 mm thick axial cross-sections of the plaque, as well as the corresponding histology images of these axial cross-sections. By a series of rigid and non-rigid registration steps, these images were mapped to a shared 3D image domain. 3D WSS maps were generated based on

the MRI-derived *in vivo* artery geometry and patient-specific flow information. After successful registration, the axially-averaged WSS values were mapped in 2D on the corresponding lumen locations of the histology sections. As a validation measure, we simulated the effect of an axial mismatch of one MRI slice on the relation between WSS and plaque thickness, and found that this relation was not significantly altered in the investigated cases.

The developed image registration pipeline was applied on a dataset of human carotid endarterectomy samples. The results of this study are described in **Chapter 3**. We correlated local time-averaged WSS (TAWSS) and oscillatory shear index (OSI) values to plaque composition. Significantly larger NC areas were found at arterial segments exposed to high TAWSS. In addition, segments exposed to low OSI values had significantly more macrophages and a trend towards higher cap thickness at low OSI was observed.

In **Chapter 4** we described the temporal and spatial changes in WSS in an ApoE knockout mouse model of carotid atherosclerosis. Absolute WSS was found to significantly decrease with time, while the degree of stenosis increased. In addition, we investigated the relation between local WSS and histological plaque composition and found a positive correlation between WSS and plaque area and a negative correlation between WSS and macrophage content. Pooling the data of all animals nullified these correlations, demonstrating that analysis of individual cases is necessary for investigating WSS-plaque composition correlations.

Part 2 of this thesis starts with **Chapter 5**, which describes a data processing pipeline to investigate the spatial lipid patterns in carotid endarterectomy samples using matrix-assisted laser desorption/ionization mass spectrometry imaging (MALDI-MSI). This pipeline was developed as a tool to investigate whether the spatial lipid profile of a plaque is indicative of plaque phenotype. We optimized sample preparation, data processing and data filtering to obtain a reproducible workflow for visualizing lipid distributions in carotid tissue sections and to contextualize these findings in terms of histology. In a series of tissue sections, we found that diacylglycerols were more abundant in a thrombotic area. Also, we found that the ratio of cholesteryl ester (CE) oleate and CE linoleate was indicative of plaque phenotype.

In **Chapter 6**, the pipeline developed in **Chapter 5** was applied on a dataset of human carotid endarterectomy samples. The resulting data, containing both spectral and spatial information, was analyzed by unsupervised classification as well as by an histology-driven multivariate approach. Both methods identi-

fied an increased abundance of sphingomyelins and oxidized cholesteryl esters in necrotic plaque areas. In addition, diacylglycerols and triacylglycerols were associated with areas containing fibrin, a structural component of thrombus.

Finally, in **Chapter 7** the main technological developments and biological findings of this thesis are discussed, as well as their contribution to the cardiovascular research field.

Samenvatting

Een herseninfarct kan resulteren in ingrijpende lichamelijke beperkingen of in een plotseling overlijden. Beide scenario's hebben een aanzienlijke impact op persoonlijke levens en op de maatschappij. Atherosclerose is één van de onderliggende oorzaken van een herseninfarct. Al decennia lang proberen wetenschappers de pathofysiologie van deze ziekte te ontrafelen, maar de ontwikkelingen die leiden tot plaque-ruptuur en klinische symptomen zijn nog steeds niet volledig in kaart gebracht. Een grondig begrip van de pathofysiologie van atherosclerose is belangrijk voor ziektebeheer, middels preventie en therapie, en ten behoeve van een tijdige diagnose van een patiënt met risico op een herseninfarct. Het werk dat in dit proefschrift wordt beschreven, was gericht op vergevorderde plaque vorming in de halsslagader (arteria carotis) en op het onderzoeken van twee kenmerken van plaque pathologie die een aanwijzing kunnen zijn voor de ruptuurgevoeligheid van een plaque. Deze twee kenmerken zijn 1. De verdeling van de wandschuifspanning (WSS) over een plaque en 2. de spatiële verdeling van lipiden in een plaque. Beide kenmerken worden afgezet tegen lokale plaque componenten die eerder gecorreleerd zijn aan de ruptuurgevoeligheid van een plaque. Deze componenten worden zichtbaar gemaakt middels histologie, de huidige gouden standaard om plaque compositie in kaart te brengen. Om dit te kunnen doen, ontwikkelden we twee beeldregistratie- en data verwerkings-methoden, die werden toegepast op datasets van humane carotis-endarteriëctomie specimens. Dit proefschrift is onderverdeeld in twee delen: in deel 1 wordt het werk beschreven dat gericht is op het onderzoeken van de correlatie tussen lokale WSS-patronen en histologisch bepaalde plaque compositie en in deel 2 het werk dat gericht is op het onderzoeken van de correlatie tussen spatiële lipidenpatronen en histologisch bepaalde plaque compositie.

In **Hoofdstuk 1** wordt de biologische ontwikkeling van een atherosclerotische plaque beschreven. De invloed van hemodynamica op het ontstaan van een plaque en de huidige kennis met betrekking tot de rol van WSS op de progressie van een atherosclerotische plaque in de arteria carotis wordt uitgelegd. De cruciale rol die lipiden spelen in de pathofysiologie van atherosclerose wordt beschreven. Spatiële lipidenpatronen in een plaque zijn mogelijk indicatief voor de ruptuurgevoeligheid van een plaque en zouden daarom kunnen dienen als diagnostische marker.

Om lokale WSS-niveaus direct te correleren aan weefselsamenstelling van de plaque, verkregen middels histologie, ontwikkelden we een beeldregistratie

methode.

Deze wordt beschreven in **Hoofdstuk 2**. De methode is ontworpen om beeldvormings- en histologie-data van carotis-endarteriëctomie-specimens te verwerken. Vier soorten afbeeldingen van de plaque waren nodig als input: *in vivo* carotis-MRI vóór de operatie, *ex vivo* MRI van de chirurgisch uitgenomen plaque, foto's van 1 mm dikke axiale doorsneden van de plaque, evenals foto's van de 5 µm dikke histologische coupes verkregen van deze axiale doorsneden. Door een reeks rigide en niet-rigide registratiestappen werden deze afbeeldingen weergegeven op een gedeeld 3D-beelddomein. De WSS verdeling over de carotis werd berekend op basis van de *in vivo* geometrie verkregen met MRI en patiënt-specifieke bloedstroomsnelheid. Na succesvolle registratie werden de axiaal gemiddelde WSS-waarden in 2D weergegeven op de bijbehorende lumen locaties in de histologische coupes. Ter validatie simuleerden we het effect van een axiale mismatch ter grootte van één MRI cross-sectie op de relatie tussen WSS en plaque dikte, en ontdekten dat deze relatie in de onderzochte gevallen niet significant veranderde.

De ontwikkelde beeldregistratie methode werd toegepast op een dataset van humane carotis-endarteriëctomie-specimens. De resultaten van deze studie worden beschreven in **Hoofdstuk 3**. We correleerden de lokale, over de tijd gemiddelde WSS-waarden (TAWSS) en de oscillatoire shear index (OSI) aan plaque compositie. Significant grotere necrotische plaque gebieden werden gevonden bij arteriële segmenten die waren blootgesteld aan hoge TAWSS. Bovendien hadden segmenten die waren blootgesteld aan lage OSI waarden significant meer macrofagen en werd een trend waargenomen naar een hogere kapdikte bij lage OSI.

In **Hoofdstuk 4** beschreven we de temporele en spatiële veranderingen in WSS in een muismodel van carotis atherosclerose ($ApoE^{-/-}$ met cast). Absolute WSS bleek significant af te nemen met plaque progressie, terwijl de mate van stenose juist toenam. Daarnaast onderzochten we de relatie tussen lokale WSS en histologisch-bepaalde plaque compositie en vonden we een significante positieve correlatie tussen WSS en plaque grootte en een significant negatieve correlatie tussen WSS en macrofaagdichtheid. Het middelen van de data van alle dieren maakte deze correlaties ongedaan, wat aantoont dat analyse van individuele gevallen noodzakelijk is voor het onderzoeken van correlaties tussen WSS en plaque compositie.

Deel 2 van dit proefschrift begint met **Hoofdstuk 5**, dat een data-verwerkings methode beschrijft om de spatiële lipidenpatronen in carotis endarteriëctomie

specimens te onderzoeken met behulp van matrix-geassisteerde laserdesorptie / ionisatie massaspectrometrie beeldvorming. Deze methode is ontwikkeld om te onderzoeken of het spatiële lipidenpatroon van een plaque indicatief is voor de ruptuurgevoeligheid van een plaque. We hebben de weefsel preparatie, data verwerking en data filtering geoptimaliseerd om een reproduceerbaar werkprotocol te verkrijgen voor het visualiseren van spatiële lipidenpatronen in coupes van humane carotis plaques en om deze bevindingen te relateren aan histologie. In een reeks weefselcoupes ontdekten we dat diacylglycerolen meer voorkwamen in gebieden met bloedingen. Daarnaast vonden we dat de verhouding van cholesterylester oleaat en cholesteryl ester linoleaat indicatief was voor de mate van ruptuurgevoeligheid van een plaque.

In **Hoofdstuk 6** werd de in **Hoofdstuk 5** ontwikkelde methode toegepast op een dataset van humane carotis endarteriëctomie specimens. De resulterende datasets, die zowel spectrale als spatiële informatie bevatten, werden geanalyseerd met een histologie-onafhankelijk classificatie algoritme en een door histologie aangestuurde multivariate benadering. Beide methoden identificeerden een hogere hoeveelheid sphingomyelines en geoxideerde cholesteryl esters in necrotische delen van de plaque. Bovendien werden diacylglycerolen en triacylglycerolen geassocieerd met gebieden die fibrine bevatten, een structureel onderdeel van trombus.

Tot slot worden in **Hoofdstuk 7** de belangrijkste technologische ontwikkelingen en biologische bevindingen van dit proefschrift besproken, evenals hun bijdrage aan het cardiovasculaire onderzoeksveld.

PhD Portfolio

General Courses	Year	ECTS
Research integrity	2018	0.3
Workshop Photoshop and Illustrator	2016	0.3
Systematic literature search course (Medical Library)	2016	1.5
Biomedical writing course	2017	3.0
Employability outside academia (PCDI)	2019	1.5
Scientific courses		
Vascular Biology (Dutch Heart Foundation)	2015	3.0
Cardiovascular Medicine (COEUR)	2015	1.5
Sex and Gender differences in Cardiovascular research (COEUR)	2018	1.5
Translational imaging workshop (MolMed)	2017	1.4
Scientific seminars (Erasmus MC)		
Symposium Sex and Gender differences in metabolism (COEUR)	2015	0.2
Symposium Translational research (COEUR)	2016	0.2
PhD days (COEUR)	2016-2018	0.9
Symposium Biomechanics in Cardiovascular Disease (COEUR)	2019	0.1
BME departmental research lectures (4 presentations)	2015-2019	0.8
Scientific seminars (other)		
ICIN theme meeting Vascular Medicine	2015	0.3
Young@Heart day	2017	0.3
Dutch Society for Mass Spectrometry Fall meeting	2019	0.3
Other healthcare events		
CHAMELEON event	2018	0.3

Innovation for Health	2019, 2020	0.6
Puls, Hartstichting	2016	0.3
National and international conferences		
Cardiovascular Conference, Ede	2016	0.3
Dutch Biomedical Engineering Conference, Egmond aan Zee (presentation)	2017	1.6
Ourcon Mass Spectrometry Imaging Conference, Doorn (poster)	2017	1.7
NAVBO Vascular Biology Conference, Monterey, USA (presentation + poster)	2017	2.7
Dutch Biomedical Engineering Conference, Egmond aan Zee (poster)	2019	1.1
Biomechanics in Vascular Biology and Cardiovascular Disease symposium, Rotterdam (poster)	2017	1.1
Biomechanics in Vascular Biology and Cardiovascular Disease symposium, London (poster)	2019	1.1
Dutch Society for Mass Spectrometry Conference, Kerkrade (presentation)	2019	1.9
Supervision of students		
Supervision of medical students writing systematic literature review	2017	0.2
Supervision of HLO student (6 months)	2017	1.0
Other activities		
Organization of lab-day-out	2017	0.1
Total		**31.1**

About the author

Astrid Maria Moerman was born on January 10th, 1990 and grew up in Maassluis, The Netherlands. She went to secondary school in Schiedam at the Stedelijk Gymnasium and graduated in 2008. That same year, she started her Bachelor's study in Biomedical Sciences at Leiden University, which she completed in 2011. For her Master's degree, Astrid moved to Delft. Here she followed a premaster program Mechanical Engineering and a Master's study Biomedical Engineering (2015) at TU Delft. Her master thesis focused on the mechanical and biological characterization of tissue surrounding hip implants. In 2015, Astrid became a PhD candidate at the Biomedical Engineering department of Erasmus MC in Rotterdam. She investigated the relation between atherosclerotic plaque composition and local shear stress in carotid arteries. Also she investigated the spatial lipid profile of carotid atherosclerotic plaques and its relation to plaque vulnerability. This resulted in her PhD defense at November 4th 2020.

Dankwoord

Het moge duidelijk zijn dat ik het werk beschreven in dit boek niet in mijn eentje heb gedaan. Daarom wil ik in dit hoofdstuk graag wat mensen bedanken.

Allereerst copromotoren **Kim** en **Frank**, dankjewel! Kim, zonder jou had ik natuurlijk helemaal geen project gehad om me 4+ jaar mee bezig te houden. Het was een uitdagend plan, waar een stuk meer bij kwam kijken dan jij, bij het schrijven van het voorstel, en ik, bij het ja zeggen tegen deze functie, hadden voorzien. Ik heb de afgelopen jaren enorm veel van je geleerd. Het voornaamste dat ik mee zal nemen is op het juiste moment kritische vragen stellen, het overtuigend neerzetten van een verhaal en het managen van een groot project en alle mensen die daarbij komen kijken. Naast project-gerelateerde vragen kon ik bij je terecht voor adviezen over van alles: van carrière-tips tot ervaringen in baby- en gezinsmanagement. Je bent een supertoegankelijk persoon, iets wat ik erg waardeer. En samen met Frank vormde je een zeer vermakelijk duo om op dinsdagochtend de stand van zaken mee door te spreken. Gelukkig zorgen jullie met z'n tweeën beter voor jullie promovendi dan voor jullie planten ;) En dat brengt me bij Frank: dankjewel voor alle momenten dat ik toch éventjes bij je kon langslopen voor vragen over Simpele Modelletjes. Ik heb genoten van het enthousiasme waarmee je kan praten over CFD, je soms behoorlijk ongezouten mening en je onuitputtelijke geheugen voor wie – wat - wanneer – en in welk blad - heeft gepubliceerd. Ik heb bovendien heel veel geleerd van jouw manier van redereneren en natuurlijk van je presentatie-skills.

Dan mijn promotor **Ton**, bedankt dat ik dit werk mocht verrichten op jouw afdeling en bedankt voor de goede adviezen in de afrondingsfase van mijn PhD. I would like to thank the other **doctoral committee members** for assessing the content of my work and preparing an (hopefully) lively discussion.

Mirjam, mijn mede-manager van de MALDI-MSI imaging facility Rotterdam. Het was de afgelopen vier jaar soms samen lachen, samen huilen, maar ik heb me geen betere partner in crime kunnen wensen. Over mijn eerste paranimf heb ik dus ook niet lang na hoeven denken. In sommige opzichten waren we tegenpolen (ik met mijn liefde voor woorden, jij voor getallen, om maar iets te noemen), maar daarin hebben we elkaar denk ik goed aangevuld. Je rechtdoor-zee mentaliteit is iets waar ik veel van geleerd heb: volgens mij word je in elk dankwoord geroemd om je eerlijkheid en dat beaam ik helemaal. Als je mijn kantoor binnenkwam met de woorden 'ik heb toch nog éven naar

de data gekeken …' dan wist ik dat er weer een compleet nieuwe invalshoek ging komen. Dank voor je monster-Excel tabellen, je doorzettingsvermogen en boven alles bedankt voor je gezelligheid! Ik wens je het allerbeste met de afronding van je PhD en alles daarna en ik hoop natuurlijk dat je mij en mijn notitieboekjes in de toekomst een beetje gaat missen.

Eline, dankjewel dat je gewoon een superleuke collega bent! Je brengt een hoop kleur in de groep en kan me het pre-Eline tijdperk eigenlijk helemaal niet meer herinneren. Daarnaast heb ik veel geleerd van jouw manier van problemen benoemen en oplossen. Dank voor de onzinnige en soms iets minder onzinnige gesprekken en dank voor het uitlaten van mij en mijn racefiets door stoplicht-loze routes. En het moet gezegd: naast het zijn van mijn paranimf, ben je ook mijn favoriete appeltaart-connaisseur ☺.

Lieve **Ayla**, jij bent een van de weinige mensen met wie ik zonder problemen een tijdje opgescheept kan zitten. Wat was het fijn dat ik altijd met jou kon kletsen zowel binnen als buiten het lab. Kom maar snel terug uit Australië, dan trekken we de wandelschoenen weer eens aan. Waarbij we natuurlijk vertrouwen op jouw richtingsgevoel.

Mijn kamergenoot **Kristina**, bedankt voor het maken van de MRI scans en je hulp bij het maken van de segmentaties. Dank voor de gezelligheid, zowel in ons gezamenlijke kantoor in Rotterdam, als ver daarbuiten (Uden, Riga, Kraslava). Dank voor het beste semi-gezonde salade recept en je onbegrijpelijke Letse humor. Ik hoop dat je opleiding voorspoedig verloopt en dat je een goede radioloog wordt!

Lieve **Suze-Anne**, je hebt een zeer grote bijdrage geleverd aan dit proefschrift en daar ben ik je heel dankbaar voor. Dankzij jouw geduld, slimme oplossingen en overzichtelijke manier van werken ben je een heel fijn persoon om mee samen te werken. Ik heb veel van je geleerd!

Bedankt **Kim vG**, voor al je hulp met de histologie en andere lab-zaken! Fijn dat je altijd tijd voor me kon maken als het nodig was.

Gijs, bedankt voor het faciliteren en het begeleiden van het MALDI onderzoek. Dankzij zowel je enthousiasme, je kritische blik en je brede kennis hebben we dit onderzoek naar een hoger plan getild. Ook leuk dat je plaats wilde nemen in mijn commissie.

Nuria, bedankt voor je hulp met de analyse van de MALDI data. Leuk dat je het MSI onderzoek overneemt. Alle goeds voor de rest van je PhD.

Dear **Ruoyu**, thank you for sharing the office, for sharing your mooncakes and Tony Chocolate and for our shared Switzerland experience. It was nice to work with you on the longitudinal and on the TOMCAT studies and I enjoyed being your paranymph.

Peter Burgers en **Theo Luider**, dank voor jullie hulp met het MALDI onderzoek. Dank voor jullie adviezen en fijn dat jullie de MS/MS experimenten voor ons hebben uitgevoerd.

Heleen van Beusekom, dank voor het faciliteren en het kritisch meedenken met het MALDI onderzoek.

Theo Klein, bedankt voor het uitvoeren van de lipidyzer experimenten en **Yolanda de Rijke**, bedankt voor je enthousiasme en leuk dat je plaats wilde nemen in mijn beoordelingscommissie.

Bram Heijs, jij hebt ons wegwijs gemaakt in de wereld van mass spectrometry imaging en daar ben ik je heel dankbaar voor. Daarnaast bedankt voor de FT-ICR metingen, je feedback op de MALDI artikelen en je gezelligheid op Ourcon.

Stefan Klein, **Dirk Poot** en **Aad van der Lugt**, dank voor jullie hulp bij het verzamelen van de dataset en het opzetten van de pipeline voor de 3D histology studie. Aad, dank dat je deel uit wilde maken van mijn beoordelingscommissie.

Ellen Rouwet, dank voor je hulp en het meedenken bij het verzamelen van de plaques. **Murat**, super dat jij zoveel van de histologie voor mij hebt uitgevoerd!

Bedankt Final Countdown (of Lockdown?)-leden **Lana** en **Inés**, voor de zeer vermakelijke digitale bijklets/klaaguurtjes. Dank voor alle welkome afleiding, gedeelde ervaringen en interessante discussies.

Jolanda en **Ali**, bedankt voor het meedenken met mijn onderzoek. **Eric**, ik vond het altijd fijn om met jou te kunnen sparren en dank voor het delen van je kleurrijke verhalen en meningen. **Su**, nice to have you as a roommate, good luck with the rest of your PhD and your Dutch lessons. **Robert**, dank voor je technische hulp met de MALDI en je gezelligheid. **Frits**, dank voor je assistentie met het inlezen en verwerken van onze MALDI data.

Ik heb goede herinneringen aan mijn tijd in het EMC omdat ik zoveel fijne collega's had: dank aan alle andere Biomedical Engineering bewoners van de 23e en 19e etage, voor de leuke labuitjes, pauze-gesprekken en PhD borrels/spelletjesavonden.

Naast collega's wil ik natuurlijk ook vrienden (**Apen**, **BWerts**, **Lieke**, **Catharina**) en familie bedanken voor hun luisterende oor, weloverwogen adviezen of gewoon voor het zijn wie ze zijn. In het speciaal ga ik nog een aantal mensen noemen.

Fijne collega's zijn 1, maar goede vrienden zijn onmisbaar. Lieve **Martine** en **Mirjam**, wat is het altijd fijn om jullie te zien. In de afgelopen 10 jaar zijn onze gespreksonderwerpen veranderd van roeikoeien, tien-dertiens en pasta bunkeren naar huisjes, boompjes en beestjes. Maar dat maakt onze dates zeker niet minder vermakelijk! En gezamenlijk weten we alles van baby's, pubers en oude mensen, dus eigenlijk hebben we overal verstand van en is er altijd gespreksstof genoeg. Dank voor jullie luisterende oren als ik ze nodig had. Ik hoop dat we zo nog vele jaren doorgaan.

Over luisterende oren gesproken: **Françoise** en **Thomas**, dank voor jullie Delftse gezelligheid. En dank voor de lekkernijen die soms ineens in onze brievenbus of voortuin verschijnen.

Dank aan de Heijdenen, groot en klein: **Gert, Inge, Stijn, Lisanne, Liv, Sven** en **Fiona**. Fijn om zo'n lieve familie te hebben. Lieve **Niek** en **Marlies**, dank voor jullie warme thuis, jullie interesse, steun en goede adviezen. En dank dat jullie altijd klaar staan om te helpen met wat dan ook: van babysitten tot onkruid wieden, van taarten bakken en jurkjes naaien tot het lay-outen van een zeker boekwerk (HEEEEEL erg bedankt hiervoor, Niek!!).

Lieve **Hans, Joost, Max, Tomas** en **Victor**, ik bof maar met zo'n verzameling aan kleurrijke broertjes om me heen! Dankzij jullie buitenlandse avonturen, sterke verhalen, talenknobbels, eindeloze bron van algemene kennis, fun facts, anekdotes, filmquotes en legendarische sinterklaas-rijmbroddelwerken is er altijd wel wat te bespreken in huize Moerman. En the more, the merrier: lieve **Vinnie, Maus, Hadassa** en **Paula**, altijd leuk om jullie te zien!

Lieve **pap en mam**, laat ik maar gewoon zeggen: Bedankt Voor Alles. Bedankt voor jullie steun bij alles wat ik doe. Bedankt voor het warme thuis, waar iedereen altijd welkom is en overal over gediscussieerd kan worden. En dank dat jullie de laatste jaren een fantastische opa en oma zijn geworden. Crèche Maassluis heeft zeker een onmisbare bijdrage geleverd aan de totstandkoming van dit boekje!

Lieve **Jasmijn**, als er iemand in ons huis een echte onderzoeker is, dan ben jij dat! Ik vind het heel mooi om te zien hoe snel je verandert en dingen steeds meer zelf op gaat lossen. Je bent een lief meisje en ik hoop dat je op mag groeien tot een geliefd en eigenzinnig dametje. Ik ben benieuwd wat voor avonturen we allemaal nog samen gaan beleven.

Lieve **Lars**, wat een cadeautje dat jij er bent! Klein als je nog bent, je hebt de laatste fase van mijn PhD pas echt op stoom gebracht want jouw komst vormde wel een zeer strakke deadline. En wat was het heerlijk, na het hectische voorjaar, om een tijdje met jou in een bubbel te leven die alleen bestond uit eten, slapen en verwonderen. Ik ben benieuwd hoe jij de komende jaren de wereld gaat ontdekken.

Als allerlaatste bedank ik jou, lieve **Thomas**, voor alles wat je voor me betekent en alles wat we de afgelopen jaren samen voor elkaar hebben gekregen. Voor je positiviteit, je grenzeloze vertrouwen in mij en je 'ach het komt allemaal wel goed'-mentaliteit. En met jou erbij komt, en is, het ook altijd goed! Jij bent de enige persoon die ik ken, die letterlijk en figuurlijk overal tegenaan kan schoppen en het vervolgens, uiteraard zonder handleiding of duct tape, weer verbeterd in elkaar krijgt. Jij weet precies wanneer je tegengas moet geven of gewoon een stevige schouder ter ondersteuning moet bieden. En jouw arsenaal aan flauwe grappen – die dus ECHT WEL grappig zijn – stelt me nooit teleur. Lieve Thomas, met jou is het leven altijd leuk en verrassend. Dus, na alle opleidingen en titels, is er vooral één ding dat ik zeker weet: we're better together.

Astrid Moerman
Delft, september 2020